physics

MDPI

Article

Force Metrology with Plane Parallel Plates: Final Design Review and Outlook

Hamid Haghmoradi [1,*], Hauke Fischer [1], Alessandro Bertolini [2], Ivica Galić [3], Francesco Intravaia [4], Mario Pitschmann [1], Raphael A. Schimpl [1] and René I. P. Sedmik [1,*]

[1] Atominstitut, TU Wien, Stadionallee 2, 1020 Vienna, Austria; hauke.fischer@tuwien.ac.at (H.F.); mario.pitschmann@tuwien.ac.at (M.P.); raphael.schimpl@tuwien.ac.at (R.A.S.)
[2] Nikhef, Science Park, 1098 XG Amsterdam, The Netherlands; a.bertolini@nikhef.nl
[3] Faculty of Mechanical Engineering and Naval Architecture, University of Zagreb, 10000 Zagreb, Croatia; ivica.galic@fsb.unizg.hr
[4] Institut für Physik, Humboldt Universität zu Berlin, Newtonstraße 15, 12489 Berlin, Germany; francesco.intravaia@physik.hu-berlin.de
* Correspondence: hamid.haghmoradi@tuwien.ac.at (H.H.); rene.sedmik@tuwien.ac.at (R.I.P.S.)

Abstract: During the past few decades, abundant evidence for physics beyond the two standard models of particle physics and cosmology was found. Yet, we are tapping in the dark regarding our understanding of the dark sector. For more than a century, open problems related to the nature of the vacuum remained unresolved. As well as the traditional high-energy frontier and cosmology, technological advancement provides complementary access to new physics via high-precision experiments. Among the latter, the Casimir And Non-Newtonian force EXperiment (CANNEX) has successfully completed its proof-of-principle phase and is going to commence operation soon. Benefiting from its plane parallel plate geometry, both interfacial and gravity-like forces are maximized, leading to increased sensitivity. A wide range of dark sector forces, Casimir forces in and out of thermal equilibrium, and gravity can be tested. This paper describes the final experimental design, its sensitivity, and expected results.

Keywords: Casimir effect; dark sector; force metrology; seismic isolation

Citation: Haghmoradi, H.; Fischer, H.; Bertolini, A.; Galić, I.; Intravaia, F.; Pitschmann, M.; Schimpl, R.A.; Sedmik, R.I.P. Force Metrology with Plane Parallel Plates: Final Design Review and Outlook. *Physics* **2024**, *6*, 690–741. https://doi.org/10.3390/physics6020045

Received: 31 December 2023
Revised: 5 February 2024
Accepted: 11 February 2024
Published: 7 May 2024

1. Introduction

Continuous improvements in measurement methods during the past few decades have unveiled a number of tensions between predictions of the standard models of particle physics (SM) and cosmology (ΛCDM) with observations. Since the 1970s, the development and testing the SM have been dominated by collider experiments culminating in the experimental discovery of the Higgs particle. However, further advancement on the high-energy frontier appears difficult, as the required technological and financial efforts grow over-proportionally with the gain in energy. Yet there are still sixteen orders of magnitude missing between the current 10 TeV scale and the Planck scale. Therefore, precision measurements at lower energy have established themselves as an alternative route to test existing theories and to search for the physics beyond.

Precision tests have unveiled a growing number of 'tensions' in various fields that cannot be explained well on the basis of existing theory. We can highlight only a few of these here. For quantum electrodynamics, measurements of the relative gyromagnetic moments, $(g-2)/2$, of fermions have revealed values [1] that differ from theoretical expectations by 2.5σ (standard deviation) for electrons and 4.2σ for muons, giving a strong signal of an incomplete understanding of either vacuum fluctuation contributions or new physics. Charge radii of the proton and the deuteron have been determined using precision (Lamb-shift) spectroscopic measurements with H and D, as well as from electron and muon scattering experiments (see review [2]). Even after a recent re-analysis of experimental

errors, and new measurements, tensions at the 2σ [3] and 3.5σ [2] level, respectively, exist between different experiments and between experiments and theory. While QED is still referred to as the 'best-tested theory', even after about 150 years, the question of whether the electromagnetic energy momentum tensor is traceless or not in materials remains open [4]. Tensions are also known for other elements of the SM. For example, the Cabibbo–Kobayashi–Maskawa (CKM) quark mixing matrix of QCD shows increasing signs of non-unitarity (currently 2.2σ [5] or up to 2.8σ [6]), which, if confirmed, would be an indication for beyond SM physics. In QCD, the breaking of CP symmetry being suppressed by a factor 10^{-10} creates a fine tuning problem that could be resolved [7,8] by an additional spontaneously broken 'Peccei–Quinn' symmetry leading to the axion as its associated Nambu–Goldstone boson [9,10]. The latter is constrained strongly but is not yet excluded. Another strong motivation for the axion is due to it providing an excellent candidate for dark matter (DM).

DM has a solid basis of evidence, as galaxy rotation curves have been measured since the early 20th century [11], and newer probes, such as cosmic microwave background or weak lensing data indicate that a fraction $\Omega_{\rm DM} \approx 0.27$ [12] of the total mass in the universe can be attributed to DM (see [5] for a review). Numerical simulations [13] show that the current large-scale structure of the universe can only be obtained if DM is taken into account, with baryonic matter ($\Omega_b \approx 0.05$) playing a sub-leading role.

Twenty five years ago after the discovery of accelerated expansion [14–16], there are clear indications that by far the largest fraction of the energy/mass content of our universe ($\Omega_{\rm DE} \approx 0.68$) is due to the existence of what is generically termed 'dark energy' (DE). In general relativity (GR), dark energy can effectively be described in terms of a cosmological constant Λ providing the negative pressure necessary to account for an accelerated expansion of our universe. In combination with 'cold' DM this constitutes the cosmological standard model ΛCDM. However, as the Hubble constant H_0—being a measure of expansion—obtained from data on the cosmic microwave background at large redshift z, is at significant tension (5σ) with the one obtained from local distance ladder measurements at $z < 2.36$ and a range of other measurements [17], speculations arise (among others) if Λ is a constant after all [18]. Significant tensions exist not only in measurements of H_0 but also for several other parameters of ΛCDM) [19]. Since DE accounts for the largest fraction of the energy/mass content of our universe, the quest for an answer to the question what the dark sector is composed of has received significant attention. It is currently unknown whether DE and DM are composed of new particles or not, but the answer lies probably beyond the current SM/ΛCDM framework.

While amending general relativity by the cosmological constant enables us to describe an accelerated expansion, such a procedure would lead to a severe fine-tuning problem, which is the so-called '(old) cosmological constant problem' [20]. This is due to contributions in addition to Einstein's original (bare) cosmological constant, coming from the zero-point energies of all quantum fields (SM fields as well as possible unknown ones), as well as the Higgs potential during its phase transition related to electroweak symmetry breaking [21]. Introducing a cutoff at the Planck scale or electroweak unification scale in order to render the zero-point energies finite, these contributions provide values for Λ that are 123 or 55 orders of magnitude above the measured value containing all contributions [20]. This may suggest that quantum fluctuations of the vacuum do not seem to gravitate [22], which has cast some doubt on their reality. Some authors have resorted to the rather metaphysical anthropological principle [23] to explain the 'cosmological constant problem' [24], while others, just to give an example, have attempted to find explanations in terms of a natural cutoff given by metric feedback at high energies [25]. If there existed additional interactions, cancellations of the zero-point energies of these new fields and the ones of the standard model [26] could explain the smallness of Λ. However, we would be left with a severe fine tuning problem, which adds to the problem of the non-gravitation of vacuum fluctuations. By now, a whole host of conceptually distinct approaches has been devised to avoid this problem (see, e.g., [20,21,27]) with no final solution.

While no general consensus has been found on the above tensions, one approach to explain them is to introduce new interactions. The historically very successful approach to search for the associated new particles in colliders, however, has not led to any discoveries so far, for either DM or DE. Indications for weakly interacting massive particles (WIMPs) have not been found at high energies. Lighter particles searched for by recoil experiments have also eluded detection (the DAMA experiment's periodic DM signal [28] is not generally considered to be confirmed at the time of writing) despite quite large international efforts. Astronomical observations, on the other hand, may have found indications for sterile neutrinos [29,30] and WIMPS [31]. Indications were also found in long baseline nuclear experiments but are still being discussed. As no clear signs regarding the type or energy range of new interactions have been found, theoreticians have turned to the broad field of effective field theories to give generic predictions that allow experimentalists to narrow down the possibilities for DM and DE models. Irrespective of the true physical origin, an effective field theory enables describing and classifying the low-energy behavior of the corresponding fundamental theory in a model-independent way. As such, the 'Standard Model Extension' [32] covers all possible $CP(T)$-violating terms that could be added to the SM. Several of these can also be written in terms of bosonic spin-0 or spin-1, scalar, vector, or tensor interactions (and their respective pseudo or axial counterparts) between SM fermions [33,34]. The latter leads to a class of effective potentials that can be tested in a large number of experiments [35]. For DE, besides modified gravity, variable dark energy models, and black holes, a class of screened scalar fields has been investigated that would describe dynamical 'quintessence' scalar fields with an effective potential depending on the local mass density. This local variability permits them to 'hide' in denser environments and evade stringent astrophysical bounds while still being able to prevail in low density regions, thereby describing DE. However, these models have several free parameters, and only a few, such as the string-inspired dilaton, have a more solid motivation.

In any case, the cosmological constant problem provides further indications that our understanding of the quantum vacuum may be incomplete. This has been one of many motivations for investigations of the Casimir effect. Being the only known quantum effect causing forces between separated macroscopic objects, experiments have been performed since its prediction in 1948 [36]. Modern experiments starting in the 1990s [37–39] have tested non-trivial boundary dependence [40,41] and lateral forces [42,43], thin layers [44], dielectric properties [45–51], influence on micro-electromechanical elements [52,53], torque [54], and repulsion [55–57], to name just a few topics. Regarding the description of the dielectric properties, especially for the thermal contribution to the Casimir effect, there has been a discussion going on for more than two decades (see review [58]). Specifically, a disagreement between theoretical predictions and experimental results put the focus on the proper account of dissipation in the description of the material optical response. Surprisingly, a simple non-dissipative model provides a better description of several experiments measuring the Casimir interaction between metallic objects. Consequently, the same experiments appear to exclude an account of dissipation in terms of the commonly used Drude model [59]. A similar issue was noticed for free electrons in semiconductors [60]. Within the same context, attention has also been devoted to surface roughness [61] and patch potentials [62,63] as a possible source for the disagreement between theory and experiment. Other material properties were investigated and, in particular, non-locality (spatial dispersion) has also attracted attention [64] in relation to thermodynamic inconsistencies, which may appear when the Drude model is adopted for the description of a metal [65]. However, up to now, all attempts have failed to reach an unanimous consensus, and more precise experimental data are required to settle the controversy [58]. More recently, it was pointed out that a non-equilibrium configuration in which the objects are at different temperatures, T_1 and T_2, can serve as an additional benchmark of the theoretical framework surrounding the Casimir effect [66]. In this case, an additional contribution to the interaction, anti-symmetric under the exchange $T_1 \leftrightarrow T_2$, has been predicted. Still, this contribution has not yet been quantitatively confirmed in a Casimir experiment.

Experimentally, precision Casimir experiments have also been used to set limits on new interactions [67–79] at small separation a, as proposed four decades ago [80]. However, the sensitivity is limited [81], as one of the strongest uncertainties in such measurements comes from local surface charges that are hard to quantify and control [62,81]. These uncertainties can be mostly avoided by using the 'iso-electronic' technique [59,70,82] (allowing only relative measurements) or by placing an electrostatic shield between the test objects, leading to the Cavendish configuration that has been extensively used in torsion balance experiments [83–96] to measure gravity-like interactions. However, a shield between the interacting objects precludes the measurement of Casimir forces and DE screened scalar fields. Another common disadvantage of most existing precision force experiments in either configuration is that they use curved surfaces of some radius R_s. Depending on the distance dependence of the investigated interaction, the effective surface area generating the force is thereby dramatically reduced from $A = R_s^2\pi$ to $A_{\text{eff}} \approx \pi R_s a$ [97,98] with $a \ll R_s$. Therefore, one looses a factor $\eta_{\text{eff}} \equiv a/R_s = 10^{-2}$ to 10^{-4} in force sensitivity [99]. This problem is maximally avoided for plane parallel plates, where $\eta_{\text{eff}} = 1$. The downside is that one has to measure and control parallelism and use perfectly flat surfaces, which introduces significant technical complications. Previous attempts to measure Casimir force gradients between parallel plates [100,101] have suffered from electrostatic and other unresolved offsets for which the results included a free fit parameter.

The Casimir And Non-Newtonian force EXperiment (CANNEX) has been designed from the onset to perform measurements between macroscopic plane parallel plates [102]. After a first proof of principle [103], we continuously updated the design [99,104] to characterize, attenuate, or actively control all relevant disturbances. The setup allows synchronous measurements of the pressure and pressure gradient with nominal sensitivities of $1\,\text{nN}/\text{m}^2$ and $1\,\text{mN}/\text{m}^3$, respectively, in both the Cavendish and Casimir configurations, in the distance regime $3\,\mu\text{m}$ to $30\,\mu\text{m}$. Recently, we selected the Conrad Observatory (COBS), a geoseismic and geomagnetic surveillance station inside a tunnel system in the Alps as a location. The seismic and thermal stability there will reduce errors and technical requirements of isolation systems for CANNEX. Operations at COBS are expected to commence in the summer of 2024.

In this paper, we present the final design and its predicted performance in Cavendish and interfacial (Casimir) configurations in Section 2. Subsequently, we update our recent error budget [99] taking into account actual device specifications and preliminary noise measurements. We then give an update on prospects for measurements of in- and out-of-equilibrium Casimir forces [66] in Section 4.1. Finally, we present updated prospects for DE screened scalar field limits [99,102,105] in Section 4.2, based on fully consistent numerical calculations taking into account the experimental and theoretical uncertainties, and close with a short outlook in Section 5.

2. Experimental Design

CANNEX is a metrological setup designed to synchronously measure forces and force gradients between plane parallel plates at separations between 3 µm and 30 µm in interfacial and Cavendish configurations. Force (gradients) are measured by interferometrically detecting (see Section 2.5) the movement of a mass-spring system consisting of a 'sensor' plate and a set of helical springs. Forces onto the sensor plate are sourced by a second fixed 'lower' parallel plate, as shown in Figure 1d. Since this mechanical detection system is highly sensitive to mechanical vibrations, surface charges, and thermal changes, we have included countermeasures for all of these disturbances in terms of active control and attenuation systems into the design, described in detail in Sections 2.1, 2.2, and 2.4, respectively. In what follows in this section, we give an overview of the setup.

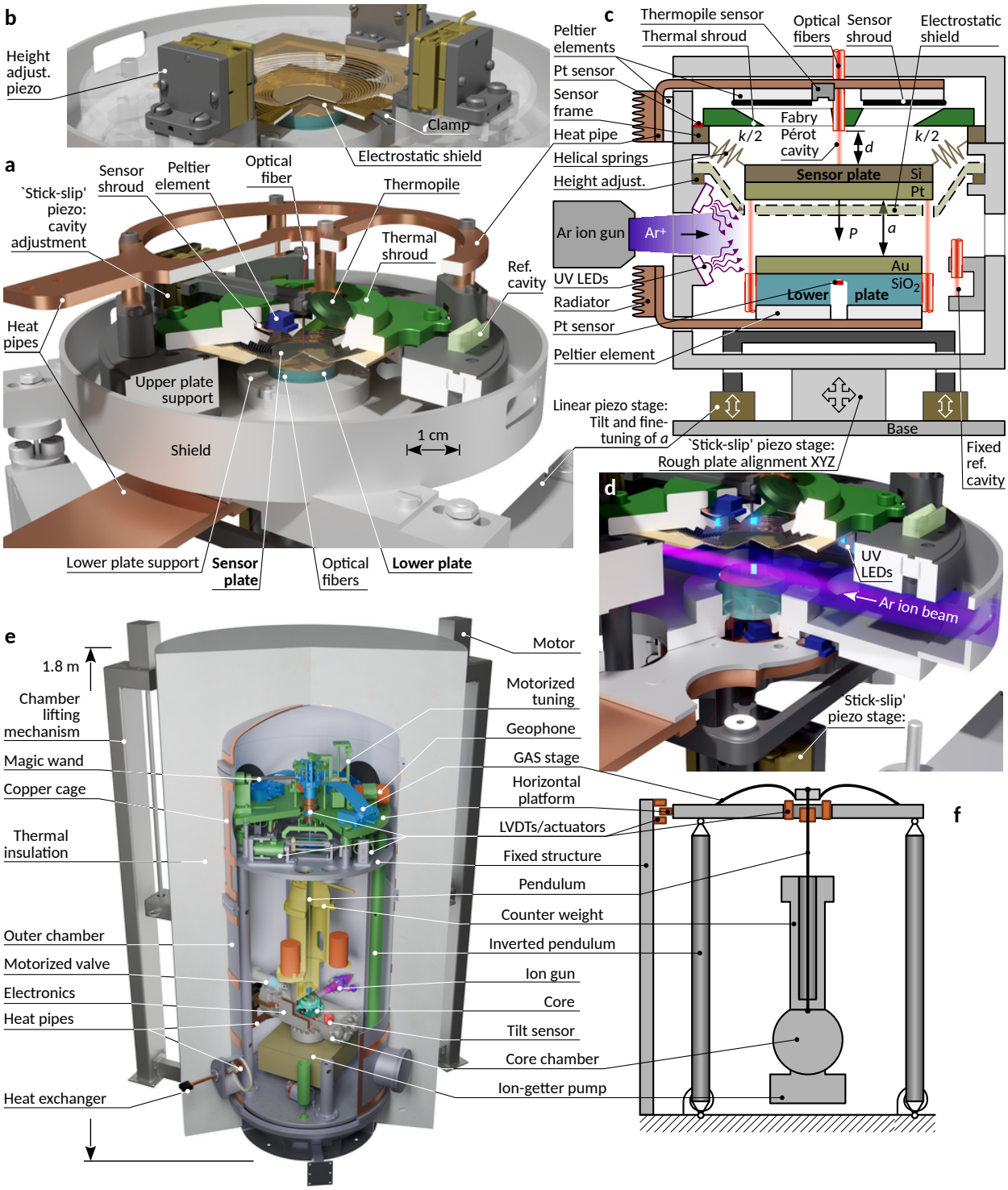

Figure 1. The CANNEX setup. (**a**) Simplified cut view of the actual core design in interfacial configuration. (**b**) Simplified focus view of the Cavendish configuration with the electrostatic shield and associated adjustment stages. (**c**) Schematic representation of the core including all elements and configurations. (**d**) View of the core with the translator stages in their upper position, in which the ion tunnels are opened for Ar ion cleaning and UV irradiation. (**e**) Cut view of the complete setup. (**f**) Schematic view of the seismic attenuation system (SAS).

The setup's 'core' contains the actual measuring device. Here, the lower plate, made of silica glass, is mounted in a fitting (light gray in Figure 1a–d) that isolates it thermally and electrically from the rest of the setup. The fitting is supported by three linear piezo

transducers with a range of 200 µm, allowing us to fine-tune the parallelism and separation between the plates. Thermal control of the lower plate can be achieved via Peltier elements (PE)s below it and a platinum sensor at its center. Attached to the side of the lower plate are three optical fibers used to measure the plate separation and tilt (see Section 2.5).

The force sensor is fabricated from a silicon single crystal (Norcada Inc., Edmonton, AB, Canada) and placed directly above the lower plate. Its position can be adapted by a three-axis drift-free stick-slip stage (SLC-1720, Smaract GmbH, Oldenburg, Germany) supporting the entire upper part of the core. The sensor's frame is connected to a massive support structure (middle gray in Figure 1a,c,d) that is thermally controlled by distributed PEs, and electrically grounded. The support carries a thermal shroud (green) allowing for non-contact thermal control of the sensor and its springs.

Sensor movements are detected via an optical fiber placed above its center (see Section 2.5). The fiber is attached to a drift-free stick-slip piezo transducer allowing us to adjust the cavity size. Similarly, the separation a between the lower and upper plate is monitored by three interferometers arranged around the rim of the lower plate. The fibers' end faces are polished optically together with the lower plate in order for them to be at exactly the same height. CANNEX implements three different configurations. In the first—interfacial—configuration, the sensor plate directly faces the top surface of the lower plate. In the second—Cavendish—configuration, we add a gold-coated silicon nitride membrane acting as an electrostatic shield (ESS) between the two plates. The ESS is held by three stick-slip piezos (see Figure 1b) to change its height and orientation. Despite its relatively large area (1 cm^2) and small thickness (<1 µm), the ESS has an extremely low hang-through under gravity of about 1 µm. Three pinholes in the ESS allow the lower plate's interferometers to operate both through the ESS (to measure a) and when shifted slightly to the side to monitor the separation between the ESS and the lower plate. This mechanism allows us to unambiguously determine and control the relative position of all three plates with respect to each other. In the third configuration discussed in Section 2.4, which is only used for surface characterization, either the sensor and the shroud, or the lower plate and its fitting, are replaced by a Kelvin probe setup able to scan the surface potential and topology of the entire surface area of the remaining plate.

The core assembly, Figure 1a, is enclosed inside an ultra-high vacuum (UHV) 'core' chamber. This chamber can be evacuated down to a pressure of 10^{-9} mbar by using an ion-getter pump or be filled with up to 500 mbar of Xe gas for measurements of screened DE interactions [106]. On the outside of the core chamber wall, the core electronics are placed on a copper plate that allows generated heat to be guided away without mechanical contact to the outside of the outer chamber (shown partially in Figure 1e). A similar but independent mechanism exists for the heat pipes emerging from the core itself. Details on these systems are given in Section 2.3. The core chamber is suspended on a 6-axis seismic attenuation system (SAS) shown in Figure 1e,f. The SAS comprises an inverted pendulum (green) for horizontal isolation, a geometric anti-spring (GAS) filter (blue) for vertical isolation, and a mass tower (yellow) improving tilt isolation, as described in more detail below. Additionally, a hollow silicon carbide rod, known as a compensation wand (magic wand), is connected to the tip of the GAS filter to improve the attenuation performance [107]. Vertical and horizontal positions of the SAS can be sensed by linear variable differential transformer (LVDT) sensors, and controlled by motorized pre-tension springs. In addition, the dynamical behavior in translational degrees of freedom can be influenced by voice coil actuators. For higher sensitivity at intermediate frequencies, geophones are used to monitor all but the vertical rotation degree of freedom. Inverted pendulums (IPs) support the base plate of the GAS filter, thereby combining vertical and horizontal attenuation systems.

The entire SAS with the core is enclosed in an 'outer' vacuum chamber at 10^{-6} mbar providing further isolation against sound, thermal, and other environmental disturbances. This chamber is mechanically decoupled from the SAS, to ensure deformations due to pressure differences do not influence the performance of the SAS. The outer chamber is fitted with a dense grid of copper bars and a 25 cm insulation layer to reduce temperature

gradients on the chamber wall. We use PEs on the mentioned copper bars to control the chamber temperature with a precision of about 4 mK. Eventually, the chamber includes several exterior mechanisms (not shown) to open it, and to extract the core with minimum mechanical input to the sensor. The entire setup is placed inside an ISO class 7 cleanroom inside the tunnels at COBS.

2.1. Seismic Attenuation

Seismic vibrations present a significant impediment to the precision of small-distance metrology setups, necessitating a comprehensive understanding of their impact on the respective measurements. CANNEX uses non-linear mechanical elements developed for gravitational wave detectors [108–110]. For vertical isolation, a geometric anti-spring (GAS) filter [111] (blue in Figure 1e) provides 40 dB/decade attenuation from roughly 100 mHz. We employ so-called 'magic wands ' [107] to augment filter performance at low frequencies and near the sensor resonances. Horizontal isolation is achieved by inverted pendula [112] (green) carrying the GAS filter and a regular pendulum suspending the core chamber. The tilt of the core chamber around the horizontal axes is attenuated by the core chamber being mounted on the pendulum close to its center of gravity. The latter is raised to the hinge point by means of a massive tower (yellow), which reduces the tilt resonance frequency.

Previously, the Atominstitut (ATI) of TU Wien, Austria, was considered as the location for CANNEX [99]. We have identified a more suitable location in the underground laboratory of the Conrad observatory, roughly 50 km southwest of Vienna. Seismic spectra have been recorded at both locations and are shown in Figure 2. As we discuss in Section 3.1 below, a one-staged passive SAS at COBS already fulfills all requirements for the targeted error level, while at ATI, a two-stage isolation system would be required [99]. In what follows here, we describe the final system, which is similar to already realized systems in the literature [109,110].

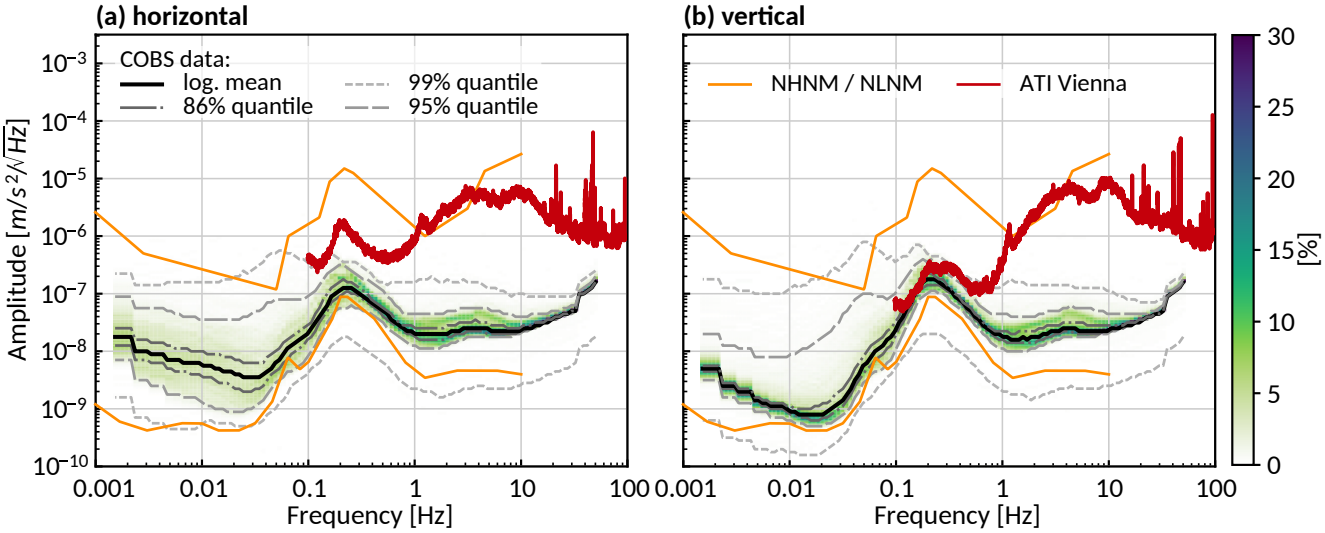

Figure 2. Seismic background in (**a**) vertical and (**b**) horizontal (eastern) direction. Data were recorded at COBS using calibrated STS-2 seismometers between 30 April 2023 and 30 June 2023, including four earthquakes of magnitude up to 3.3. The black line is the logarithmic mean of the data, while the dashed gray lines represent the quantiles obtained from histograms at each frequency. The green and blue color encodes the probability. In comparison, the seismic background at the Atominstitut (ATI) in Vienna, recorded using calibrated Sercel L4C geophones during 24 h starting 28 September 2018, is significantly higher due to a nearby highway, subway, and in-house noise sources. For reference, we give Peterson's new high- and low-noise models [113] (NHNM and NLNM, respectively).

The principle of GAS filters [111] and inverted pendula [112] relies on the instability of non-linear mechanical systems at which the stable operating point splits into two distinct solutions. Such points lead (theoretically) to zero resonance frequency and thereby ideal isolation. In practice, internal damping and creep set limits on the achievable minimum resonance frequencies. We can describe our SAS by the model shown in Figure 3. The respective small-signal Lagrange functions $\mathcal{L}_D$ for the horizontal ($D = h$) and vertical ($D = v$) directions are given by

$$\mathcal{L}_h = \mathcal{T}_h - \mathcal{V}_h \tag{1}$$

$$\text{with } \mathcal{T}_h = \frac{1}{2}\left[I_0(\partial_t\alpha_0)^2 + I_2(\partial_t\alpha_2)^2 + m_1(\partial_t x_1)^2 + m_2(\partial_t x_2)^2 + m_0(\partial_t x_c)^2\right],$$

$$\mathcal{V}_h = \frac{1}{2}\left[k_0(x_1 - x_0)^2 + k_{w2}(\delta_{1l}^2 + \delta_{2u}^2)\right] + m_0 g y_0 + m_1 g y_1 + m_2 g y_2,$$

$$\mathcal{R}_h = \frac{1}{2}\left[\gamma_{2h}(\partial_t x_2 - \partial_t x_0)^2 + \gamma_{1h}(\partial_t x_2 - \partial_t x_1)^2 + \gamma_{0h}(\partial_t x_1 - \partial_t x_0)^2\right],$$

$$x_c = x_0\left(1 - \frac{l_{0cm}}{l_0}\right) + x_1\frac{l_{0cm}}{l_0},$$

$$y_0 = -\frac{1}{2}\alpha_0^2 l_{0cm}, \quad y_1 = -\frac{1}{2}\alpha_0^2 l_0, \quad y_2 = y1 + \frac{1}{2}(\delta_1^2 l_2 + \alpha_2^2 a_{2u}),$$

$$\delta_1 = \frac{x_2 - x_1 - a_{2u}\alpha_2}{l_2}, \quad \delta_{2u} = \alpha_2 - \delta_1, \quad \alpha_0 = \frac{x_1 - x_0}{l_0}, \quad \partial_t\alpha_0 = \frac{\partial_t x_1 - \partial_t x_0}{l_0}.$$

$$\mathcal{L}_v = \mathcal{T}_v - \mathcal{V}_v, \tag{2}$$

$$\text{with } \mathcal{T}_v = \frac{1}{2}\left[m_2(\partial_t z_2)^2 + m_c\left(\frac{l_c}{l_w}(\partial_t z_2 - \partial_t z_0)\right)^2\right],$$

$$\mathcal{V}_v = \frac{1}{2}k_{v1}(z_2 - z_0)^2, \quad \mathcal{R}_v = \frac{1}{2}\gamma_1(\partial_t z_2 - \partial_t z_0)^2.$$

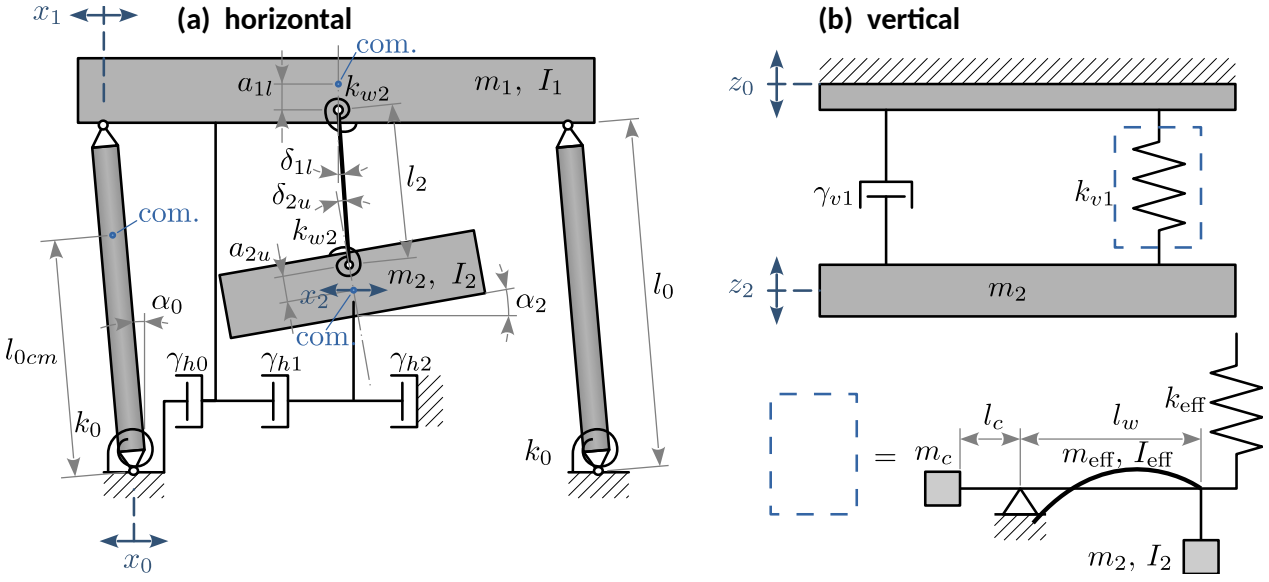

Figure 3. Model for the dynamical behavior of the CANNEX SAS in (**a**) horizontal and (**b**) vertical direction. The centers of mass are indicated by 'com.'. See text for details.

Here, in $\mathcal{T}_h$, the first two terms describe the angular kinetic energy of the top and payload masses m_1 and m_2, respectively. The last three terms are the linear kinetic energies of the top, payload, and inverted pendulum (m_0) masses. Potential energies for the inverted pendulum tilt and wire tilt are given by the first two terms in $\mathcal{V}_h$, while the last two terms

regard the change in the absolute height of m_1 and m_2 due to rotary (sidewards) movements of the inverted pendulum and pendulum, respectively. The wire is resisting with elastic constant k_{w2} its deformation at both fixed ends with angles δ_{1l} and δ_{2u} due to the swing x_2 and tilt α_2 of the payload. Viscous damping between all parts is considered by the Rayleigh dissipation terms in $\mathcal{R}_h$, while internal friction is added ad hoc by adding to the effective values $k_i = \omega_i^2 m_i$ (for masses $i = 1, 2$ and resonance frequencies ω_i), representing the spring constant of system i a factor $(1 + \mathrm{i}\phi)$ with $\phi < 1$ [107], which is not shown here for brevity. Similarly, for the vertical direction, we have the linear kinetic energy of the payload mass and wand counter weight μ_c in $\mathcal{T}_v$. Deformation of the GAS filter gives a contribution to the potential energy $\mathcal{V}_v$, while viscous damping between the top stage and the payload contributes to the damping term $\mathcal{R}_v$. y_1 approximates the vertical shift of m_1 for small angle, α_0. Consequently, y_2 is the vertical shift of m_2 due to the combined action of the pendulum and inverted pendulum. The I_x denote the moments of inertia of the inverted pendula ($x = 0$), the upper platform ($x = 1$), the payload (core chamber, $x = 2$), and the GAS springs ($x =$ eff) obtained numerically from CAD software. γ_x denote damping coefficients, k_x are (effective) elastic constants, and m_x are masses as defined in Figure 3. Note that we use the notation $\partial_x \equiv \partial/\partial x$.

The Euler–Lagrange equations giving the dynamical behavior of the system are then

$$\frac{\partial \mathcal{L}}{\partial u} - \frac{\partial}{\partial t}\frac{\partial \mathcal{L}}{\partial(\partial_t u)} - \frac{\partial \mathcal{R}}{\partial(\partial_t u)} = 0\,, \tag{3}$$

for $u = x_i, z_i\,, \alpha_i$. Equation (3) can be resolved for the transfer functions $T_{x0x2} \equiv X_2/X_0$, $T_{x0\alpha_2} \equiv \alpha_2/X_0$, and $T_{z0z2} \equiv Z_2/Z_0$ for the horizontal, tilt, and vertical degrees of freedom. We have optimized the system's parameters with respect to low resonance amplitude and maximum attenuation around the sensor resonance frequency $f_0 = 9.8\,\mathrm{Hz}$, resulting in the responses shown in Figure 4. We obtain a vibration suppression of about 77 dB and 66 dB in the horizontal (both axes) and vertical direction, respectively, at f_0, which suffices to achieve the targeted sensitivity under all circumstances, as discussed further in Section 3.

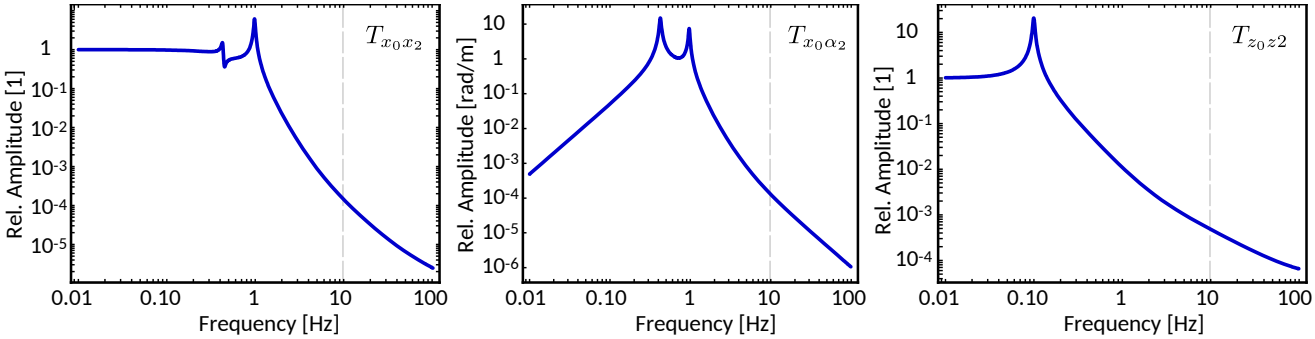

Figure 4. Transfer functions of the passive CANNEX SAS from horizontal and vertical vibrations to core movement and tilt, respectively, as indicated. The vertical dashed lines indicate the position of the sensor resonance.

The current design includes linear variable differential transformers (LVDT) combined with voice coils for force feedback on the horizontal and vertical degrees of freedom as well as geophones. These sensors and actuators shall be used to reduce the amplitude of resonances and improve the overall performance, as described for similar systems [114]. The design of the feedback system is still in progress.

2.2. Surface Charge Cancellation

Electrostatic patch potentials due to local variations in the Fermi potential of surfaces, chemical impurities, and charge accumulation [115] are a major nuisance in all interfacial force experiments [81,116,117]. Over the years, several methods to characterize and compute these forces (gradients) have been developed [62,116,118–120]. Recently, a new ex-

perimental approach was presented to reduce surface charges in situ [121]. UV irradiation can be used to dissociate larger molecules and extract electrons from surfaces. The residual impurities can then easily be removed by a variant of plasma cleaning using a low-energetic beam of Ar ions. After the process, the surfaces have been demonstrated to exhibit strongly reduced local variations in the potential and a low overall force minimizing potential.

In CANNEX, we implement a dual strategy. Firstly, in all configurations (interfacial and Cavendish), active surface cleaning using an Ar ion source and UV irradiation are possible without the need to break the vacuum. This is enabled by the vertical translator stage of the upper plate being able to lift the sensor to a distance of about 5 mm above the lower plate and simultaneously open a window in the shield to clear the path for an Ar ion beam (see Figure 1d). Using eight high-power LEDs viewing the gap between the plates, we can apply UV irradiation at 275 nm wavelength with up to 2 W in short pulses (visible in Figure 1c,d). Secondly, the performance of the cleaning procedure can be monitored in situ using a custom-built Kelvin probe setup (see Section 2.4) mounted in place of the force sensor. Once the distribution, stability, and amplitude of the surface potentials after cleaning and intermittent exposure to air [115] have been determined on both interacting surfaces, the regular force measuring configuration is restored to perform exactly the same cleaning procedures as before.

Apart from patch potentials, two opposing surfaces differ in their absolute potential even if grounded together due to contact potentials. To cancel these, we use an active homodyne compensation method that was successfully applied in recent measurements of Casimir forces [122–124] and in the proof of principle for CANNEX [103]. The method is similar to amplitude modulation Kelvin probe force microscopy (see below), and relies on a small electrostatic excitation, $v_{\mathrm{AC}}(t) = V_{\mathrm{ac}} \sin \omega_{\mathrm{AC}} t$, being applied to the lower plate, resulting in signals at frequencies ω_{AC} and $2\omega_{\mathrm{AC}}$, whose amplitudes are measured using a lock-in amplifier. The prior signal is then used to drive a feedback circuit that applies an additional potential V_{DC} to the plate, thereby driving $(V_{\mathrm{DC}} - V_0)$ to zero [103,122] with high accuracy. The signal at $2\omega_{\mathrm{AC}}$ can be used to independently measure the surface separation electrostatically or what is not required in CANNEX due to the optical method, to perform an independent measurement of the mechanical properties of the sensor. Importantly, all potentials are applied to the lower plate, while the sensor and all other parts are kept on the ground potential. Note also that all surfaces and contacts, except for isolating spacers, are coated by gold to exhibit the same absolute surface potential. The real potentials applied to both plates are measured at all times using a calibrated in situ electrometer amplifier.

2.3. Temperature Control

According to the error budget described in Ref. [99], achieving the targeted error levels of $1\,\mathrm{nN/m^2}$ and $1\,\mathrm{mN/m^3}$ is only possible if the thermal stability of the sensor and optical cavities of 0.1 mK is guaranteed. In order to comply with this requirement, both plates have an independent thermal control system responsible for providing the desired thermal stability. We use calibrated custom-made low-noise controllers with 24-bit converters. The lower plate's thermal system is based on thermal conduction and consists of several PEs located below a copper plate attached to the bottom of the lower plate and a platinum sensor situated in a hole at the center of the lower plate body to read the temperature as close as possible to the top surface of the plate. The copper plate is insulated thermally from other parts by reflective coatings and mechanically by a gap to suppress heat transfer via radiation and conduction, respectively, between the lower plate and other parts of the core. The lower plate itself is clamped down onto the copper plate and into its fitting using spring-loaded ruby balls, which minimizes mechanical contact area and limits heat loss towards the sides. The sensor plate's temperature is stabilized with a combination of a contact and a non-contact feedback loop. The contact loop consists of several platinum sensors and PE combinations on a copper plate between the upper plate support (Figure 1a) and the thermal shroud on top of it, thereby controlling the sensor frame. The central disk of the sensor is connected to its frame only via the long and

thin spring arms, for which thermal conduction plays a minor role. On the other hand, the sensor plate exchanges radiation with the lower plate. Despite highly reflective metal coatings on both sides, heat will be transferred between the two plates as soon as they have different temperature setpoints. As the function of the sensor precludes any mechanical contact with its center, the only option to stabilize the upper plate's temperature is via radiation. For this purpose, a blackened copper ring being controlled in temperature by a separate circuit is placed inside the shroud such that it is visible from the sensor plate's surface. This ring counteracts radiation heating or cooling of the sensor plate by the lower plate. Importantly, we optimized the view factor to the sensor's springs such that they are minimally influenced by radiation from either the ring or the lower plate. Another opening in the shroud allows a thermopile to view the sensor plate and monitor its temperature with <0.1 m°C precision. This input is used to control the temperature of the ring and in consequence the temperature of the sensor disk. A finite element method (FEM) study was conducted using COMSOL Multiphysics to examine the temperature and respective gradients in all parts of the core. Figure 5a,b show the preliminary results of this study for the temperature distributions of both plates for a temperature setpoint of the lower plate being 10 °C higher than the ambient temperature. The deviation on the upper plate with respect to the setpoint (293.130 K) is kept below 0.27 mK, while on the lower plate, the deviation reaches 3.31 mK.

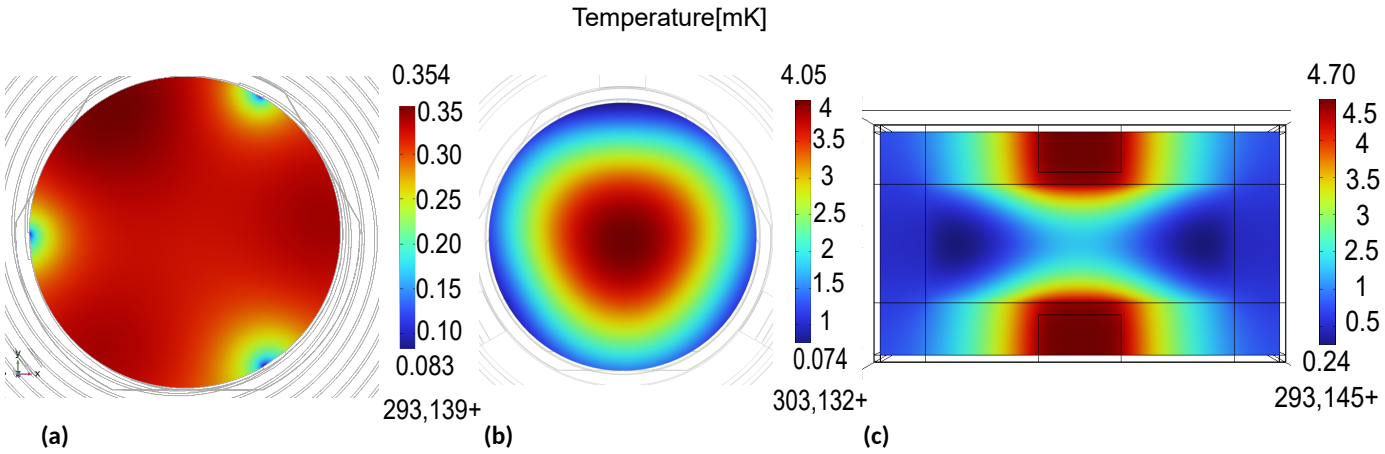

Figure 5. Results of an FEM analysis of thermal distributions. (**a**) sensor plate (**b**) lower plate in the core for a nominal difference of 10 °C between the two plates. (**c**) chamber wall grid cell (see text). Here, only the relative deviations on the parts are accurate, while the absolute temperatures may contain relatively small offsets due to fixed power input instead of feedback control in the numerical computations.

Proper operation of a PE requires the side opposite to the controlled surface to be connected to a heatsink. Therefore, all PEs atop the upper plate, support, and shroud are connected via vertical copper columns to the large circular heatpipe on top connected via flexible parts (not shown) to a thermal feedthrough at the back chamber wall. Below the lower plate, the non-control side of the PEs is connected to a heat pipe (shown on the lower left of Figure 1d), which leads to a radiator permitting contactless heat transmission between the core and a feedthrough at the back chamber wall of the core. Similarly, there are two radiators between the core chamber and outer chamber that contactlessly exchange heat with their respective counterpart, partially visible in Figure 1e. These radiators on the inner side of the outer walls are connected to heat pipes leading through the outer wall to a thermal controller regulating the heat pipe temperature and effectively releasing excess heat via a heat exchanger to the environment. The radiators themselves are interleaved comb-like structures with a relatively large overlap between the interacting parts, blackened on the inside and reflective on the outside. Optimization and testing of these structures is still in progress.

The strong dependency of the working point of the non-linear mechanical elements of the SAS on thermal variations [111] makes it crucial to actively stabilize the temperature of the outer chamber wall as well to within about 5 mK. This requirement is not changed by our DC-feedback with the pre-tension springs. The low amount of power produced by CANNEX's SAS, which still could be a critical thermal disturbance, is dissipated via radiation interaction with the wall. At the setup's location at COBS, the ambient temperature changes by much less than 0.1 °C per day with an average of roughly 10 °C, for which we expect little exterior thermal fluctuations. To keep the chamber close to the setpoint (about 290 K), we add 25 cm of passive thermal isolation around the entire chamber. Below the isolation, the entire chamber wall is covered with a dense grid of 5 mm thick copper bars to improve the heat conduction on the walls. On top of the copper bars, we add 50 independent calibrated control units each consisting of two PEs and two platinum resistors. In Figure 5c, we show the results of an FEM study of the resulting temperature distribution on the inside of the chamber wall for one representative unit cell of the gridded chamber wall.

2.4. AFM/KPFM Setup

In Section 2.2, we discussed the setup for surface charge cancellation by the combined action of an Ar-ion beam and UV irradiation cleaning. To ensure the consistency and performance of these methods, to investigate the long-time evolution of the surface potentials, and to measure the influence of exposure of the setup to the atmosphere [125] (which is inevitable while working on it), we add a Kelvin probe force microscope (KPFM) to the setup. The KPFM has been designed to offer two configurations. In the first one shown in Figure 6, the surface charge distribution on the lower plate can be investigated in situ before and after cleaning. The sensor plate and shroud (see Figure 1) of the force sensing setup are replaced by a u-shaped structure (green) carrying an AFM cantilever. The optical fiber, which is otherwise used for measurements on the sensor plate, is remounted at an angle to detect the movement of the cantilever interferometrically, in a similar way as demonstrated previously [124,126]. In order to align the fiber with the cantilever tip in situ, we use a stack of horizontal stick-slip translators. The scanning motion of the tip and vertical coarse alignment is carried out by the movement of the 3-axis stick-slip piezo translator stack (golden, at the bottom in Figure 6). Note that these stages have a range of more than 12 mm, for which they can be used to investigate the entire area of the lower plate with the KPFM. Because of the comparably large surface separation in CANNEX, only patches of size $\lambda_p \gtrsim a/10$ are of interest [127], with a being the separation between the plates. Therefore, the tip of the cantilever is chosen to be of spherical shape with a diameter of a few µm. Using a common sharp tip, the same setup can also be used to characterize the roughness (and potentials) on all scales with lateral resolution $<$10 nm. In the vertical direction, we implement a common tapping mode method, where the height adaptation with 0.2 nm resolution is enabled by the three linear piezo-electric stages otherwise used for tilt adjustment of the lower plate.

In the second configuration (not shown in this paper) the KPFM is turned upside down and the lower plate is replaced by the cantilever holder, allowing an in situ measurement of the upper plate's lower surface or the electrostatic shield's potential distribution in the same way as described above. With these two configurations, we can achieve a complete characterization of all surfaces that can then be used to compute the patch potential contribution to the measurements based on actual data instead of statistics.

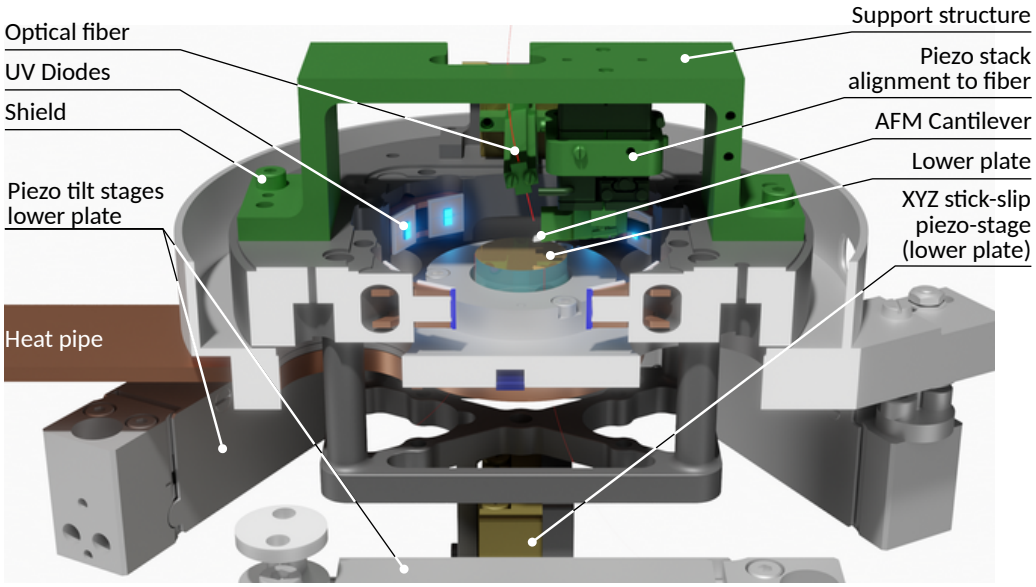

Figure 6. Rendering of the AFM/KPFM configuration for measurements of potentials and topology of the lower plate.

It has been demonstrated that frequency-modulated (FM)-KPFM is able to achieve higher resolutions than amplitude-modulated (AM)-KPFM, as artifacts caused by the capacitance of the cantilever are more prominent in AM-mode operation [128–130]. On the other hand, lower bias voltages in AM KPFM reduce the distance dependence of the minimizing potential [131] and result in a higher reliability for the topological loop to prevent damaging the surface or the tip [132]. Recently, the introduction of heterodyne detection methods in both AM [133] and FM [134] KPFM has been shown to yield improved resolution and speed. In CANNEX, we intend to use heterodyne AM. In contrast to the literature, our cantilever is excited at its resonance frequency ω_{c0} electrostatically. This method is less prone to artifacts and offers increased resolution compared to both classical AM and FM KPFM. Moreover, heterodyne KPFM enables us to detect the contact potential difference simultaneously to $\partial^2 C/\partial a^2$, where C is the capacitance and a is the distance between the tip and the surface [134–136]. In the potential domain, we expect the resolution to be better than 0.1 mV [137]. This setup can easily be adjusted to any homo- or heterodyne detection method. If necessary, we will diverge from the intended use of heterodyne AM-KPFM if other methods prove to lead to higher resolutions.

2.5. Optical Detection System: Force and Distance Measurements

A major problem in the proof of principle for CANNEX [103,104] was the parasitic coupling of AC signals into the cavity. We have, therefore, replaced the capacitive detection system by a entirely optical one to detect all relevant parameters. Electrical potentials between the plates are now defined by a single source driven by the active potential compensation circuit described in Section 2.2.

2.5.1. Force and Force Gradient Detection

CANNEX uses Fabry–Pérot cavities formed by the polished ends of optical fibers and the reflecting surfaces of the sensor plate to measure the extension of the latter and its distance to the opposing lower plate. An overview of the complete optical setup is given in Figure 7.

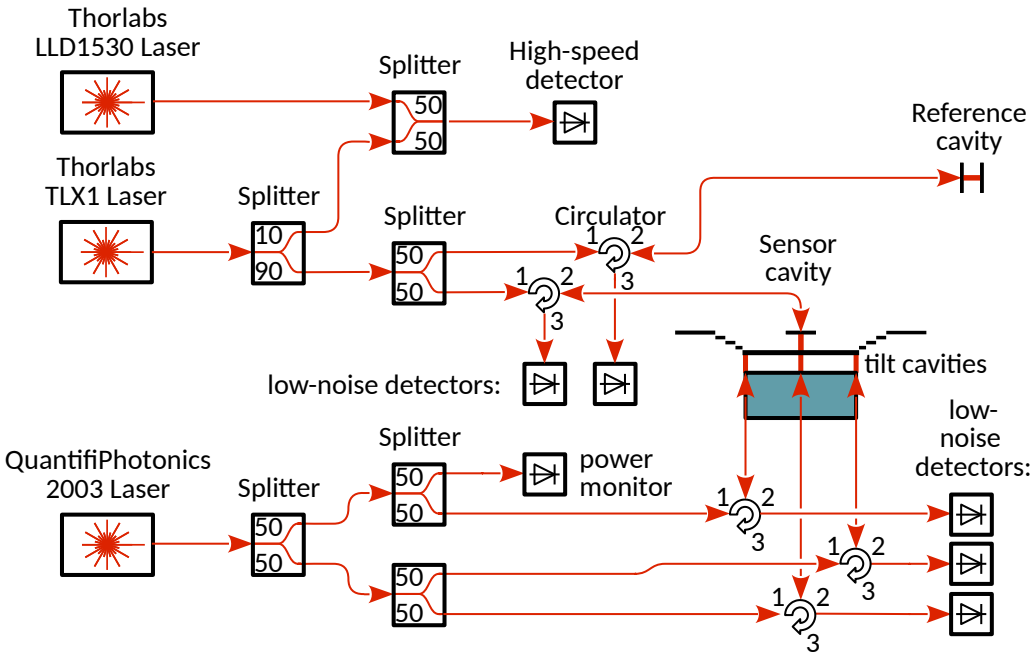

Figure 7. Complete schematic of the optical detection system.

A periodic force F or movement of the sensor base z_0 at circular frequency ω leads to a displacement amplitude Δz of the sensor plate according to the transfer functions

$$T_{Fz} \equiv \frac{\Delta z}{F} = \frac{1}{m\left(\omega_0^2 - \omega^2 - \partial_a F/m - \mathrm{i}\omega\omega_0/Q\right)}, \quad \text{and } T_{z_0 z} \equiv \frac{\Delta z}{z_0} = \frac{\omega^2}{\left(\omega_0^2 - \omega^2 - \partial_a F/m - \mathrm{i}\omega\omega_0/Q\right)}. \tag{4}$$

Here, $Q \approx 10^4$ is the quality factor of the sensor.

Note that at $\omega = 0$, the transfer function reduces only approximately to Hooke's law, as $T_{Fz} \to (m\omega_0^2 - \partial_a F)^{-1} = (k - \partial_a F)^{-1}$. We denote the sensor spring constant by k, the free resonance frequency by ω_0, and the effective mass by m, which is larger than the physical plate mass m_0 due to the dynamical contribution of the spring elements. At the smallest separations $a \to 3\,\mu\mathrm{m}$, the ratio $(\partial_a F)/k$ reaches values up to 0.01 such that the force gradient $\partial_a F$ cannot be neglected when evaluating DC extension data. We, therefore, have to either measure or calculate $\partial_a F$ for all measurements. The sensor resonance frequency ω_r (defined as the frequency at which the mechanical system has $\pi/2$ phase shift with respect to the sinusoidal force excitation signal) shifts according to

$$\omega_r = \sqrt{\omega_0^2 - \frac{\partial_a F}{m} + \frac{1}{m}\mathcal{O}\left((\partial_a^2 F) T_{Fz} F\right)}, \tag{5}$$

where the relative error due to the last term is smaller by four orders of magnitude than the effect of the second at all separations.

We use the single interferometer above the sensor (see Figure 7, 'sensor cavity') to synchronously detect the DC extension Δz in response to constant forces acting onto the plate, and the dynamical response $\Delta z(t)$ to an electrostatic excitation $F_{\mathrm{exc}}(t) = (\varepsilon_0/4a^2) V_{\mathrm{exc}}^2 \cos\omega_r t$ (with the vacuum permittivity ε_0).

Due to the voltage V_{exc} applied between the plates at frequency $\omega_r/2$. Using a phase-locked loop (PLL), we can track ω_r and detect the shift $\Delta\omega = \omega_r - \omega_0$ of the resonance frequency, from which we extract $\partial_a F$ by inverting Equation (5). For measurements in Xe gas, the sensor is over-critically damped, such that $\Delta\omega$ cannot be measured. In these measurements, we move to $a > 10\,\mu\mathrm{m}$, where $\partial_a F/k \ll 10^{-2}$ and the error by using the computed values for the force gradients due to the dominant electrostatic and Casimir force contributions is negligible.

The value of $\Delta z(t)$ is extracted from the optical signal

$$S = S_A + S_B \cos \frac{4\pi(d - \Delta z)}{\lambda}, \tag{6}$$

where the offset S_A and the amplitude S_B are determined by the optical and geometric properties of the cavity, the laser power P_L and the wavelength λ, and the sensitivity of the detector. All appearing parameters are calibrated independently (see Section 2.5.2). In order to maximize the sensitivity of S to Δz in Equation (6), we need to adjust λ such that $\cos 4\pi d/\lambda = 0$, which we call the 'quadrature point'. Before data taking, we ensure the latter condition by performing a sweep of λ at large distance, where Δz can be calculated with sufficient precision. The sweep data are then fitted by Equation (6), with free parameters S_A, S_B, and d. Note that for all a the interferometric cavity size d only changes by $|\Delta z| \ll |d - \lambda/2|$ (the size of a fringe) due to the sensor's reaction to forces applied between the two plates. We can, thus, measure d and adjust λ to be at quadrature. The same sweep method with a wide range of λ allows us to measure the absolute distance a_i between the two plates at the position of the lower three interferometers; see Figures 1 and 7. We extract a_i either from fits as described above or from the peaks appearing in the Fourier transformed data $\tilde{S}(d)$ of $S(\lambda)$. Which method is used depends on the cavity size. At large $a \gtrsim 20\,\mu\text{m}$, where sufficiently many fringes can be covered by the modulation range (1520–1620 nm) of the QuantifiPhotonics 2003 laser (QuantifiPhotonics Ltd., Auckland, New Zealand) laser, the Fourier method gives fast and accurate values of a_i, while at the smallest separations, not even one fringe can be covered and only the fit method can be applied.

The optical paths $2d$ and $2a_i$ of our cavities change with the vacuum pressure and are significantly influenced during the measurements in Xe gas. For this reason, we use an auxiliary fixed-distance cavity made of a material with an effectively zero thermal expansion coefficient, sourced by the same laser driving the upper sensor cavity. Being located next to the sensor, this cavity gives a reference signal $S_\text{R}(P_L, \lambda, \rho_G)$ depending on the density ρ_G of the gas and fluctuations in both the laser power and wavelength. For the three interferometers below the sensor, we use a power monitor to eliminate power fluctuations from the signal. As all excitations and resonances are well below 20 Hz, we use slow low-noise detectors with cutoff-frequency 1 kHz to eliminate high-frequency noise.

Measurements in the interfacial and Cavendish configurations are performed in sweeps starting at the maximum separation $a_\text{max} = 30\,\mu\text{m}$, reducing the separation for each measurement point in discrete logarithmic steps towards $a_\text{min} = 3\,\mu\text{m}$. Before each sweep, a full re-calibration is performed (see below) to cancel drifts. The cavity size d and wavelength λ are re-calibrated before each single measurement point. For measurements in Xe, a is kept constant and sets of several consecutive measurements are performed at the same pressure. Each set is preceded by a full calibration with d and λ recalibrations in between single measurements.

2.5.2. Calibration

In order to perform an absolute measurement of forces, we need to calibrate all the optical, mechanical, and electric properties of our detection system. Some calibrations are invalidated only by ageing for which one measurement per experimental campaign is sufficient, while others have to be repeated as often as possible to compensate drift. Constant offsets requiring only few re-calibrations concern the dependence of laser power on the wavelength, transmission functions of wiring and electronics, etc., taken into account in the error calculations in Section 3. The remainder of this Section focuses on the frequent calibration of physical properties of the sensor and optical system. Mechanically, the sensor response is influenced by thermal fluctuations, long-term changes in the residual water layer on its surface, and surface charges. Even if these effects are expected to be relatively small, only a calibration can exclude them with certainty.

We start by re-calibrating the time-dependent wavelength offset of our lasers using a second laser with wavelength locked to an acetylene transition at $\lambda_\text{ref} = 1532.832\,30(8)$ nm

and a beat technique [138]. For this method, the output of the tested laser is combined with that of the reference laser and lead to a high-frequency detector (see Figure 7). Then, the λ_{set} setting of the TLX1 is adjusted to result in a minimum beat frequency, $\Delta f = (c/2)(\lambda_{set}^{-1} - \lambda_{ref}^{-1})$ (with c the speed of light), using a lock-in amplifier. From the difference between λ_{set} and λ_{ref}, and from the residual Δf (resolution of λ_{set}), we can determine the (constant) error in λ_{set} to within about 0.1 pm.

Next, in a similar way as in the proof of principle [103], we increase the plate separation in high vacuum to $a_{cal} \approx 5\,\mathrm{mm}$, where all interactions (electrostatic, Casimir, and gravity) between the plates fall off by at least two orders of magnitude with respect to their values at $a = 30\,\mu\mathrm{m}$. In this position, the properties of the sensor cavity (see Figure 7) and the reference cavity are determined by a wavelength sweep as described above. Subsequently, at $\lambda_{set} \approx \lambda_{ref}$, d is adapted iteratively to match that of the reference cavity such that both cavities are of the same size and at quadrature. Then, a precisely known electrostatic excitation is applied at frequency ω_{exc} that is swept over a range from $\omega_0/2$ to $2\omega_0$ and the signal amplitude and phase are decoded by a lock-in amplifier. Finally, a DC voltage is applied between the plates and its value is swept over a range around zero, resulting in similar signal levels as in the actual measurement of the Casimir force. Both the extension Δz and the frequency shift $\Delta\omega$ in response to the electrostatic force are recorded. Then, a synchronous fit of data from both sweeps (frequency and voltage) to Equations (4) and (5), considering the signal non-linearity from Equation (6), with all separately recorded voltages, power fluctuations (see below), and calculated forces and their gradients contributing to Δz at $a = a_{cal}$, is performed. This fit results in accurate values for m, ω_0, and Q.

3. Error Budget

We already published a complete error budget [99] on the basis of a preliminary design considering a two-stage SAS, but at a location inside a (seismically and thermally) noisy lab in Vienna. The leading reason to relocate CANNEX to COBS is significantly lower environmental disturbances. Here, we update the previous error budget, firstly, with respect to the new location, and, secondly, for the final design and the characteristics of the actually used devices. As we show subsequently, the final design implements major improvements with respect to the previous conservative estimations, leading to expected final sensitivities of $0.259\,\mathrm{nN/m^2}$ and $0.0179\,\mathrm{mN/m^3}$, with projected uncertainties (of statistical (stat.), systematic (syst.) and constant (const.) errors) $0.119\,\mathrm{nN/m^2}$(stat.+ syst.) + $0.139\,\mathrm{nN/m^2}$(const.) and $8.6\,\mu\mathrm{N/m^3}$(stat.+ syst.) + $9.3\,\mu\mathrm{N/m^3}$(const.), respectively, at the 68% confidence level (1σ) for 100 days of measurements at $a = 20\,\mu\mathrm{m}$. These figures represent an improvement by factors 2 and 30 for measurements of the pressure and pressure gradient between the flat parallel plates, respectively, in comparison to our previous estimate.

3.1. Seismic Noise

As shown in Figure 2 above, the seismic noise at the COBS is significantly lower than in Vienna at all frequencies above the micro-seismic peak. Due to a near seismically active zone in the Pannonian basin south of Vienna, earthquakes of low magnitude are frequent. However, the observatory houses official geomagnetic, seismic, and meteorological surveillance stations, including several STS-2 seismometers (Streckeisen GmbH, Pfungen, Switzerland), which can be used not only to veto affected data but also to correct variations in the gravitational acceleration g due to Earth tides and irregular local mass shifts at the location of CANNEX.

The lower seismic noise at the COBS relaxes our requirements for the SAS such that the one-staged system described in Section 2.1 suffices. In Figure 8, we show the expected spectral seismic disturbance together with the limits from RMS noise, signal non-linearity, and the signal-to-noise ratio (SNR). At all frequencies at COBS, the passive SAS alone already fulfills the requirement with 53 dB and 22 dB (amplitude) buffers in the horizontal and vertical directions, respectively, around the sensor resonance. Near the resonance of the GAS filter (assumed 100 mHz) in the vertical direction, the buffer reduces to 14 dB.

Such a low resonance frequency is usually not achieved by a passive system but since active feedback can lower the resonance frequency and the corresponding amplitude even further, we use this assumption in our calculations. At frequencies below 30 mHz, RMS noise becomes an issue. However, all data below $10\,\mathrm{s}^{-1}$ will be corrected by STS-2 data, which eliminates the constraint. Furthermore, the current error budget does not include additional damping by active feedback, as the respective design is not yet complete. We conservatively expect 2 dB additional damping around the sensor resonance and about twice this reduction for the amplitude of the primary GAS filter and pendulum resonances.

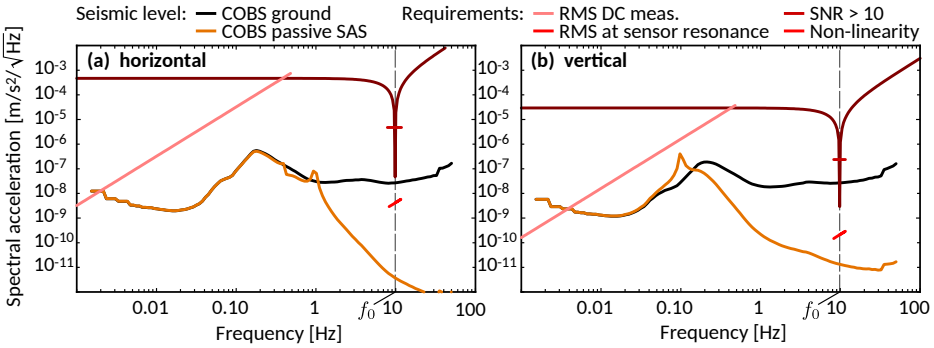

Figure 8. Numerical result of the passive (**a**) horizontal and (**b**) vertical seismic background on the core chamber, compared to updated requirements (red lines) representing upper limits (for details see [99]). The vertical dashed lines indicate the position of the vertical sensor resonance.

3.2. Detection Noise

For the error budget, we have to consider the time-dependent offsets and noise in all the calibrated quantities, parameters, inputs, excitation and detection signal paths, and measurement devices. With respect to the previous error budget, we now have detailed and specific information about most quantities available, which allows us to compute the final error level expected for the measurements.

General boundary conditions are a total number of 100 distance sweeps, each including a re-calibration of the cavity sizes, laser wavelength and sensor parameters, and elimination of seismic disturbances at frequencies lower than $(10\,\mathrm{s})^{-1}$ using seismometer data. In the following, we construct the error budget by first analyzing the signal paths for DC and AC measurements independently, leading to a voltage and frequency signal, respectively. mentioned. Please confirm or revise naming "first step" clearly. Those signals are then converted to the pressure and pressure gradient using the calibrated mechanical properties of the sensor. In each of these two stages and for the calibration, we perform a detailed and—to the best of our knowledge—complete error analysis assuming small and normally distributed statistical errors and time-dependent drifts wherever manufacturer data are available. Details on each considered error are given in Appendix A.

For DC signals of the extension Δz, we consider variations δd in the cavity size d due to seismic vibrations and thermal drift. Note that errors σd in the cavity size determination are constant offsets that need to be considered only for the conversion to a force below, as they are nullified for the voltage signal at quadrature. Wavelength errors $\delta\lambda$ are due to the laser bandwidth and spectral frequency noise as well as time-dependent wavelength accuracy errors $\sigma\lambda(t)$. The latter can be reduced by first assuring the independence (specifications obtained directly from the manufacturer) of the offset $\sigma\lambda(\lambda)$ from the wavelength, for all λ values in the tuning range of the TLX1 laser, using a spectrometer with less than 0.1 pm accuracy. Then, during operation, $\sigma\lambda$ will be measured repeatedly (before each force measurement) at one single wavelength using a frequency-locked reference laser as described above. According to the manufacturer's information, the uncertainty of the reference laser wavelength is mainly limited by thermal drift. The given uncertainty value $\sigma\lambda = 0.08\,\mathrm{pm}$ is specified for $\delta T = 3.5°$, for which we reduce this value by a factor 0.1/3.5 for operation at COBS. For the signal error, we further consider the relative power fluctuations δP_L of the

laser leading to intensity fluctuations affecting both the signal of the measuring cavity and the one of the reference cavity, S_R. As both signals are measured independently, this allows us to normalize the signal in realtime. Both optical signals contain stochastic noise δV_det of the detectors, and δV_DAQ of the two Keysight 34470A voltmeters, discretization error δV_alias, voltage offsets $\sigma V_\mathrm{DAQ}(T)$, depending on fluctuations of the ambient temperature T, and a stochastic component for cable pickup noise. This leads to an expression for the total measured signal V_sig, where for brevity, we combine for some quantities the respective constant and systematic errors $\sigma X(t)$ that may contain drift depending on time t and the stochastic noise δX as $\delta X(t)$:

$$V_\mathrm{sig} = \frac{V_\mathrm{R}(0) + \delta V_\mathrm{R0}}{V_\mathrm{R}(t) + \delta V_\mathrm{R}} \left(\delta V_\mathrm{DAQ}(t) + \delta V_\mathrm{det} + [1 + \delta P_\mathrm{L}(t)] \left[S_A + S_B \frac{4\pi[d + \delta d(t)]}{\lambda + \delta\lambda(t)} \right] \right), \quad (7)$$

$$\text{with } V_\mathrm{R}(t) = \delta V_\mathrm{DAQ}(t) + \delta V_\mathrm{det}(t) + [1 + \delta P_\mathrm{L}] \left[S_{A,\mathrm{R}} + S_{B,\mathrm{R}} \frac{4\pi[d_\mathrm{R} + \sigma_\mathrm{R}]}{\lambda + \delta\lambda(t)} \right].$$

The reference signal $V_\mathrm{R}(0)$ is measured before the start of the measurements with long integration time τ_R (see below), determined from the minimum between noise averaging and the rising influence of long-term variations (drift). The measured ambient temperature in the tunnel at COBS generally changes over periods of weeks rather than hours and has a typical fluctuation amplitude of 5×10^{-3} °C per day. As a worst case (in the case of work being performed in the tunnel), we consider a sinusoidal diurnal temperature deviation with peak amplitude 0.1° with zero transition at the start of the measurement. For the resulting offset errors, we use manufacturer specifications for the voltmeters amended by noise measurements with the actual devices. The lasers are temperature-stabilized but nonetheless are affected by changes in T. For the TLX1, the power noise has a $1/f$ characteristic for frequencies below 10 Hz extrapolated from -105 dBc at 10 Hz to smaller frequencies, and flattening off at -40 dBc at around 2×10^5 s due to the power regulation circuit; specifications were confirmed by actual measurements over 3 h [139]. We computed the Allan deviation from these data, showing no clear minimum but flattening around 5 ks). The laser frequency noise δf_L is most pronounced around 1 Hz and reduced for smaller frequencies by a dither keeping the DC value of the wavelength constant within 10 kHz (approximately 0.1 fm). Due to the periodic laser frequency offset calibration between measurements, continuous power normalization, internal temperature calibration of the data acquisition system, and all-year temperature stability at COBS, any long-term drift is expected to be insignificant for the period of data taking (100 days). We, thus, cut off drift contributions ($\delta V_\mathrm{DAQ}(t)$, $\delta f_L(t)$, δP_L) at the integration time $\tau = 1 \times 10^{-5}$ s by integrating over the fluctuation spectra from $f = t^{-1}$ to ∞ with a cutoff function, $f_I(f) = 1/(1 + 2\pi f\tau)$, provided by the detector with $\tau = \tau_\mathrm{det} = 10^{-3}$ s and $\tau = t$ for a variable integration time (2 s for DC measurements and 83 s for AC measurements, 1000 s with averaging for one measurement point) to obtain the respective RMS error. This procedure replaces the $1/\sqrt{\tau}$ factor considered generally for stochastic quantities for all errors for which we have spectral information. The cavity size d has an uncertainty due to seismic disturbances ($\delta d = 4\,\mathrm{pm_{RMS}}$ for $\tau = 2$ s and $\delta d = 2.8 \times 10^{-2}$ pm for $\tau = 1000$ s). Another contribution to δd comes from the thermal drift. Based on the thermal expansion coefficients and geometry, we expect an effective coefficient of about 5×10^{-8} m/°C (with rather large uncertainty), which translates to 5 pm maximum amplitude. This error needs to be evaluated carefully but our results here indicate that in order to keep the effect of this error small, we need to re-calibrate d after each measurement point. Note that for δV_sig,constant errors in d are irrelevant, as they cancel out by subtracting the signal from the one at a_cal.

Without error normalization (i.e., by setting $V_\mathrm{R}(t) = V_\mathrm{R}(0)$), we obtain for an integration time of $\tau_i = 1000$ s a total (statistical and systematic) detection error, $\delta V_\mathrm{sig} = 4.85 \times 10^{-6}$ V, which is dominated by stochastic δP_L at short times and $\delta\lambda$ drift at times larger than approximately 100 s. Including the reference measurement, which has a fixed-length cavity without distance fluctuations or temperature drift, this figure can be reduced (assuming even 10% mismatch between sensor and reference cavity) to 8.90×10^{-7} V,

which is dominated by seismic vibration at short times, and δV_{DAQ} at $\tau \gtrsim 500$ s. Error contributions for a single measurement and 500 sequential measurements comprising one force (gradient) measurement are given in Table 1. For comparison, a pressure of 1 nN/m^2 would result in a signal of 3.03×10^{-6} V. Note that δV_{DC} has no significant dependence on a.

Table 1. Components of the DC signal error for fixed $a = 3\,\mu$m and $\tau_{\mathrm{DC}} = 2$ s for a single datum ($N = 1$) and for $N = 500$ ($\tau = 1000$ s) representing one single measurement point, considering drift models and constant deviations $\sigma_{\mathrm{R}} = d + 10$ nm, $S_{A,\mathrm{R}} = 1.1 S_A$, and $S_{B,\mathrm{R}} = 1.1 S_B$. See text for details.

Error	**Symbol**	**Value [V]**		**Error Type**
		$N = 1$	$N = 500$	
Detector noise	δV_{det}	6.0×10^{-8}	2.7×10^{-9}	stat.
DAQ input noise	δV_{DAQ}	8.9×10^{-8}	4.0×10^{-9}	stat.
Laser power fluct. (canceled)	δP_{L}	0	0	stat.
Laser bandwidth	$\delta\lambda$	2.1×10^{-12}	9.3×10^{-14}	stat.
Laser frequency noise	$\delta\lambda$	1.6×10^{-10}	7.6×10^{-12}	stat.
Seismic vibrations	δd	3.3×10^{-5}	1.3×10^{-7}	stat.
Tot. ref. measurement noise (72 h)	δV_{R}	8.2×10^{-8}		stat.
DAQ input error	$\sigma V_{\mathrm{DAQ}}(t)$	2.3×10^{-11}	1.3×10^{-11}	syst.
Laser wavelength drift	$\sigma\lambda(t)$	7.0×10^{-13}	1.3×10^{-10}	syst.
Cavity size drift	$\sigma d(t)$	2.9×10^{-9}	8.3×10^{-7}	syst.
Tot. ref. measurement error (72 h)	σV_{R}	7.9×10^{-7}		syst.
DAQ calibration	σV_{DAQ}	1×10^{-7}		const.
Tot. ref. measurement error (72 h)	σV_{R}	1×10^{-7}		const.

For AC measurements of the frequency shift, $\Delta\omega = 2\pi\Delta f$, we consider the inherent phase stability of the lock-in amplifier and PLL feedback circuitries, δf_{LI} and δf_{PID}, respectively. There is no simple expression, such as Equation (7) that could be used for direct error propagation, since the frequency measurement involves numerical operation of the PLL. Therefore, we measured the noise and stability of the actual lock-in amplifier and feedback using a first-order passive RC-lowpass filter as the test device. This measurement results in higher noise than in measurements with the CANNEX sensor, as the Q-factor is significantly lower. Aiming to give a (quite) conservative estimate, we consider these measurements representative, nonetheless. Furthermore, we consider the uncertainty in the ω_0 calibration obtained from simulations (see below). Constant offsets σf of the lock-in amplifier clock are reduced to $<5 \times 10^{-10}$ Hz by referencing the PLL to an external Rubidium clock. In addition, the Allan deviation of the clock between calibrations (once per 24 h) could give an error at the level 0.05 ppm/°C, which we take into account. Voltage noise sources as described for DC measurements, vibrations, and laser frequency noise are considered indirectly by expressing the amplitude noise of the sensor signal in terms of a phase ϕ at the zero transition, $\delta\phi = (\partial V/\partial\omega t)^{-1}\delta V$ and $\delta\phi = [\partial \mathrm{Arg}(T_{Fz})(\omega)/\partial\omega]\delta\omega$, where Arg() is the argument function. This computation over-estimates the real phase error by at least a factor of two but we consider it as a worst case. We obtain $\delta f_V = \omega_0\lambda/(16\pi Q\Delta z_{\mathrm{exc}})\delta V$, with the excitation displacement amplitude Δz_{exc} depending on V_{exc} and a, and $\delta V_{\mathrm{sig}} = 7.33 \times 10^{-7}$, $\sigma V_{\mathrm{sig}} = 5.58 \times 10^{-7}$ V, evaluated as described above for DC measurements but with $\tau_i = 83$ s. Note that we adapt $V_{\mathrm{exc}}(a) = V_{\mathrm{exc}}(10\,\mu\mathrm{m}) \times (a/10\,\mu\mathrm{m})^{3/2}$ to render the excitation and associated shift in the sensor resonance frequency independent of a. The same uncertainties lowered by longer integration time are used for the calibration of ω_0 (see Section 2.5.2). We then obtain the total frequency shift measurement error by adding all the constant, systematic, and statistical errors listed in Table 2, as described in Section 3.3 below, leading at the shortest separation $a = 3\,\mu$m to a single point ($\tau = 1000$ s) frequency determination error $\delta f = 4.68 \times 10^{-7}$ Hz dominated by δf_{LI} at all integration times (up to $\tau \sim 10^4$ s) and $\sigma f = 8.31 \times 10^{-9}$ Hz. This

has to be compared by a minimum signal $\Delta f = 4.95 \times 10^{-6}$ Hz for a pressure gradient of $1\,\mathrm{mN/m^3}$.

Table 2. Components of the AC signal error for fixed $a = 3\,\mu\mathrm{m}$ and $\tau_{\mathrm{AC}} = 83$ s for a single datum ($N = 1$) and for $N = 12$ ($\tau = 1000$ s) representing one single measurement point, considering drift models. See text for details.

Error	Symbol	Value [Hz]		Error Type
		$N = 1$	$N = 12$	
Signal noise	δf_V	3.9×10^{-9}	1.4×10^{-10}	stat.
f-detection	δf_{PID}	2.2×10^{-6}	6.3×10^{-7}	stat.
PLL frequency noise	δf_{LI}	1.8×10^{-9}	5.2×10^{-10}	stat.
Signal drift	$\sigma f \delta_V(t)$	3.0×10^{-10}	1.6×10^{-11}	syst.
PLL phase stability	$\sigma f_{\mathrm{LI}}(\tau)$	8.8×10^{-10}	1.1×10^{-8}	syst.
Resonance freq. error	$\sigma\omega_0$	2.3×10^{-10}	2.3×10^{-10}	syst.
Signal noise	σf_V	4.5×10^{-9}		const.
PLL phase error	σf_{LI}	5×10^{-10}		const.
Resonance freq. error	$\sigma\omega_0$	8.8×10^{-11}		const.

The measured frequency shift can be converted to a total force gradient by inverting Equation (5), where we require the effective mass m and ω_0 from the calibration. In order to determine the error on m, Q, and ω_0, we performed a Monte Carlo simulation of complete calibration data on V_{sig} and ω_r considering all the voltage and frequency measurement errors discussed in this Section as normally distributed random quantities with the known width, and offsets depending on time. For frequency data, we created voltage signals containing δV_{sig} and extracted the resulting amplitude and phase using a software lock-in amplifier. We then selected 300 arbitrary sets of frequency shift and voltage shift data, from which we extracted values for m, Q, ω_0, as described in Section 2.5.2. Eventually, we computed the standard deviation of the fit results, which we interpret as a systematic error (i.e., statistical, averaging with the number of calibrations only). The difference between the mean fit value and the originally used parameter value is representative of a constant error for this parameter. We obtain $\delta m = 58.6 \times 10^{-12}\,\mathrm{kg}$, $\sigma m = 1.42 \times 10^{-12}\,\mathrm{kg}$, $\delta Q = 1.30 \times 10^{-5}$, $\sigma Q = 2.83 \times 10^{-2}$, $\delta\omega_0 = 1.44 \times 10^{-9}\,\mathrm{rad/s}$, $\sigma\omega_0 = 4.4 \times 10^{-11}\,\mathrm{rad/s}$. For m and ω_0, the constant errors are significantly smaller than the systematic ones, which indicates that repeated calibrations may be required to average out the systematic errors. For further computation, we use the constant frequency detection error $\sigma f = 5.53 \times 10^{-10}\,\mathrm{Hz}$ for $\sigma\omega_0/(2\pi)$ instead of the smaller constant error from the simulation given above. We consider a measurement scheme in which one calibration is performed per distance sweep (i.e., per day) and assume that due to the thermal stability of the system, σm and $\sigma\omega_0$ can be reduced as $1/\sqrt{N_{\mathrm{cal}}}$ with the number N_{cal} of calibrations. We then resolve $\omega_r + \delta\omega_r(t) = \sqrt{(\omega_0 + \sigma\omega_0)^2 - \partial_a F/(m + \sigma m)}$ for the total gradient $\partial_a F$, and propagate all errors. To evaluate the latter expression, we require a value for ω_r, where we assume the Casimir force gradient (see Section 4.1) and an electrostatic interaction $\partial_a F_{\mathrm{ES}} = \varepsilon_0 A V^2/a^3$, with $V = 0.5\,\mathrm{mV} \times (a/10\,\mu\mathrm{m})^{3/2}$ for the excitation and the sensor interaction area A. Using the quantities just above and the frequency determination error $\delta\Delta f(t)$, we finally obtain the errors listed in Table 3 for $a = 3\,\mu\mathrm{m}$, yielding a total pressure gradient detection errors $\delta\partial_a F/A = 0.097\,\mathrm{mN/m^3}$(stat. + syst.) and $\sigma\partial_a F/A = 0.001\,\mathrm{mN/m^3}$(const.), dominated by the frequency measurement error δf_{PID}, which is based on our test measurements at low Q-factor.

Table 3. Components of the pressure gradient error for fixed $a = 3\,\mu\text{m}$ and $\tau_{\text{AC}} = 83\,\text{s}$ for a single datum ($N = 1$) and for $N = 12$ ($\tau = 1000\,\text{s}$) representing one single measurement point, considering drift models.

Error	Symbol	Value [N/m^3]		Error Type
		$N = 1$	$N = 12$	
Frequency detection error	δf	3.3×10^{-4}	9.4×10^{-5}	stat.
Mass calibr. uncertainty	σm	4.8×10^{-5}	4.8×10^{-5}	syst.
Resonance freq. uncert.	$\sigma\omega_0$	4.6×10^{-8}	4.6×10^{-8}	syst.
Frequency detection error	$\sigma f(t)$	1.4×10^{-7}	1.6×10^{-6}	syst.
Mass calibration error	σm	1.2×10^{-6}		const.
Resonance freq. error	$\sigma\omega_0$	1.1×10^{-7}		const.
Frequency detection error	σf	1.1×10^{-7}		const.

The measured DC signal voltage can be interpreted as an extension $\Delta d = F\,T_{Fz}|_{\omega\to 0}$ of the sensor due to a force F and its transfer function T_{Fz}, given in Equation (4). In order to evaluate the latter quantity, we require the errors of $\partial_a F$, m, d, as well as the optical amplitude S_B and V_{sig}. Eventually, we propagate the errors according to

$$F(a) = \frac{1}{4\pi}\left[\partial_a F + \delta\partial_a F(t) - (m+\sigma m)(\omega_0+\sigma\omega_0)^2\right] \times \left[4\pi\sigma d - (\lambda+\delta\lambda(t))\text{asin}\left(\frac{V_{\text{sig}}+\delta V_{\text{sig}}(t)}{S_B+\sigma S_B} + \sin\frac{4\pi\sigma d}{\lambda+\delta\lambda(t)}\right)\right], \tag{8}$$

resulting in an error of $\delta F/A = 0.324\,\text{nN/m}^2$ and $\sigma\partial F/A = 0.167\,\text{nN/m}^2$, for a single measurement of 1000 s at $a = 3\,\mu\text{m}$ dominated by the uncertainty δV_{sig} and uncertainty σd in the cavity size. The value of σd is the parameter error obtained by the wavelength sweep fit during repeated calibrations, for which we categorize it as systematic error, influenced by thermal variation. The corresponding offset (constant error) was below machine precision in the fit. We, thus, consider in the final budget a factor $1/\sqrt{N_{\text{sweep}}}$ with $N_{\text{sweep}} = 500$ for σd. All errors contributing to $\delta F/A$ are listed in Table 4. These results highlight again the need for thermal stability and vibration attenuation as well as proper thermal design. In Figure 9a,b, we show the detection errors for the pressure and its gradient as a function of the integration time. In light of the considerations of this section, the previous error budget [99] is thereby improved by up to one order of magnitude in both measured quantities. For the pressure error, the main contributions are the drift and uncertainty (σd) in the cavity size, the DC measurement noise, which, in turn, depends on vibrations, and the uncertainty σm in the mass of the sensor. For the pressure gradient, the most important contributions come from the frequency measurement that depends strongly on the internal stability of the PLL and the sensor mass. The temperature drift is a crucial parameter influencing most systematic errors considered here.

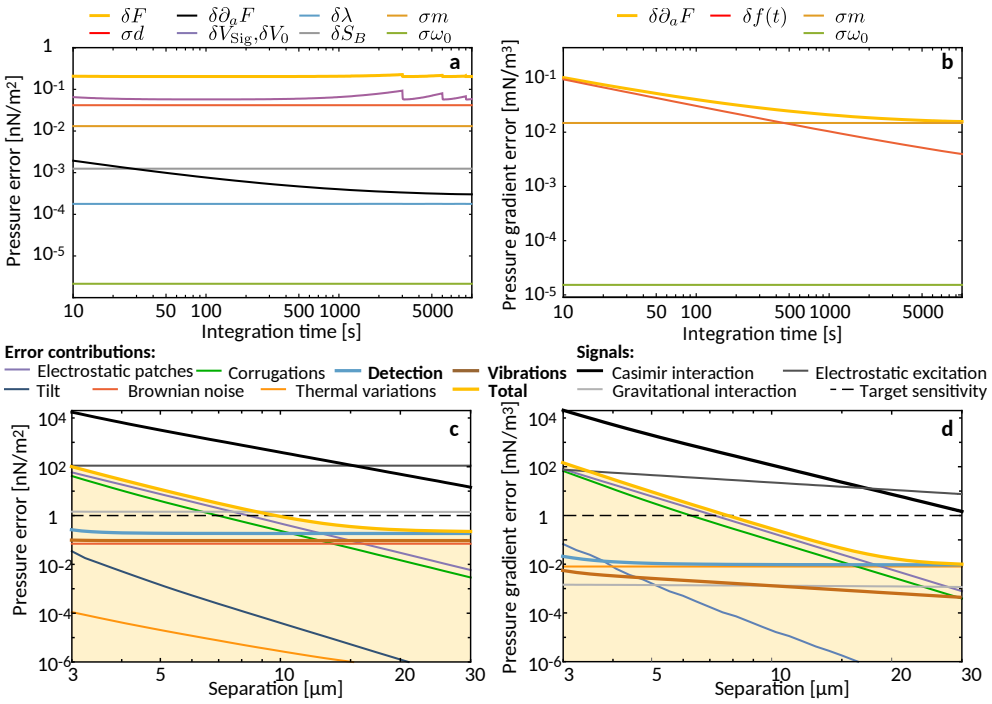

Figure 9. Updated error budget for CANNEX. (**a**,**b**) Time dependence of the detection error in the pressure and pressure gradient, respectively, for a single calibrated measurement at fixed separation $a = 3\,\mu\text{m}$. (**c**,**d**) Error contributions from Ref. [99] with only detection errors and seismic errors updated. Note that here, δX denotes the total error of quantity X and σX denotes the the corresponding combined systematic and constant error.

Table 4. Components of the pressure error for fixed $a = 3\,\mu\text{m}$, $\tau_{\text{DC}} = 2$ s and $\tau_{\text{AC}} = 83$ s for a single datum ($N = 1$) and for $N = 12$ ($\tau = 1000\,\text{s}$) representing one single measurement point, considering drift models.

Error	**Symbol**	**Value [N/m^2]**		**Error Type**
		$N = 1$	$N = 12$	
Force gradient error	$\delta\partial_a F$	6.0×10^{-12}	5.0×10^{-13}	stat.
DC signal error	δV_{sig}	1.8×10^{-10}	2.0×10^{-12}	stat.
Zero force DC signal error	δV_0	1.8×10^{-10}	2.4×10^{-11}	stat.
Mass calibr. uncertainty	σm	4.1×10^{-11}	1.2×10^{-11}	syst.
Resonance freq. uncertainty	$\sigma\omega_0(t)$	8.6×10^{-16}	2.5×10^{-16}	syst.
Cavity size error	$\sigma d(t)$	4.2×10^{-10}	1.2×10^{-10}	syst.
Wavelength drift	$\sigma\lambda(t)$	1.4×10^{-12}	4.0×10^{-13}	syst.
Fringe amplitude uncertainty	σS_B	1.3×10^{-11}	3.6×10^{-12}	syst.
Force gradient error	$\sigma\partial_a F$	6.6×10^{-13}	1.9×10^{-13}	syst.
DC signal error	σV_{sig}	9.0×10^{-11}	4.9×10^{-11}	syst.
Zero force DC signal error	σV_0	9.1×10^{-11}	1.7×10^{-10}	syst.
Mass cal. uncertainty	σm	9.0×10^{-12}		const.
Resonance freq. uncertainty	$\sigma\omega_0(t)$	2.1×10^{-15}		const.
Cavity size error	$\sigma d(t)$	6.7×10^{-11}		const.
Wavelength accuracy	$\sigma\lambda(t)$	3.9×10^{-14}		const.
Force gradient error	$\sigma\partial_a F$	2.2×10^{-13}		const.
DC signal error	σV_{sig}	4.8×10^{-11}		const.
Zero force DC signal error	σV_0	4.8×10^{-11}		const.

3.3. Updated Error Budget

Apart from the seismic and detection errors updated above in Sections 3.1 and 3.2, respectively, we also improved our statistical methods. Following Ref. [140], we compute the total error σ_p^{tot} at probability p for N_δ statistical errors σ_j^{stat}, N_σ systematic errors σ_k^{syst}, and N_{const} independent constant errors σ_i^{const} using

$$\sigma_p^{\text{tot}} = \sum_i \sigma_i^{\text{const}} + \sqrt{t_p^2(\nu_\delta) \sum_j^{N_\delta} [\delta_j^{\text{stat}}]^2 + t_p^2(\nu_\sigma) \sum_k^{N_\sigma} [\sigma_k^{\text{syst}}(\tau)]^2}\,. \tag{9}$$

Note that constant errors occur for many devices and are not limited to the aliasing error, as mentioned in the literature [141]. For example, consider an internal calibration offset of a voltmeter due to aging that may change on timescales larger than the experimental period. Even if a traceable certified calibration is performed before the experiment, the error cannot be determined during the experiment but has to be considered as a maximum offset. Such errors are not statistically distributed (varying) over the timescales of the experiment and can only be estimated conservatively from the accuracy limit given by the manufacturer. They are linearly added and do not reduce with time. δ_j are statistical random errors varying on timescales shorter than any integration time τ, such that they properly probe a (normal) distribution and can be reduced by a factor $1/\sqrt{\tau}$. $\sigma_k^{\text{sys}}(t)$ are the (statistical components of) systematic errors. In this category, we have any offset that has changes that are quick enough to exhibit a distribution during the experiment that may probably not be sampled completely. For example, we have aliasing errors and temperature drift as well as errors of parameters determined in repeated calibrations. These errors average with the number of calibrations or the number of measurements obtained at the same conditions and parameters. $t_p(\nu)$ is the p-% point of the student distribution that depends on the number ν of degrees of freedom, $\nu_x = N_x - 1$, for x being δ or σ. Note that for $p = 0.68$ at $1\,\sigma$ level, $t_p < 1$ for which the total error is smaller than the single errors in Figure 9. For all δ_i determined from N_i individual measurements x_j, each with a total error σ_j, it is common to consider the (weighted) error of the mean

$$\delta = \left[\sum_{j=1}^{N_i} \frac{\sigma_j^{-2}(x_j - \bar{x}_w)}{\sum_{k=1}^{N_i} \sigma_k^{-2}} \right]^{\frac{1}{2}}, \quad \text{with } \bar{x}_w = \sum_{j=1}^{N_i} \frac{\sigma_j^{-2} x_j}{\sum_{k=1}^{N_i} \sigma_k^{-2}}\,, \tag{10}$$

where we have introduced the weighted mean $\bar{x}_w$. While for experimental data points, weighted quantities can differ from unweighted ones due to singular noise events, in the present estimation of the error to the total mean, it holds that $\sigma_j = \sigma\,\forall j$ for which Equation (10) reduces to the geometric mean and its error.

With the seismic and detection errors updated, we achieve the prospective error budget in Figure 9c,d. We replot the errors discussed in Ref. [99] with only the seismic and detection errors updated. All the detection errors have a mild dependence on separation due to the adaptation of V_{exc}. For details on other errors, see the detailed discussion in Ref. [99]. The detection error is the main limitation at separations $a \gtrsim 10\,\mu\text{m}$, for which the updated error budget presented here improves the prospects for measurements at large separations. Deformation errors, including the sag of the surfaces due to the measured pressures and gravity, are the second-strongest error contribution at small consider replacing. separations after residual patch effects. Using Talbot interferometry on the actual plate surfaces, we are able to measure the deformation and take it into account, for which the error given here (green line), which considers a *residual* spherical deformation of 4 nm amplitude, can be considered as an absolute worst case. Note further that local differences in the Xe density in the gas pressure modulation measurements near the surfaces due to temporal adsorption, rarefaction, or other stratification effects would cause only negligible errors not influencing the budget presented here. As the present error budget is still partially based on models,

we nonetheless present the updated prospects below considering the previous worse error budget.

4. Prospective Results

Recently [99], we gave prospective limits on axion-like interactions, Symmetron DE interactions, and measurements of the Casimir effect. Although the error budget in Section 3 demonstrates a further improvement in both the pressure and pressure gradient measurements, we conservatively keep the baseline of $1\,\mathrm{nN/m^2}$ and $1\,\mathrm{mN/m^3}$. In this section, we present updated calculations regarding equilibrium and non-equilibrium Casimir forces and limits on a range of DE interactions with updated theoretical methods and consider the final design. The latter limits supersede the previous ones in Refs. [99,102].

4.1. Casimir Effect

Casimir force experiments open an extensive window into the quantummechanical behavior of physical systems. Since the prediction of the Casimir effect in 1948 [36], the theoretical framework characterizing this phenomenon has substantially evolved, and nowadays it is situated at the intersection of very diverse areas of physics, ranging from material science and statistical physics to quantum field theory. An accurate measurement of the Casimir force has, therefore, the potential not only to offer more information about the behavior of the system's quantum fluctuations but also to test how different theories merge together, possibly providing a new window into fundamental physics.

One of the most remarkable aspects of the Casimir interaction is its dependence on the involved materials, the thermodynamic state, and the geometry of the system. Indeed, investigations have shown that by modifying these properties the Casimir force can be tuned, with interesting implications both for fundamental research and modern quantum technologies. Below, we provide a brief review of how these three aspects affect the Casimir interaction and the role that CANNEX may play in approaching them separately or also simultaneously.

4.1.1. Material Properties

Already from Casimir's original paper on the force between two parallel perfect reflecting plates, it appears clear that the properties of the materials involved in the system can play a role in determining the behavior of the force. The work by Evgeny Lifshitz in 1955 [142] underlined this aspect even further. The celebrated Lifshitz formula,

$$P_{\mathrm{Lif}}(a,T) = -\mathrm{Im}\int_0^\infty \frac{d\omega}{\pi}\int \frac{d\mathbf{k}}{(2\pi)^2}\sum_\sigma \hbar\coth\left[\frac{\hbar\omega}{2k_{\mathrm{B}}T}\right]\kappa\frac{r_1^\sigma(\omega,k)r_2^\sigma(\omega,k)e^{-2\kappa a}}{1-r_1^\sigma(\omega,k)r_2^\sigma(\omega,k)e^{-2\kappa a}}\,, \tag{11}$$

provides the force per unit of area between two parallel planar structures separated by a distance a in terms of the planes' reflection coefficients $r_i^\sigma(\omega,k)$. In Equation (11), σ defines the polarization (TE or TM) of the electromagnetic field, $\mathbf{k}$ is the component of the wave vector parallel to the surfaces, $k=|\mathbf{k}|$ and $\kappa=\sqrt{k^2-\omega^2/c^2}$ ($\mathrm{Im}[\kappa]\leq 0; \mathrm{Re}[\kappa]\geq 0$) and k_{B} denotes the Boltzmann constant. Considering materials with different reflection properties, several experimental groups have shown that the Casimir pressure can be substantially modified [46,47,49,50,54,57,143–146]. In particular, leveraging the interplay between optical properties and geometry (see also Section 4.1.2), not only the strength but also the sign of interaction can be changed [146–150].

One of the most representative and, at the same time, most controversial examples highlighting the relevance of material properties in the Casimir interaction is provided by their role in determining the finite-temperature correction to the Casimir force between parallel metal plates. For more than two decades now this has been a topic of intense investigation and debate. A description of the metal in terms of the commonly used Drude model,

$$\varepsilon(\omega) = 1-\frac{\Omega^2}{\omega(\omega+\mathrm{i}\gamma)}, \tag{12}$$

where Ω is the plasma frequency and γ a non-zero dissipation rate, gives rise to a temperature dependence of the force, which considerably differs from that obtained for perfect reflectors [151]. (For recent reviews on the debate around the thermal correction of the Casimir force, see [152,153] and references therein.) This is particularly relevant at large temperatures and/or distances where the force predicted by the Drude model is half the value obtained for perfect reflectors. Puzzlingly, such behavior is not found in many precise measurements of the Casimir force [49,59,145,154–156]. Experiments where the reduction in strength predicted by the Drude model was observed [63,144,157] needed to consider systematic effects, such as the presence of patch potentials in their setups [127,158,159]. Perhaps even more surprising is that the experiments disagreeing with the prediction of the Drude model (12) are in very good agreement with the result obtained by setting $\gamma = 0$ in the same model. This quite suggestive behavior highlights the role of the material properties and, for the present model, of dissipation in the controversy. More generally, within the Lifshitz framework, the disagreement between the experimental measurements and theoretical predictions obtained using the Drude model is related to the description of the optical response of metals at low frequency. This can substantially affect the contribution of the transverse electric ($\sigma =$TE) polarization [160–163]. More specifically, in the limit of large separations a, the difference between the two models discussed here arises because for the Drude model with $\gamma \neq 0$, in agreement with the Bohr—van Leeuwen theorem [164,165], the contribution of the TE-polarization in Equation (11) vanishes at large distance [163]. The model resulting by setting $\gamma = 0$ in Equation (12), often called the plasma model, is equivalent to a relatively simple description of a superconductor [166], which does not fulfill the Bohr–van Leeuwen theorem.

A complementary perspective can be given in terms of specific solutions of the Maxwell equations corresponding to purely dissipative (i.e., over-damped) modes [167], which are physically connected with the Foucault current or 'eddy current' in the interior of the plate's material [162,168–170] (see also Refs. [171,172] for related investigations). These modes have pure imaginary frequencies (see Figure 10) and their dynamics are described by a diffusion equation. The diffusion constant is given by $D = \gamma\lambda^2$, where γ is the dissipation rate of the metal and $\lambda \equiv c/\Omega$ is the plasma penetration depth. The electromagnetic field associated with these currents is evanescent in vacuum, i.e., it exponentially decays with the distance from the surface of the metal. In superconductors, eddy current modes are suppressed by the Meissner effect, explaining the behavior of the Casimir effect with the plasma model. It was shown that the eddy current contribution alone accounts for the difference in the prediction for the Casimir effect at finite temperature obtained with the Drude and the plasma model [162,168]. In particular, in agreement with earlier observations [160,161], the largest contribution of these modes arises for the TE-polarization [163]. Eddy currents are also helpful to understand why accounting for spatial dispersion in light–matter interaction [173] can remove pathologies occurring in the thermodynamic behavior of the Casimir entropy when the Drude model is used [65,174–177]. In particular, they enable discerning among the different models describing spatial dispersion, showing also that not all of them are able to eliminate these inconsistencies [170].

Due to the accuracy and the flexibility of the measurements, as well as the possibility to approach the system in its simplest geometry (two parallel plates), CANNEX allows approaching the study of the interplay between material properties and the Casimir effect from a new perspective. The same flexibility also allows probing the impact on the interaction of materials with special or exotic properties, such as magnetic materials [145,178,179], graphene [51,180–182], and others [183–186], using planar structures. This can offer new understandings for the resolution of the controversy and, in general, additional information about the behavior of the Casimir force in regimes and, in particular, for distances that were not explored before in experiments.

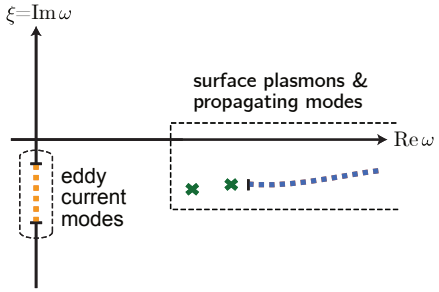

Figure 10. Schematic representation of the typical electromagnetic mode-frequencies vibrating within a planar cavity made by dispersive and dissipative metallic mirrors described in terms of the Drude model [167]. Due to dissipation and according to causality, all modes are resonances described by a complex frequency located in the lower half of the complex-frequency plane. Typical resonances include surface plasmons (green crosses) and cavity modes (blue dots) [187,188]. Due to their diffusive nature, the eddy currents are described in terms of a pure imaginary frequency and are, therefore, located along the negative imaginary axis [162,168].

4.1.2. The Geometry of the System

It was recognized early on that the Casimir effect can be substantially modified by changing the geometry of the involved objects. One of the most remarkable examples is probably the calculation of T. Boyer in 1968 predicting a repulsive Casimir force on a perfectly conducting spherical shell cavity [189] (see also Ref. [190] for recent evaluations with the same geometry). In the last decade, theoretical developments have shown how to efficiently compute the Casimir interaction in systems involving complex structures. A large variety of methods, ranging from semi-analytical [191–199] to full numerical [199–204], have been developed. The main drives of this progress have been, on the one side, the necessity to accurately interpretmeasurements of the Casimir force in realistic setups, and, on the other side, the ambition to deterministically tune the interaction. Controlling the Casimir force can help in reducing unwanted stiction in microscopic devices like MEMS and NEMS, and it can serve as an additional contactless mechanical actuator for similar devices [205,206].

Among the most studied geometries different from plane–plane originally considered by Casimir, one finds the plane–sphere configuration. As a matter of fact, this geometry has been for a long time the workhorse in experiments aiming to measure the Casimir force [37,38,156,205,207,208]. Considering a sphere in front of a plane indeed releases the constraint of parallelism, drastically simplifying the experimental setup. The price to pay is, however, a smaller signal and a more difficult interpretation of the measurement. The latter has for a long time relied on the so-called proximity force approximation, sometimes also called the Derjaguin approximation [207]. If the radius of the sphere is larger than the distance between the surfaces of the two objects, this approximation connects the sphere–plane Casimir force to the energy in the plane–plane configuration. Although previous experiments have directly investigated the plane–plane configuration [100,209], CANNEX is one of the first modern apparatuses designed to reexamine this geometry without strongly penalizing compromises between control, accuracy, and strength of the signal. This same characteristic and the flexibility of this setup can be employed in order to investigate from a new perspective the interaction between different planar structures, ranging from multilayer stacks to nanostructured surfaces, like periodic gratings [191,193–195,197,210–214] or more modern and complex arrangements, such as, for example, metasurfaces [215–217].

Specifically, the one-dimensional lamellar grating structure has already found its way into Casimir physics. Its relative simplicity has allowed for an accurate theoretical description of the Casimir interaction between two vacuum-separated gratings with commensurable periods. Within the framework of the scattering approach [218–221] the evaluation is essentially reduced to the calculation of the scattering matrices of the two nanostructured objects. For instance, the Casimir pressure at temperature T between

two parallel gratings with the same period p separated by the distance a can be obtained from [192,193].

$$P(a) = -4k_B T \sum_{l=0}^{\infty}{}' \int_0^{\infty} dk_y \int_0^{\pi/p} d\alpha_0 \, \partial_a \log\det\left[1 - \underleftarrow{\mathcal{R}}^{L}\mathcal{P}(a)\,\underrightarrow{\mathcal{R}}^{R}\mathcal{P}(a)\right]. \tag{13}$$

Here, $\mathcal{P}$ are the matrices describing the propagation of the electromagnetic field in the vacuum between the gratings, and $\mathcal{R}$ are the gratings' reflection matrices. The arrows under the reflection and propagation matrices indicate the direction of propagation of light, and their expression can be obtained using rigorous coupled wave approaches (RCWA), as in classical photonics [222]. The propagation matrices are diagonal in a plane-wave, Rayleigh basis (see for example [192] for explicit expressions). All these matrices are evaluated at the Matsubara imaginary frequencies, $\omega_l = \mathrm{i}\xi_l = \mathrm{i}2\pi l k_B T/\hbar$ [223], and the primed sum indicates that the $l = 0$ term has half weight. A particular example of this geometry is represented in Figure 11, left, where the depth h of one of the gratings was reduced to zero to recover a plane. For a grating structure with specific geometrical parameters and comprised by a metal described using the Drude model, the predictions corresponding to Equation (13) are reported in Figure 11, right. At short separations, due to the finite grating conductivity, the pressure scales as $\propto a^{-3}$. At large separations, the pressure tends towards the value $\zeta(3)k_B T/(8\pi a^3)$, which is the same limiting behavior for the Casimir pressure predicted for the plane–plane configuration using the Drude model.

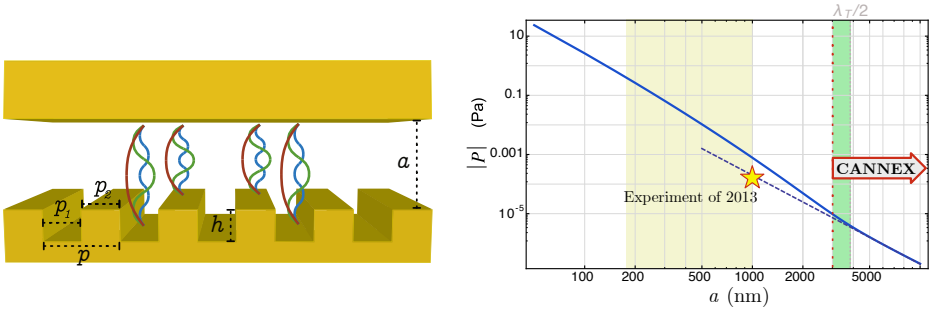

Figure 11. Left: A schematic representation of one of the simplest configurations for investigating the impact of nanostructuring on the Casimir effect: a one dimensional lamellar grating facing a plane. The grating can be characterized with the help of the following parameters: width of the grooves p_1, width p_2, and height h of the teeth. **Right**: Casimir pressure between a metallic grating and a metallic plane (see Ref. [194] for further details). The metal is modeled using the Drude model with $\Omega = 8.39\,\mathrm{eV}$ and $\gamma = 0.043\,\mathrm{eV}$, corresponding to the values of gold. The grating is characterized by the following parameters: $p_1 = 160\,\mathrm{nm}$, $p_2 = 90\,\mathrm{nm}$, and height $h = 216\,\mathrm{nm}$. The temperature of the system is set to $T = 300\,\mathrm{K}$. At separations larger than the thermal wavelength [$\lambda_T = \hbar c/(k_B T)$], the pressure tends towards the value $\zeta(3)k_B T/(8\pi a^3)$ (dashed curve), which is the same limiting behavior for the Casimir pressure predicted for the plane–plane configuration using the Drude model. At short separations, the pressure is proportional to a^{-3} because of the finite grating conductivity. The yellow shadow region describes the distance range investigated in Ref. [213] and the star indicates the value of the Casimir pressure measured around 1 μm in the same experiment. See text for details.

Despite systems involving 'simple' one-dimensional grating structures having been actively investigated both theoretically [191,193–195,197,212,213] and experimentally [43,210,211,213,214,224], some disagreements between the predictions and measurements of the corresponding Casimir pressure remain. For example, an experiment reported in Ref. [213] measuring the Casimir force between a gold sphere and a one-dimensional gold grating at finite temperature has shown that the Casimir force can be tailored in a nontrivial way by modifying the grating's period [213]. Conversely to comparable measurements involving a dielectric grating [210,211,214], however, the theoretical predictions and the experimental results do not agree, indicating once again the possibility that when metals are involved something in the physics of the system still needs to be understood.

In Figure 11, right, we depict the theoretical predictions for the Casimir pressure between a plane and a grating with dimensions quite similar to those used in Ref. [213], as well as the designated working range of the CANNEX setup. The distance range, as well as the value of the pressure measured for the largest plane–sphere separation in the experiment reported in Ref. [213], are also represented, showing that CANNEX has the potential to inspect a complementary regime. Specifically, the device's accuracy of 1 nPa could allow to investigate the pressure behavior within a range of distances corresponding to the transition to the thermal regime. This is expected to occur for distances of the order of $\lambda_T = \hbar c/(k_B T) \simeq 7.6$ μm (green shadowed region in Figure 11), considerably higher than the largest separation considered in many experiments. Shorter separations could be investigated using the same setup with a slightly more rigid sensor. This would reduce the sensitivity, but as the Casimir forces in this distance range scale as a^{-n} with n between 3 and 4, while other disturbing effects, such as patches or electrostatics scale with $2 \leq n < 4$, the precision of the measurement would not be reduced.

4.1.3. The Thermodynamic State of the System: Configurations out of Thermal Equilibrium

The Lifshitz theory of Casimir interactions assumes that the whole system is at thermal equilibrium at temperature T. Recent investigations have shown, however, that when non-equilibrium configurations are taken into account, interesting phenomena can occur [225–227]. Out-of-equilibrium configurations can be realized with different expedients, including temperature gradients [66,225,228–230], moving objects [226,227], and also scenarios where external lasers act on a system initially in thermal equilibrium [231,232]. In many experiments, non-equilibrium physics aremore the rule than the exception. In particular, the presence of different temperatures in the system can considerably affect the Casimir force's behavior, giving rise to repulsive interactions and different power-law dependencies [66,225,229,230]. In addition to providing alternative ways to tailor Casimir forces, non-equilibrium configurations also offer opportunities to differently investigate the interplay between the Casimir interaction, the material's optical properties, and the system geometry, possibly adding new relevant information for solving some of the issues mentioned above.

The high symmetry of the plane–plane configuration has allowed in Ref. [228] for a detailed calculation of the thermal non-equilibrium Casimir pressure acting on the inside faces of two planar plate configuration. As in the Lifshitz Formula (11), the planes can be characterized using the corresponding reflection coefficients r_i^σ, $i = 1, 2$. If each planar plate is assumed to be locally in thermal equilibrium at the temperature T_i within an environment that is kept at temperature T_3, the total Casimir pressure on the plate i can be written as follows [66]:

$$P^{(i)}(a, T_1, T_2) = \frac{1}{2} \sum_{i=1,2} \left[P_{\mathrm{Lif}}(a, T_i) + \frac{4\sigma_{\mathrm{SB}}}{3c} T_i^4 \right] + \Delta P_{\mathrm{neq}}(a, T_1, T_2) - \frac{2\sigma_{\mathrm{SB}}}{3c} (T_i^4 + T_3^4) \,, \quad (14)$$

where σ_{SB} is the Stefan–Bolzmann (SB) constant. The first term is equivalent to the average equilibrium pressure predicted by the Lifshitz formula and the SB law evaluated at the two different plates' temperatures. The last term is the pressure of the environmental radiation on the plate i (for both plates, we assumed the external surfaces to be blackened [66,233]). The second term, ΔP_{neq}, is a pure non-equilibrium contribution: It can be written as the sum of two contributions arising from evanescent and propagating waves, respectively. Moreover, ΔP_{neq} is non-zero only if the two planar structures are different such that $r_1^\sigma \neq r_2^\sigma$ and it is odd if the plates' temperatures are swapped $\Delta P_{\mathrm{neq}}(a, T_1, T_2) = -\Delta P_{\mathrm{neq}}(a, T_2, T_1)$ (see Appendix B for more details).

The direct connection between the detailed expression for $P^{(i)}(a, T_1, T_2)$ and their reflection coefficients (from the inside of the resulting cavity) allows for some flexibility in the description of the planar structure and, in particular, for the consideration of multilayered structures [234,235]. An example is given in Figure 12, left, which represents a typical configuration used in the CANNEX setup. A possible measurement scheme in-

volves the upper plate, which is kept at equilibrium with the surrounding environment, i.e., $T_1 = T_3 = T_{eq} = 293$ K, while the lower plate is cooled by $\Delta T_2 = 10$ K during a first measurement campaign and then warmed by the same quantity during a second campaign. According to Equation (14), the difference between the two sets of measurements considering the pressures acting on the CANNEX's sensor plate is given by

$$P^{(1)}_{\text{diff}}(a) = P^{(1)}(a, T_{eq}, T_{eq} + \Delta T_2) - P^{(1)}(a, T_{eq}, T_{eq} - \Delta T_2). \tag{15}$$

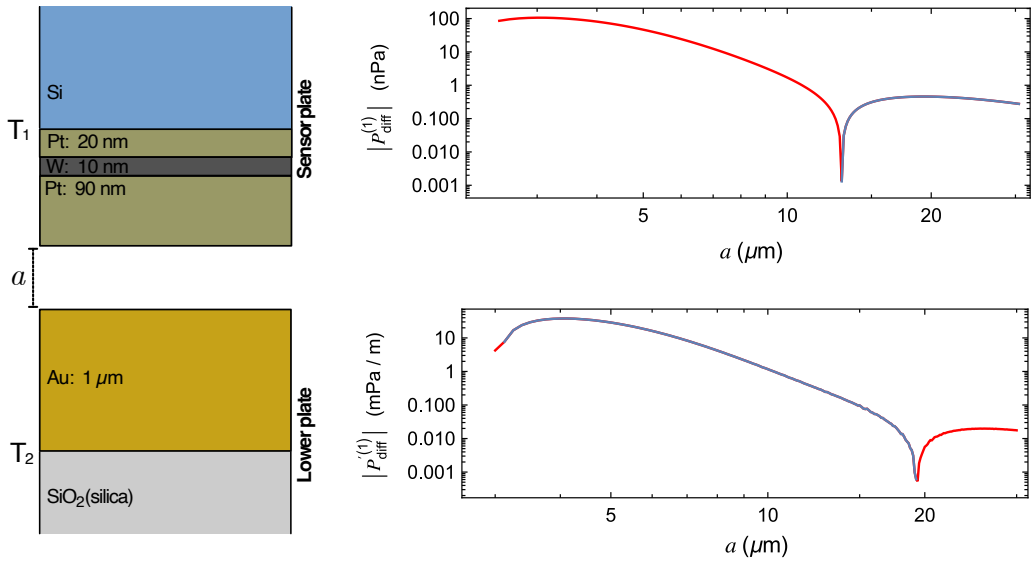

Figure 12. Left: Schematic configuration of the two planar multilayer structures which shall be used in the CANNEX setup for interfacial measurements (not to scale). The lower plate is made by a 1 µm thick gold layer over a silica substrate. The upper/sensor plate is made of a platinum/tungsten/platinum multilayer deposited over a silicon structure. For describing the metals, we use the Drude model (12) with the following parameters: $\Omega_{Au} = 8.39$ eV, $\gamma_{Au} = 43.4$ meV [213]; $\Omega_{Pt} = 5.48$ eV, $\gamma_{Pt} = 86.5$ meV [236]; $\Omega_W = 6.41$ eV, $\gamma_W = 60.4$ meV [237]. For simplicity, we described the silicon and silica layers using the same dielectric function described in terms of the Lorentz model (A8), with the following parameters: $\epsilon_0 = 11.87$, $\epsilon_\infty = 1.035$, $\Omega_0 = 4.346$ eV, and $\Gamma = 43.5$ meV [238]. **Right**: Differential pressure $P^{(1)}_{\text{diff}}(a)$ (see Equation (15)) (**top**) and its gradient (**bottom**) corresponding to out-of-equilibrium configurations, where $T_1 = T_3 = T_{eq} = 293$ K, while the lower plate's temperature is in one case at temperature $T_2 = T_{eq} + \Delta T_2$, and $T_2 = T_{eq} - \Delta T_2$ in the other case. The value of ΔT_2 is taken to be 10 K corresponding to the temperature difference, which can be obtained in CANNEX. The red curves indicate a negative difference while the blue curves describe positive ones. See text for more details.

Since CANNEX can simultaneously measure both the pressure and the pressure gradient, in Figure 12, right, we plot the prediction corresponding to these two quantities for the differential measurement described above and in relation to the material configuration in Figure 12, left. For comparison, in Figure 13, we also report the corresponding equilibrium values ($T_i = T_{eq} = 293$ k) for both the pressure and its gradient calculated using the Lifshitz Formula (11). Notice that over a range of 3–30 µm, we can predict a maximal value for $P^{(1)}_{\text{diff}}(a)$ of about -0.1 mPa for a distance $a = 3$ to 4 µm and a change in sign from negative ($P^{(1)}(a, T_{eq}, T_{eq} + \Delta T) < P^{(1)}(a, T_{eq}, T_{eq} - \Delta T_2)$) to positive ($P^{(1)}(a, T_{eq}, T_{eq} + \Delta T_2) > P^{(1)}(a, T_{eq}, T_{eq} - \Delta T_2)$) around $a = 13$ µm. This means that for sufficiently short distances, the pressure measured by the sensor plate when the lower plate is warmer than the environment is larger than the corresponding pressure measured for a plate which is cooler than the environment. This balance, however, changes as a

function of the separation between the plates. Coherently, Figure 12, bottom right, shows that the pressure gradient, in the range of distance considered in our analysis, changes sign between 3 and 4 µm and again around 20 µm.

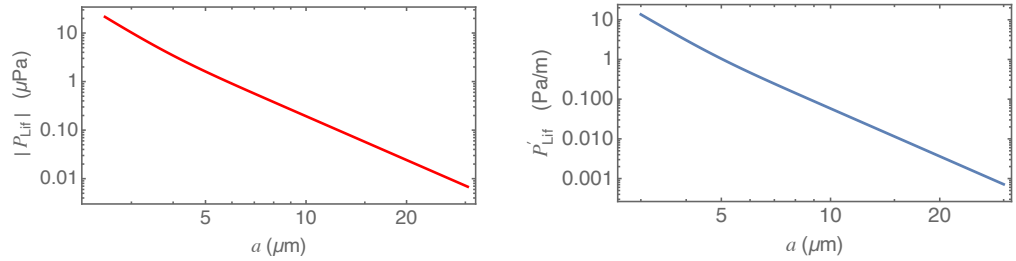

Figure 13. Pressure (**left**) and its gradient (**right**) in equilibrium at temperature $T = T_{eq} = 293$ K for the configuration depicted in Figure 12. The pressure is negative (attraction) while its gradient is positive. The values of both quantities are evaluated using the Lifshitz Formula (11) (see Appendix B) and the material parameters reported in the caption of Figure 12.

4.2. Scalar Dark Energy

A common approach to solving the cosmological constant problem proposes the existence of new hypothetical scalar fields. However, these scalar fields typically introduce so-called fifth forces. Since such additional forces are tightly constrained by ongoing high-precision experiments, these scalar fields must incorporate some kind of 'screening mechanism' to avoid conflict with current experimental results. Several such screening mechanisms have been suggested, such as the chameleon [239,240], K-mouflage [241,242], Vainsthein [243], and Damour–Polyakov [244] mechanisms. All these mechanisms have in common that the fifth force is suppressed in high-density environments. For this reason, high-precision vacuum experiments, such as CANNEX, are ideal tools to probe these hypothetical forces.

The investigations in this paper cover the environment-dependent dilaton [245,246], symmetron [247–249], and chameleon field theories [250]. Notably, the self-interaction potential of the dilaton finds its theoretical origin in the strong coupling limit of string theory [251–253]. The corresponding screening mechanism is highly sensitive to the parameter values and the corresponding behavior has been investigated in detail in [105]. In contrast, symmetrons, resembling the Higgs, employ spontaneous symmetry breaking to realize a screening mechanism. In low-density regions, the field is in its spontaneously broken phase and, hence, acquires a non-vanishing vacuum expectation value (VEV), resulting in a fifth force. However, in high-density regions, the symmetry is restored and the fifth force vanishes. Still another screened scalar field theory is the chameleon with a screening mechanism, which increases the mass in dense environments (see, e.g., [250,254] for reviews concerning the symmetron and chameleon field).

While the chameleon and the symmetron field have been constrained by several experiments, such as atomic interferometry [255,256], Eöt–Wash experiments [257], gravity resonance spectroscopy [247,248,258], precision atomic measurements [259], and others [250,254], more recent investigations on the dilaton model have so far provided only constraints by gravity resonance spectroscopy, lunar laser ranging, and neutron interferometry [105,260]. Concerning CANNEX, prospective constraints have been derived for either of these fields [99,102,105]. However, these earlier analyses suffer from various shortcomings, e.g., the chameleon analysis has neglected the vacuum region above the setup's movable mirror in the calculation of the induced pressure. Furthermore, the chameleon parameter Λ has been fixed to the specific value of 2.4 meV. As of now, pressure gradients have not been considered and investigations related to chameleons and symmetrons have not taken variations in the vacuum pressure and plate separation into account. Herein, the most rigorous and complete investigation, closing the discussed gaps, has been carried out.

4.2.1. Theoretical Background

The effective potential of the scalar fields considered herein is given by

$$V_{\text{eff}}(\phi;\rho) = V(\phi) + \rho A(\phi), \tag{16}$$

where $V(\phi)$ is the self-interaction potential and $A(\phi)$ the 'Weyl factor' providing the coupling to the ambient matter density ρ. For all models investigated in this paper, $A(\phi) \simeq 1$ holds. The dilaton (D), symmetron (S), and chameleon (C) models are defined by [250,254]

$$\begin{aligned} V_D(\phi) &= V_0\, e^{-\lambda_D \phi/m_{\text{pl}}}\,, \\ V_S(\phi) &= -\frac{\mu^2}{2}\,\phi^2 + \frac{\lambda_S}{4}\,\phi^4\,, \\ V_C(\phi) &= \frac{\Lambda^{n+4}}{\phi^n}\,, \end{aligned} \tag{17}$$

together with the Weyl factors

$$\begin{aligned} A_D(\phi) &= 1 + \frac{A_2}{2}\frac{\phi^2}{m_{\text{pl}}^2}\,, \\ A_S(\phi) &= 1 + \frac{\phi^2}{2M^2}\,, \\ A_C(\phi) &= e^{\phi/M_c} \simeq 1 + \frac{\phi}{M_c}\,. \end{aligned} \tag{18}$$

The dilaton field is characterized by three parameters, i.e., V_0, an energy scale associated with DE, λ_D, a numerical constant, and A_2, a dimensionless coupling parameter. Then, m_{pl} denotes the reduced Planck mass. Furthermore, the symmetron parameters are given by the tachyonic mass μ, a dimensionless self-coupling constant λ_S, and M as a coupling constant to matter with a dimension of a mass. Finally, for chameleons, $n \in \mathbb{Z}^+ \cup 2\mathbb{Z}^- \setminus \{-2\}$ determines the power of the self-interaction potential, Λ defines an energy scale that is sometimes related to DE, $M_c = m_{\text{pl}}/\beta$ is a coupling constant with dimension of a mass, and β being the dimensionless coupling. To justify the neglect of any higher-order couplings, the analysis herein is restricted to

$$\frac{A_2}{2}\frac{\phi^2}{m_{\text{pl}}^2}\,,\ \frac{\phi^2}{2M^2}\,,\ \frac{\phi}{M_c} \ll 1\,. \tag{19}$$

The resulting equations of motion are given by

$$\Box\phi + V_{\text{eff},\phi}(\phi;\rho) = 0\,, \tag{20}$$

while the non-relativistic force acting on a point particle with mass m is [249]

$$\vec{f}_\phi = -m\vec{\nabla}\ln A(\phi)\,. \tag{21}$$

For the analysis herein, the CANNEX setup is approximated in one dimension along the z-axis as follows: The fixed lower mirror is located at $z < 0$ with density $\rho_M = 2514\,\text{kg/m}^3$, while the movable upper mirror with density ρ_M and thickness $D = 100\,\mu\text{m}$ is located at $a < z < a + D$ with $3\,\mu\text{m} \leq a \leq 30\,\mu\text{m}$. Between both mirrors and above the upper mirror, vacuum prevails with an adjustable density of $5.3 \times 10^{-12}\,\text{kg/m}^3 \leq \rho_V \leq 2.6\,\text{kg/m}^3$. To justify the neglect of the vacuum chamber above the upper plate, an interaction range cut-off at 1 mm has been applied in our analysis. For even greater interaction ranges, the matter content of the vacuum chamber induces a pull on the upper plate, thereby

effectively lowering the pressure on the upper plate. Hence, the force on the upper mirror is given by [261].

$$\vec{f}_\phi = -\rho_M \int_{-\infty}^{\infty} dx \int_{-\infty}^{\infty} dy \int_a^{a+D} dz\, \partial_z \ln A(\phi)\, \vec{e}_z\,, \tag{22}$$

and the pressure in the z-direction on the movable mirror is, therefore,

$$\begin{aligned} P &= \rho_M \left(\ln A(\phi(a)) - \ln A(\phi(a+D)) \right) \\ &\simeq \rho_M \left(A(\phi(a)) - A(\phi(a+D)) \right). \end{aligned} \tag{23}$$

If the field reaches its potential minimum value ϕ_M inside the upper mirror, the latter expression can be simplified further to [105]

$$P = \frac{\rho_M}{\rho_M - \rho_V} \left(V_{\text{eff}}(\phi_V, \rho_V) - V_{\text{eff}}(\phi_0, \rho_V) \right), \tag{24}$$

where $\phi_0 := \phi(a/2)$ is the value of the scalar field in the middle between both plates. This assumption, however, is not very restrictive, since the screening mechanism typically suppresses the field inside the mirror such that the field can effectively reach its potential minimum value. We have checked explicitly that this assumption is actually satisfied for parameter values where limits were set. In order to obtain ϕ_0, the following differential equation has to be solved:

$$\frac{d^2\phi}{dz^2} - V_{\text{eff},\phi}\left(\phi(z), \rho(z)\right) = 0\,. \tag{25}$$

Since the field effectively reaches its potential minimum values inside both mirrors, $\phi(z) = \phi_M$ has been set as a boundary condition deep inside the mirrors. For some cases, analytical solutions to this equation exist [248,249,262]. However, for the new limits obtained herein, we solved this equation numerically. Whenever possible, we performed a comparison with analytical solutions as an additional check. This allowed the reliable computation of the pressure as a function of the plate distance as well as the vacuum density. The pressure gradients can straightforwardly be computed by using

$$\partial_a P \simeq \frac{P(a+\delta) - P(a-\delta)}{2\delta}\,, \tag{26}$$

for small enough δ.

4.2.2. Dilaton Constraints

The resulting constraints for the dilaton field theory are shown in Figure 14. CANNEX will indeed be able to probe parts of the dilaton parameter space that have not been excluded by existing experiments. However, adding pressure gradients to the existing analysis does not improve the constraints that can be obtained with CANNEX.

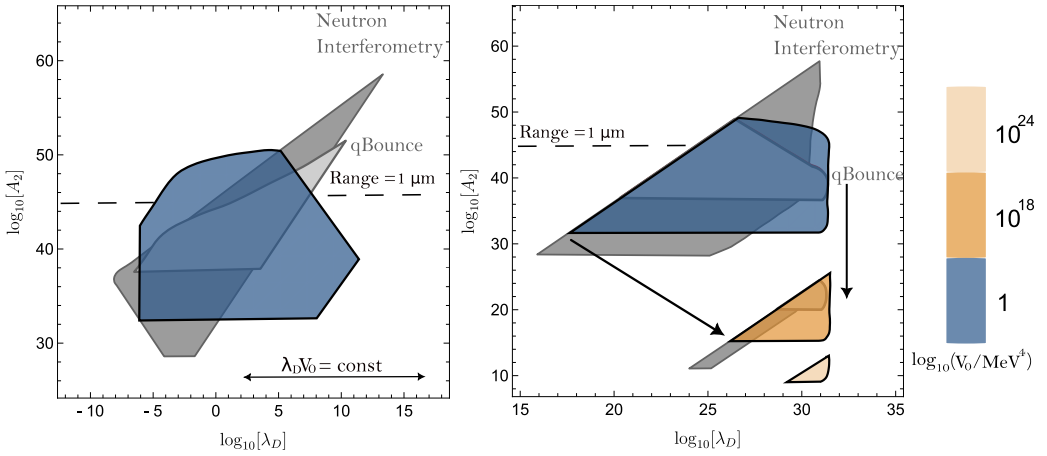

Figure 14. Prospective CANNEX limits on dilaton interactions (in color) alongside the already existing constraints from *q*Bounce and neutron interferometry (assuming the Fermi-screening approximation [105]). The combined constraints from pressure and pressure gradient measurements are plotted. The parameter space of the dilaton field naturally falls into two regimes. **Left**: For small values of the parameter λ_D, the model has an additional parameter symmetry, such that the physics only depend on the product $\lambda_D V_0$ rather than λ_D or V_0 individually. Therefore, the shape of the excluded parameter areas remains the same for increasing V_0, but only shifts towards lower values of λ_D. **Right**: For large values of λ_D, the dilaton approximately depends only on $A_2 \ln\left(V_0/\rho\right)$, but not on their individual values. Therefore, the excluded parameter areas shift towards lower A_2 for increasing V_0 without changing their shape. However, in contrast to the small λ_D regime, the areas are cut by an ever stronger cut-off as indicated by the arrows.

4.2.3. Symmetron Constraints

The resulting constraints for the symmetron field theory are shown in Figure 15. For too small values of μ, the field vanishes entirely and with it the induced pressure as well. This happens approximately for [248]

$$\sqrt{\mu^2 - \frac{\rho_V}{M^2}}\, a < \frac{\pi}{2}\,. \tag{27}$$

For too large μ values, however, the force between the plates gets very weak. Hence, CANNEX can only probe a small interval of μ values. It has been found that in some cases the pressure gradients provide better constraints than the pressure itself and that the plate separation has strong impact on the limits. The analysis herein significantly improves on the analysis in Ref. [99]. Specifically, for μ = 1 eV, corresponding roughly to an interaction range of 0.2 µm, the CANNEX limits have previously been underestimated by a factor of $\sim 10^{20}$ on the λ_S axis, since a plate separation of 10 µm was assumed. Clearly, a smaller plate separation of 3 µm yields an enormously stronger pressure and consequently better constraints. Due to the same reason, previous limits for $\mu = 10^{-0.5}$ eV have also been underestimated by several orders of magnitude. Based on Equation (27), in combination with a value of $a = 10$ µm, the conclusion was drawn in [99] that CANNEX can probe only parameter values $M > 10^2$ GeV for $\mu = 10^{-3/2}$ eV, resulting in weak limits. However, increasing a to 20 µm removes this constraint and more substantial limits with $M > 10^{-4.5}$ GeV can be obtained, resulting in significant improvements with respect to the existing constraints. Indeed, CANNEX will be able to improve upon existing table-top experiment constraints by several orders of magnitude.

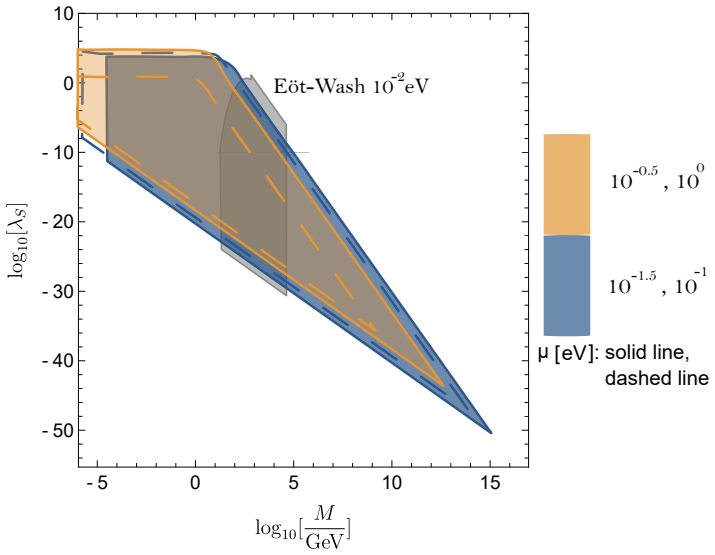

Figure 15. Prospective constraints on symmetron interactions from CANNEX. The colored areas refer to the constraints for $\mu \in \{10^{-1.5}, 10^{-0.5}\}$ eV, the colored dashed lines enclose the constraints for $\mu \in \{10^{-1}, 10^{0}\}$ eV, as indicated. Only the combined constraints from pressure and pressure gradient measurements are shown, alongside already existing constraints.

4.2.4. Chameleon Constraints

Since each value of n is typically considered as a separate chameleon model, the analysis herein has been restricted to two cases. The most commonly studied model is $n = 1$ and, hence, limits have been computed for $n = 1$ and varying Λ. However, within the current limits of the applied theoretical analysis, no new parts of the parameter space can be probed using CANNEX. Nevertheless, fixing $\Lambda = 2.4$ meV to the DE scale and varying $1 \leq n \leq 10$, which is also commonly studied, will indeed result in narrowing the gap between the existing limits, as shown in Figure 16.

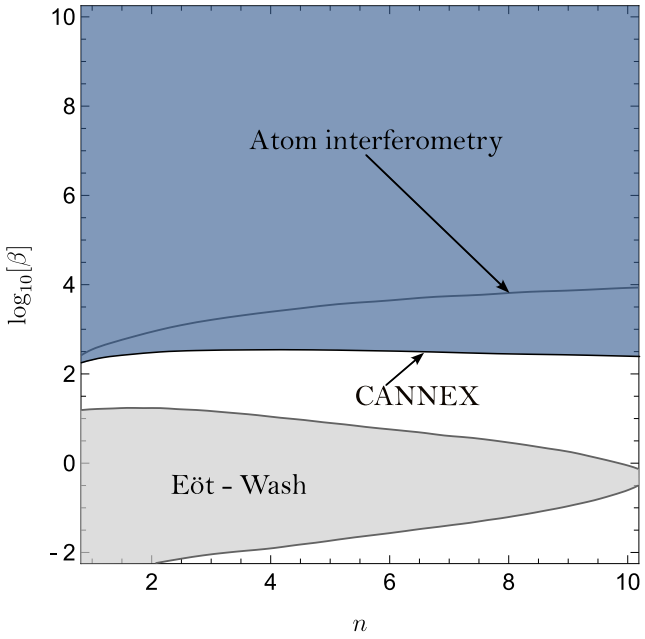

Figure 16. The blue area shows the combined prospective constraints of pressure and pressure gradient measurements on chameleon interactions resulting from CANNEX, while gray areas indicate parameter combinations already excluded by torsion balances and atom interferometry. The parameter Λ has been fixed here to the DE scale of 2.4 meV. See text for details.

5. Discussion

CANNEX has completed its design phase and is about to be realized, with the first results expected in 2024. It is the first experiment to perform highly accurate measurements of both interfacial and gravity-like forces and force gradients in the distance regime 3–30 µm with truly plane parallel plates. This geometry increases the sensitivity to distance-dependent forces by several orders of magnitude with respect to the curved interacting surfaces used in most other experiments. High accuracy naturally demands control of various disturbing effects. We have designed and (partially) tested thermal control at the (sub-)mK precision level both in thermal equilibrium and with the two interacting plates being out of thermal equilibrium by 10 °C. We also designed a six-axis passive seismic attenuation system, in situ surface charge and impurity removal by UV irradiation and Ar ions, purely optical detection systems, and an in situ Kelvin probe/AFM setup to characterize the surfaces. Importantly, our calibration procedures rely on references that can be traced to metrological standards (wavelengths, voltages, frequencies).

In the present paper, we give a final update on the design and measurement procedures, on the basis of which we compute a detailed update of the detection error and seismic disturbances. Using specifications of and noise measurements with the actual devices, we find that the error at large separation $a \gtrsim 15$ µm can realistically be reduced by factors 2 and 30 in the pressure and its gradient, respectively, with respect to the previous error budget in Ref. [99].

CANNEX can be operated in different configurations. In the interfacial configuration, the two plates directly face each other, which allows us to measure the Casimir forces, and the hypothetical screened scalar DE forces. Measuring the former at the percent level at separations both smaller and larger than the thermal wavelength allows us for the first time to probe the transition from a predominantly quantum mechanical origin to a thermal origin in the Casimir force at high accuracy. The respective data may lead to further insights regarding longstanding problems regarding the role of dissipation and locality in the description of the dielectric response of metals. CANNEX could also perform the first quantitative measurements of Casimir forces out of thermal equilibrium, thereby testing the respective theory. Eventually, the plates can easily be modified by structuring. Thanks to control of parallelism at the µrad level, gratings or cylinders at arbitrary angles could be investigated, thereby generating high-precision data that can be used to further verify theoretical approaches currently disagreeing with the measurement results for such geometries. While the Casimir force is a worthwhile subject to study, it also poses a problem if we aim to measure screened scalar DE forces which have a similar distance dependence, but in comparison, several orders of magnitude lower strength. An electrostatic shield would entirely block these interactions. For this reason, we adapt our measurement procedure by remaining in interfacial configuration at the same surface separation but changing the ambient pressure of the Xe gas. In the presence of the gas, electrostatic, Casimir and gravitational forces only show a negligible and calculable increase, while screened DE forces would decrease in strength. In a relative measurement with and without Xe, our sensitivity to such hypothetical forces is maximized. Here, we have presented updated prospective exclusion graphs for the most prominent representatives of screened scalar fields: dilatons, symmetrons, and chameleons. The new calculations properly take into account the finiteness and geometry of the interacting objects, the formation of the field within the vacuum chamber, and the validity limits of the theory—aspects that have mostly been neglected in the literature. For all three scalar fields, even considering only the most conservative error budget, CANNEX will be able to extend the present limits by several orders of magnitude.

The second possible configuration is the one of Cavendish, where a thin flat conducting shield is added between the two plates in order to remove electrostatic and Casimir forces from the balance. In this configuration, volume-sourced forces, such as gravity or hypothetical fifth forces between fermions in the two plates, can be measured with high sensitivity. As we now reconfirm the previous error budget and prospective limits on

a variety of such forces that have been presented recently [99], we do not update these data here but refer to the literature [99]. With this in mind, CANNEX is considered to be able to measure gravity (and thereby Newton's constant, G) at the 10%-level in a distance regime down to 10 µm with active masses of roughly 30 mg, thereby probably exceeding recent experiments with torsion balances and spherical objects probing in this direction. We remark that, since the thick metal coatings on the plates of CANNEX have densities that exceed those of the carrier material by an order of magnitude, the effective separation between the masses sourcing the gravitational interaction lies close to the actual surface separation, in stark difference to spherical objects.

Author Contributions: Conceptualization, R.I.P.S., H.F., M.P. and F.I.; methodology, R.I.P.S. and M.P.; software, H.F., R.I.P.S. and R.A.S.; design and simulation: I.G., A.B., R.A.S., H.H. and R.I.P.S.; formal analysis, H.F., H.H. and R.I.P.S.; writing—original draft preparation, H.F., R.A.S., H.H., F.I. and R.I.P.S.; writing—review and editing, R.I.P.S., M.P., R.A.S., I.G. and A.B.; visualization, R.A.S. and R.I.P.S.; supervision, M.P. and R.I.P.S.; project administration, R.I.P.S.; funding acquisition, R.I.P.S. and M.P. All authors have read and agreed to the published version of the manuscript.

Funding: This research was funded by the Austrian Science Fund (FWF) under grant No. P 36577-N and P 34240-N.

Data Availability Statement: Data are contained within the article.

Acknowledgments: The authors thank Roman Gergen, Heinz Matusch, Andrzej Pelczar, Thomas Dokulil, and Piotr Suprunowicz for technical support, Max Maichanitsch for analyses of the SAS design, and Hartmut Abele for administrative support. The previous version of this experiment was funded by the Netherlands Organization for Scientific Research (NWO) and donations via the CANNEX crowd funding campaign by ASML and others.

Conflicts of Interest: The authors declare no conflicts of interest.

Abbreviations

The following abbreviations are used in this manuscript:

AC	Alternate Current
AFM	Atomic Force Microscope
AM	Amplitude Modulation
ATI	Atominstitut
CANNEX	Casimir And Non-Newtonian force EXperiment
COBS	Conrad OBServatory
CKM	Cabibbo–Kobayashi–Maskawa matrix
CP(T)	Charge Parity (Time)
cal	calibration
DAMA	DArk MAtter
DAQ	Data Acquisition
DC	Direct Current
DE	Dark Energy
DM	Dark Matter
det	detector
ESS	Electrostatic Shield
EW	Evanescent Wave
exc	excitation
FEM	Finite Element Method
FM	Frequency Modulation
GAS	Geometric Anti-Spring
GR	General Relativity
KPFM	Kelvin Probe Force Microscopy
LED	Light-Emitting Diode
LI	Lock-In amplifier
Lif	Lifshitz

LVDT	Linear Variable Differential Transformer
ΛCDM	Lambda Cold Dark Matter model
MC	Monte Carlo
MEMS	MicroElectroMechanical System
NHNM	New High-Noise Model
NEMS	NanoElectroMechanical System
NLNM	New Low-Noise Model
PE	Peltier Element
PID	Proportional–Integral–Derivative
PLL	Phase-Locked Loop
PW	Propagating Wave
QCD	Quantum ChromoDynamics
QED	Quantum ElectroDynamics
RC	Resistor–Capacitor
RCWA	Rigorous Coupled Wave Approach
RMS	Root Mean Square
SAS	Seismic Attenuation System
SB	Stefan–Boltzmann
STS	STreckeisen Seismometer
SM	Standard Model
SNR	Signal-to-Noise Ratio
SpI	Spectral Integration
sig	signal
TD	Temperature Drift
TE	Transverse Electric
TM	Transverse Magnetic
TU	Technische Universität
UHV	Ultra-High Vacuum
UV	UltraViolet
WIMP	Weakly Interacting Massive Particle

Appendix A. Details of the Error Budget

In this Appendix, we give the models used for the calculation of various specific detection errors. For easier reference, we give them in a listed format below in their original units, while their effects on the respective measurement were listed in Tables 1–4.

As a general model for drift estimation, we assume a generic diurnal sinus model with $A_T = 0.1\,^\circ\mathrm{C}$ amplitude,

$$TD(t) = A_T \sin \frac{2\pi t}{24 \times 3600\,\mathrm{s}}\,, \tag{A1}$$

which over-estimates the actual temperature variation at COBS and statistically exceeds the error for a normal distribution by up to two orders of magnitude, but serves as a worst-case scenario. Table A1 lists further parameters assumed throughout the analysis. For RMS quantities x_{RMS}, we do not use a sharp cutoff at the bandwidth $1/\tau$ but integrate the spectrum $x(\omega)$ up to the maximum frequency $\omega_{\max}$ with a first-order low-pass $T_I(\omega, \tau) = [1 + \mathrm{i}\omega\tau]^{-1}$ yielding a more realistic estimate

$$x_{\mathrm{RMS}}(\tau) = \left[\int_0^{\omega_{\max}} \frac{\mathrm{d}\omega}{2\pi} x^2(\omega) |T_I|^2(\omega)\right]^{\frac{1}{2}}. \tag{A2}$$

Table A1. Global parameters assumed for the error analysis.

Parameter	Value	Description
τ_{DC}	2.0 s	integration time for a single DC voltage measurement
τ_{AC}	83.0 s	lock-in integration time for a single AC amplitude, frequency, or phase measurement
m	26.13 mg	effective dynamic sensor mass
ω_0	$2\pi\times$ 9.8 s^{-1}	free sensor resonance frequency
d	500 µm	nominal sensor cavity size
A	1.035 cm^2	sensor interaction area

Note again that all statistical errors where we do not have information on the spectral dependence, are time-averaged with $1/\sqrt{t/\tau}$, where τ is the time constant of the actual measurement as listed in Table A1. Systematic errors are averaged with $1/\sqrt{N_{cal}}$, where N_{cal} is the number of calibrations. We furthermore use the following indicators on statistics: 'SpI' means that spectral integration is performed according to Equation (A2) instead of regular time averaging (which includes low-frequency thermal drifts); 'TD' indicates that temperature drift is considered on this error according to Equation (A1).

Appendix A.1. DC Signals

Appendix A.1.1. Statistical Errors

DAQ noise, $\delta_{DAQ} = (\frac{1}{2}+1)\times 10^{-7}$ V, containing the aliasing error from 34470A datasheet (first term). Keysight specifies [263] that the error given in the datasheet is for a temperature range of $\pm 1°$C and can be adapted if the real temperature variation is below that. We add 1 µV (second term) to account for noise picked up by cabling, estimated from actual measurements with the device.

Cavity size fluctuations, δd. We consider the RMS value according to Equation (A2) of the measured vertical vibration spectrum (see Figure 2) at COBS, the passive SAS $T_{x0x2}(\omega)$, and the sensor response $T_{z_0 z}(\omega)$ up to $1/\tau$ Hz with $\tau \geq \tau_{DC}$. For $\tau = \tau_{DC}$, we have $\delta d = 8.5$ pm.

Detector noise, δV_{det}. At $\lambda = 1550$ nm, the detectors have a noise level of 0.19 pW/$\sqrt{\text{Hz}}$, at a total incident flux of 1 mW from the fiber interferometer into the detector (based on laser power and the optical properties of the cavity and fiber). We consider a 1 kHz bandwidth for the low-pass filter, resulting in 60 nV RMS noise.

Laser power fluctuations, δP_L (SpI). We received actual TLX1 intensity noise spectra from the manufacturer ranging from $1/(3\times 3600)$ s to 10 kHz. From these data, we determined a temperature correlation coefficient of $4.38 \pm 0.03 \times 10^{-6}$ K^{-1}, but not all of the drift is temperature-related. We, thus, use the measured Allan deviation as error here. For integration times 2, 83, and 1000 s, using Equation (A2), we obtain RMS relative intensity errors 5.53×10^{-4}, 1.51×10^{-5}, and 1.54×10^{-6}, respectively. To the first order, this error is canceled exactly by the normalization in Equation (7).

Laser bandwidth, $\delta\lambda_{BW}$. Given by the datasheet to be 10 kHz (0.08 fm), nominally, as the low-frequency limit of the frequency noise.

Laser frequency noise, $\delta\lambda_f$ (SpI). Derived from manufacturer data of the spectral frequency noise δf in the range 3 Hz–100 MHz. At lower frequencies, the noise is assumed to stay constant at 6.8 MHz/$\sqrt{\text{Hz}}$, which is three orders of magnitude larger than the specified linewidth but serves as a worst-case estimate. We convert these data to wavelength noise by $\delta\lambda_f = (\lambda^2/c)\delta f$ for the mean wavelength $\lambda = 1590$ nm after integration over the spectrum as described at the start of Appendix A, resulting in RMS values 6.28 fm, 1.04 fm, and 0.31 fm for τ = 2, 83 and 1000 s, respectively.

Reference cavity signal, δV_{R}. Respective values are obtained from the total δV_{DC} without seismic vibrations and thermal distance fluctuations, as the reference cavity is a monolithic block made of a material with thermal expansion coefficient of less than $2\times10^{-8}\,\mathrm{K}^{-1}$. We obtain a total $\delta V_{\mathrm{ref}} = 4.82\times10^{-6}\,\mathrm{V}$ and $1.06\times10^{-6}\,\mathrm{V}$ for 1000 s and 72 h integration time, indicating the errors for $V_{\mathrm{R}}(t)$, and $V_{\mathrm{R}}(0)$, respectively. This error could be reduced in practice, as power fluctuations being the main error here also have a significant temperature dependence.

Appendix A.1.2. Systematic Errors

DAQ error, σV_{DAQ} (TD). We use the temperature drift according to manufacturer specifications $\sigma_{\mathrm{DAQ}} = (S_A \times 1\,\mu\mathrm{V} + 1\,\mu\mathrm{V}) \times TD(\tau)$ with $S_A = 0.55\,\mathrm{V}$. For longer measurements, we consider a reset of this error by the Keysight 34470A's auto-calibration routing after $\tau = 1000$ s.

Cavity drift, $\sigma d(t)$ (TD). The effective temperature coefficient of d can only be measured, as uncertainties in the material properties lead to rather different values. Considering the actual geometry and materials, we obtain an estimate of $5\times10^{-8}\,\mathrm{m/K}$, which, together with a preliminary stability 0.1 mK of the core temperature and $TD(\tau)$, results in the second-strongest error at large τ. Knowing the actual temperature, this error could be removed from the results but we do not consider this possibility in the error budget here. We rather assume that $\sigma d(t)$ can be reset using a λ-sweep calibration preceding each measurement point, leading to respective statistical averaging and consider $TD(\tau)$ with amplitude 5 pm. We add to $\sigma d(t)$ the uncertainty of determination obtained from simulated calibration data. For this purpose, we computed 100 λ-sweep datasets considering independently randomized $\delta\lambda$, δV_{sig}, δd, and fixed $\sigma\lambda$ with their respective known statistical widths. The single sweep data are fit to Equation (6) with free parameters S_A, S_B, d, and $\sigma\lambda$. σd is then the standard deviation of all the MC results and the mean parameter error (added as systematic errors) of the fits. The same procedure is used for the reference cavity size determination error σd_{ref}, where we set $\delta d = 0$ for data generation. For the computation of the 72 h reference signal, we assume periodic re-calibration and reset of $\sigma d(t)$ every $500\tau_{\mathrm{DC}} + \tau_{\mathrm{cal}}$, with calibration time $\tau_{\mathrm{cal}} = 2800$ s.

Wavelength drift, $\sigma\lambda(t)$ (TD), is derived from the 1.5 GHz accuracy of the TLX1 for a range 10–40 °C. As the absolute wavelength can be re-calibrated using the frequency-locked reference laser, we assume for operation at COBS a pessimistic maximal error of 12.6 pm/100 as amplitude for $TD(\tau)$. This error averages with the number of measurement points of both data and reference signal; we assume periodic re-calibration and reset of $\sigma\lambda(t)$ every $500\tau_{\mathrm{DC}} + \tau_{\mathrm{cal}}$.

Reference cavity signal (TD)*:* systematic component of $\sigma V_{\mathrm{R}} = 4.7$ and 0.79 µV for 1000 s and 72 h integration time, respectively. Obtained in the same way as σV_{DAQ}.

Appendix A.1.3. Constant Errors

DAQ error, $\sigma_{\mathrm{DAQ}} = 0.1\,\mu\mathrm{V}$, for the Keysight 34470A offset error, exceeding the specifications from the datasheet.

Reference cavity signal: constant component of $\sigma V_{\mathrm{ref}} = 0.1\,\mu\mathrm{V}$, similar as for σ_{DAQ}.

Note that constant errors in d and λ do not appear as voltage errors due to measurement at quadrature. The constant errors are considered in Appendixes A.3 and A.4.

Appendix A.2. AC Signals

Appendix A.2.1. Statistical Errors

PLL frequency noise, δf_{LI}. The short-time stability of the lock-in amplifier's phase-tracking based on phase stability $\delta\phi_{\mathrm{LI}}$ was measured as the RMS value of the phase using

a first-order passive RC-lowpass as a device under test over 3 h, without feedback. This error combines internal electrical noise, aliasing errors, and internal oscillator stability (without an external Rubidium reference clock). We obtained $\delta f_{\mathrm{LI}} \leq \delta\phi_{\mathrm{LI}}\omega_0/(4\pi Q) = 1.80\,\mathrm{nHz}$ (for $Q = 10^4$ and $\delta\phi_{\mathrm{LI}} = 2.4 \times 10^{-4\circ}$).

Frequency measurement, δf_{PID}. This noise quantifies the stability of the frequency tracking algorithm of the PLL together with PID feedback. We measured it using the same first-order passive RC lowpass, resulting in $\delta f_{\mathrm{PID}} = 2.2\,\mu\mathrm{Hz}$.

Signal noise, δf_V (SpI, indirectly; see Appendix A.1). Voltage noise (containing all error sources described in Appendix A.1) can be converted into time jitter of a sinusoidal signal at frequency ω, as explained in the main text in Section 3.2, resulting in $\delta V_{\mathrm{sig}} = 7.39 \times 10^{-7}$ and 5.59×10^{-7} V, $\sigma f_V = 3.90$ and 0.51 nHz for τ_{AC} and 1000 s integration time, respectively and $a = 3\,\mu\mathrm{m}$.

Appendix A.2.2. Systematic Errors

PLL phase stability, $\sigma f_{\mathrm{LI}}(t)$ (TD). This error quantifies the 0.05 ppm/°C drift of the internal oscillator of the lock-in amplifier with temperature, and the respective deviation at COBS. For multiple measurements, we consider periodic re-calibration to average this error. $\sigma f_V(t) = 0.88$ and 10.5 nHz for τ_{AC} and 1000 s integration time, respectively.

Resonance frequency calibration error, $\sigma\omega_0$. The resonance frequency is calibrated prior to each distance sweep or once per day. We use the combined standard deviation and parameter error obtained from MC simulations of the calibration data as described in Section 2.5.2. $\sigma\omega_0 = 1.44 \times 10^{-9}\,\mathrm{s}^{-1}$.

Signal drift, $\sigma f_V(t)$ (TD, indirectly; see Appendix A.1). Drifts of the voltage signal, converted to frequency error, as described in Section 3.2. We obtain $\sigma V_{\mathrm{sig}} = 3.64 \times 10^{-7}$ and 6.69×10^{-7} V, $\sigma f_V(t) = 1.92$ and 3.63 nHz for τ_{AC} and 1000 s integration time, respectively, and $a = 3\,\mu\mathrm{m}$.

Appendix A.2.3. Constant Errors

PLL phase error, σf_{LI}. This error reflects the absolute 0.05 ppm frequency accuracy of the reference Rubidium atomic clock, applied to the sensor resonance frequency ($f_0 = 10\,\mathrm{Hz}$).

Resonance frequency calibration error, $\sigma\omega_0$. This error comes from the mean constant offset error seen in our MC simulations. It is caused by non-linearities in combination with other errors, leading to a constant estimation error $\sigma\omega_0 = 5.53 \times 10^{-7}\,\mathrm{s}^{-1}$.

Signal error: constant component of the signal error, amounting to $\sigma f_V = 0.1\,\mu\mathrm{V}$ or 0.53 nHz (see Section 2.5.2).

Appendix A.3. Pressure Gradient

Appendix A.3.1. Statistical Errors

Frequency measurement, δf (SpI, indirectly; see Appendix A.1. This error is propagated from the AC error described in Appendix A.2 and amounts for τ_{AC} to $\delta f = 1.62$ and 0.47 µV for $\tau = \tau_{\mathrm{AC}}$ and 1000 s, respectively, at $a = 3\,\mu\mathrm{m}$.

Appendix A.3.2. Systematic Errors

Frequency measurement, $\sigma f(t)$ (TD, indirectly; see see Appendix A.1). This error is propagated from the AC error described in Appendix A.2. We obtain $\sigma f = 0.71$ and 7.76 nHz for $\tau = \tau_{\mathrm{AC}}$ and 1000 s, respectively.

Resonance frequency calibration error, $\sigma\omega_0$. This error (described already in Appendix A.2) is considered separately here, as it appears in the expression for the total gradient $\partial_a F$, expressed from Equation (5). $\sigma\omega_0 = 1.44 \times 10^{-9}\,\mathrm{s}^{-1}$.

Mass calibration error, σm. We again use the standard deviation and parameter error determined from MC simulations of calibration data (see Section 2.5.2). $\sigma m = 5.86 \times 10^{-11}$ kg.

Appendix A.3.3. Constant Errors

Frequency measurement, $\sigma f = 5.13$ nHz, is the constant part of the error propagated from the AC frequency detection.

Resonance frequency error, $\sigma\omega_0 = 5.53 \times 10^{-7}\,\mathrm{s}^{-1}$. Mean parameter offset from fits to MC simulation data (see Section 2.5.2).

Mass calibration error, $\sigma m = 1.28 \times 10^{-11}$ kg. Mean parameter offset from fits to MC simulation data (see Section 2.5.2).

Appendix A.4. Pressure

Appendix A.4.1. Statistical Errors

Signal fluctuation, δV_{sig}. Propagated statistical error from the DC signal. Amounts to $\delta V_{\mathrm{sig}} = 0.74$ and 0.10 µV for τ_{AC} and 1000 s integration time, respectively, at $a = 3$ µm.

Reference signal, δV_0. Statistical error of the zero-force reference signal taken at a_{cal} (do not confuse with δV_{R} from the reference cavity). As DC detection is independent of a, we use the same models as for δV_{sig}described in Appendix A.1. $\delta V_0 = 0.01$ µV for $\tau = 1000$ s integration time.

Force gradient, $\delta\partial_a F$. Correcting the spring constant k introduces a dependence on the force gradient. We propagate the corresponding error described in Appendix A.3, resulting in $\delta\partial_a F = 32.5$ and 9.36 nN/m for τ_{AC} and 1000 s integration time, respectively.

Appendix A.4.2. Systematic Errors

Mass calibration error, $\sigma m = 5.86 \times 10^{-11}$ kg, was described in Appendix A.3.

Resonance frequency error, $\sigma\omega_0 = 1.44 \times 10^{-9}\,\mathrm{s}^{-1}$. This is the same error described in Appendix A.2.

Wavelength error, $\sigma\lambda(t)$ (TD, partially). While $\sigma\lambda$ can be measured and brought close to zero by the beat method (see Section 2.5.2), it can also be obtained from a fit to a λ-sweep (see σd above). We use the average parameter uncertainty of the fits combined with the standard deviation of the results using 300 sets of calibration data, resulting in $\sigma\lambda = 0.16$ pm. In addition, we use the known temperature dependence, as described in Appendix A.1: $\sigma\lambda = 12.6\,\mathrm{pm}/100 \times TD(\tau)$, and add the two uncertainties.

Cavity size determination error, $\sigma d(t)$. Same as described in Appendix A.1.

Signal error, σV_{sig} (TD, indirectly; see Appendix A.1). Systematic component of the signal error from Appendix A.1. We use $\sigma V_{\mathrm{sig}} = 0.36$ and 0.69 µV for τ_{AC} and 1000 s, respectively.

Reference signal error, σV_0 (TD, indirectly; see Appendix A.1). Systematic error of the zero-force reference, from Appendix A.1 for $\tau = 1000$ s. $\sigma V_0 = 0.69$ µV.

Force gradient error, $\sigma\partial_a F$ (TD, indirectly; see Appendix A.3. Systematic error of the synchronous force gradient measurement, considering all errors from Appendix A.3, $\sigma\partial_a F = 3.55\,\mathrm{nN/m^2}$ for both $\tau = \tau_{\mathrm{AC}}$ and 1000 s, respectively.

Appendix A.4.3. Constant Errors

Resonance frequency error, $\sigma\omega_0 = 5.53 \times 10^{-7}\,\mathrm{s}^{-10}$. Mean offset from MC simulations, see Appendix A.3.

Mass calibration error, $\sigma m = 1.28 \times 10^{-11}\,\mathrm{kg}$. Mean offset from MC simulations, see Appendix A.3.

Wavelength offset error, $\sigma\lambda$. Absolute error of the Thorlabs LLD1530 reference laser from manufacturer data, adjusted for better thermal stability at COBS, as described in Section 3.2. During the experiment, this may turn out to be a systematic error. Conservatively, we consider it to be constant here. $\sigma\lambda = 3.4\,\mathrm{fm}$.

Signal error, σV_{sig}. Propagated constant error of the DC signal V_{sig}. $\sigma V_{\mathrm{sig}} = 0.19\,\mu\mathrm{V}$.

Reference signal error, σV_0. Constant error of the zero-force reference signal. $\sigma V_0 = 0.19\,\mu\mathrm{V}$.

Force gradient error, $\sigma\partial_a F$. Constant part as described in Appendix A.3, amounting to $\sigma\partial_a F = 1.16\,\mathrm{nN/m}$.

Appendix A.5. Other Errors

The radius of the plates is specified with uncertainty 5 µm. It can be measured with slightly better accuracy. To convert the errors on the force and its gradient to a pressure and pressure gradient, we consider a constant error $A \to A(1+\sigma A)$ with $\sigma A = 2.5 \times 10^{-3}$, considering the maximal deviation on both plates and alignment errors.

Appendix B. Evaluation of the Out of Thermal Equilibrium Casimir Pressure

In the expression for the non-equilibrium Casimir pressure given in Equation (14), the pure non-equilibrium term, ΔP_{neq}, can be written as the sum of a contribution arising from the evanescent waves ($\Delta P_{\mathrm{neq}}^{\mathrm{EW}}$) and a contribution due to the propagating waves ($\Delta P_{\mathrm{neq}}^{\mathrm{PW}}$) [66,228,233]. Considering local and isotropic materials, the two contributions can be conveniently written as

$$\begin{aligned}\Delta P_{\mathrm{neq}}^{\mathrm{EW}}(a,T_1,T_2) &= -\hbar\int_0^\infty \frac{d\omega}{\pi}\Delta n(\omega,T_1,T_2)\int_{\frac{\omega}{c}}^\infty \frac{dk}{2\pi}k\sum_\sigma \kappa\frac{\mathrm{Im}[r_1^\sigma]\mathrm{Re}[r_2^\sigma]-\mathrm{Re}[r_1^\sigma]\mathrm{Im}[r_2^\sigma]}{|1-r_1^\sigma r_2^\sigma e^{-2\kappa a}|^2}e^{-2\kappa a}\\ &= -\frac{\hbar}{2}\int_0^\infty \frac{d\omega}{\pi}\Delta n(\omega,T_1,T_2)\int_0^\infty \frac{d\kappa}{2\pi}\sum_\sigma \kappa^2\frac{2\,\mathrm{Im}[r_1^\sigma (r_2^\sigma)^*]e^{-2\kappa a}}{|1-r_1^\sigma r_2^\sigma e^{-2\kappa a}|^2}\,,\end{aligned} \tag{A3}$$

$$\begin{aligned}\Delta P_{\mathrm{neq}}^{\mathrm{PW}}(a,T_1,T_2) &= -\frac{\hbar}{2}\int_0^\infty \frac{d\omega}{\pi}\Delta n(\omega,T_1,T_2)\int_0^{\frac{\omega}{c}} \frac{dk}{2\pi}k\sum_\sigma k_z\frac{|r_1^\sigma|^2-|r_2^\sigma|^2}{|1-r_1^\sigma r_2^\sigma e^{2\mathrm{i}k_z a}|^2}\\ &= -\frac{\hbar}{2}\int_0^\infty \frac{d\omega}{\pi}\Delta n(\omega,T_1,T_2)\int_0^{\frac{\omega}{c}} \frac{dk_z}{2\pi}\sum_\sigma k_z^2\frac{|r_1^\sigma|^2-|r_2^\sigma|^2}{|1-r_1^\sigma r_2^\sigma e^{2\mathrm{i}k_z a}|^2}\,,\end{aligned} \tag{A4}$$

where it is also assumed that each of the plates is locally in thermal equilibrium at the corresponding temperature. In expressions (A3) and (A4), the same conventions and definitions as described after Equation (11) are used, while '$*$' indicates the complex conjugate of the corresponding quantity. In the second line of Equation (A3), given that κ is non-negative over the whole integration range, we changed the variable from k to κ. Similarly, in the second line of Equation (A4), we performed the variable change $k \to k_z = \sqrt{\omega^2/c^2 - k^2} = \mathrm{i}\kappa$ ($\mathrm{Im}[k_z] \geq 0; \mathrm{Re}[k_z] \geq 0$). We have also defined

$$\begin{aligned}\Delta n(\omega,T_1,T_2) &= n(\omega,T_1)-n(\omega,T_2) = \frac{1}{2}\left(\coth\left[\frac{\hbar\omega}{2k_{\mathrm{B}}T_1}\right]-\coth\left[\frac{\hbar\omega}{2k_{\mathrm{B}}T_2}\right]\right)\\ &= \frac{1}{2}\tanh\left[\frac{\hbar\omega}{2k_{\mathrm{B}}}\left(\frac{1}{T_1}-\frac{1}{T_2}\right)\right]\left(1-\coth\left[\frac{\hbar\omega}{2k_{\mathrm{B}}T_1}\right]\coth\left[\frac{\hbar\omega}{2k_{\mathrm{B}}T_2}\right]\right),\end{aligned} \tag{A5}$$

where $n(\omega,T) = 1/[e^{\frac{\hbar\omega}{k_{\mathrm{B}}T}}-1]$ is the Bose–Einstein occupation number.

As pointed out in Section 4.1.3, the result (11) allows for the consideration of multilayered structures. In this case, numbering the layers in the stack from the top ($n = 1$

corresponds to the medium above the first interface) to the bottom, the reflection coefficients, as seen from an electromagnetic wave impinging from the top of the layer onto the topmost interface can be obtained using the following recurrence formula [234,235]:

$$r_n^\sigma = \frac{\tilde{r}_n^\sigma + r_{n+1}^\sigma e^{-2t_{n+1}\kappa_{n+1}}}{1 + \tilde{r}_n^\sigma r_{n+1}^\sigma e^{-2t_{n+1}\kappa_{n+1}}}\,, \tag{A6}$$

where $\tilde{r}_n^\sigma$ is the interface reflection coefficient between the layer n and $n+1$, t_n is the thickness of the nth-layer and $\kappa_n = \sqrt{k^2 - \epsilon_n(\omega)\omega^2/c^2}$, with $\epsilon_n(\omega)$ the corresponding permittivity. In the case of a finite multilayer structure having N layers, we set $r_N^\sigma = \tilde{r}_N^\sigma$. For local and isotropic materials, the expression for $\tilde{r}_n^\sigma$ can be given in terms of Fresnel coefficients [66,233]

$$\begin{aligned}
\tilde{r}_n^{TE} &= \frac{\sqrt{k^2 - \epsilon_n(\omega)\frac{\omega^2}{c^2}} - \sqrt{k^2 - \epsilon_{n+1}(\omega)\frac{\omega^2}{c^2}}}{\sqrt{k^2 - \epsilon_n(\omega)\frac{\omega^2}{c^2}} + \sqrt{k^2 - \epsilon_{n+1}(\omega)\frac{\omega^2}{c^2}}}\,,\\
\tilde{r}_n^{TM} &= \frac{\epsilon_{n+1}(\omega)\sqrt{k^2 - \epsilon_n(\omega)\frac{\omega^2}{c^2}} - \epsilon_n(\omega)\sqrt{k^2 - \epsilon_{n+1}(\omega)\frac{\omega^2}{c^2}}}{\epsilon_{n+1}(\omega)\sqrt{k^2 - \epsilon_n(\omega)\frac{\omega^2}{c^2}} + \epsilon_n(\omega)\sqrt{k^2 - \epsilon_{n+1}(\omega)\frac{\omega^2}{c^2}}}\,.
\end{aligned} \tag{A7}$$

Commonly, multilayer structures are made out of metallic and insulating layers. One of the simplest mathematical expressions for the dielectric function of metals is given by the Drude model (12). For semiconductors or insulators, a relatively simple description is given by the Lorentz model,

$$\epsilon(\omega) = \epsilon_\infty + \frac{(\epsilon_0 - \epsilon_\infty)\Omega_0^2}{\Omega_0^2 - \omega^2 - \mathrm{i}\Gamma\omega}\,. \tag{A8}$$

For example, this expression is used in Figure 12 to describe the optical properties for both silicon and silica. For simplicity, both materials were described using the parameters as given in Ref. [238], to which we add a small dissipation rate to account for the material dissipation near resonance (see Figure 12).

Figure 12 also presents a calculation involving the pressure gradient $P'(a, T_1, T_2)$. Although the expression for $P'(a, T_1, T_2)$ can be obtained analytically from the expression for $P(a, T_1, T_2)$, the numerical evaluation of the corresponding result can be quite unstable. For this reason, the pressure gradient was obtained by applying a symmetric eighth-order numerical differentiation algorithm, which gives an estimate of the derivative of the function $f(x)$ at the point x_0 as

$$\begin{aligned}
f'(x_0) \approx \frac{1}{\delta}\Big[&\frac{1}{280}f(x_0 - 4\delta) - \frac{4}{105}f(x_0 - 3\delta) + \frac{1}{5}f(x_0 - 2\delta) - \frac{4}{5}f(x_0 - \delta)\\
&+\frac{4}{5}f(x_0 + \delta) - \frac{1}{5}f(x_0 + 2\delta) + \frac{4}{105}f(x_0 + 3\delta) - \frac{1}{280}f(x_0 + 4\delta)\Big]\,.
\end{aligned} \tag{A9}$$

for sufficiently small δ. We checked the result (A9) against the corresponding expression for the derivative with respect to the distance of the Lifshitz Formula (11), which can be obtained by using the identity

$$\partial_a \frac{e^{-2\kappa a}}{1 - r_1^\sigma r_2^\sigma e^{-2\kappa a}} = -\frac{2\kappa e^{-2\kappa a}}{(1 - r_1^\sigma r_2^\sigma e^{-2\kappa a})^2}\,. \tag{A10}$$

The comparison successfully validated the numerical differentiation scheme with $\delta = 1/8$ µm to the level of one part in a million.

References

1. Keshavarzi, A.; Khaw, K.S.; Yoshioka, T. Muon $g-2$: A Review. *Nucl. Phys. B* **2022**, *975*, 115675. [CrossRef]
2. Gao, H.; Vanderhaeghen, M. The Proton Charge Radius. *Rev. Mod. Phys.* **2022**, *94*, 015002. [CrossRef]
3. Tiesinga, E.; Mohr, P.J.; Newell, D.B.; Taylor, B.N. CODATA Recommended Values of the Fundamental Physical Constants: 2018. *Rev. Mod. Phys.* **2021**, *93*, 025010. [CrossRef]
4. Burger, F.A.; Corkery, R.W.; Buhmann, S.Y.; Fiedler, J. Comparison of Theory and Experiments on van der Waals Forces in Media—A Survey. *J. Phys. Chem. C* **2020**, *124*, 24179–24186. [CrossRef]
5. Workman, R.L. et al. [Particle Data Group] Review of Particle Physics. *Prog. Theor. Exp. Phys.* **2022**, *2022*, 083C01. [CrossRef]
6. Hardy, J.C.; Towner, I.S. Superallowed $0^+ \rightarrow 0^+$ nuclear β decays: 2020 critical survey, with implications for V_{ud} and CKM unitarity *Phys. Rev. C* **2020**, *102*, 045501. [CrossRef]
7. Peccei, R.D.; Quinn, H.R. CP Conservation in the Presence of Pseudoparticles. *Phys. Rev. Lett.* **1977**, *38*, 1440–1443. [CrossRef]
8. Peccei, R.D.; Quinn, H.R. Constraints Imposed by CP Conservation in the Presence of Pseudoparticles. *Phys. Rev. D* **1977**, *16*, 1791–1797. [CrossRef]
9. Weinberg, S. A New Light Boson? *Phys. Rev. Lett.* **1978**, *40*, 223–226. [CrossRef]
10. Wilczek, F. Problem of Strong *P* and *T* Invariance in the Presence of Instantons. *Phys. Rev. Lett.* **1978**, *40*, 279–282. [CrossRef]
11. Zwicky, F. Die Rotverschiebung von extragalaktischen Nebeln. *Helv. Phys. Acta* **1933**, *6*, 110–127. Available online: https://www.e-periodica.ch/digbib/view?pid=hpa-001:1933:6#112 (accessed on 7 February 2024).
12. Aghanim, N. et al. [Planck Collaboration] *Planck* 2018 Results. VI. Cosmological Parameters. *Astron. Astrophys.* **2020**, *641*, A6. [CrossRef]
13. Angulo, R.E.; Hahn, O. Large-Scale Dark Matter Simulations. *Liv. Rev. Comput. Astrophys.* **2022**, *8*, 1. [CrossRef]
14. Perlmutter, S.; Aldering, G.; della Valle, M.; Deustua, S.; Ellis, R.S.; Fabbro, S.; Fruchter, A.; Goldhaber, G.; Groom, D.E.; Hook, I.M.; et al. Discovery of a Supernova Explosion at Half the Age of the Universe. *Nature* **1998**, *391*, 51–54. [CrossRef]
15. Riess, A.G.; Filippenko, A.V.; Challis, P.; Clocchiatti, A.; Diercks, A.; Garnavich, P.M.; Gilliland, R.L.; Hogan, C.J.; Jha, S.; Kirshner, R.P.; et al. Observational Evidence from Supernovae for an Accelerating Universe and a Cosmological Constant. *Astrophys. J.* **1998**, *116*, 1009–1038. [CrossRef]
16. Schmidt, B.P.; Suntzeff, N.B.; Phillips, M.M.; Schommer, R.A.; Clocchiatti, A.; Kirshner, R.P.; Garnavich, P.; Challis, P.; Leibundgut, B.; Spyromilio, J.; et al. The High-Z Supernova Search: Measuring Cosmic Deceleration and Global Curvature of the Universe Using Type Ia Supernovae. *Astrophys. J.* **1998**, *507*, 46–63. [CrossRef]
17. Hu, J.P.; Wang, F.Y. Hubble Tension: The Evidence of New Physics. *Universe* **2023**, *9*, 94. [CrossRef]
18. Koch, B.; Käding, C.; Pitschmann, M.; Sedmik, R.I.P. Vacuum Energy, the Casimir Effect, and Newton's Non-Constant. *Universe* **2023**, *9*, 476. [CrossRef]
19. Perivolaropoulos, L.; Skara, F. Challenges for ΛCDM: An Update. *New Astron. Rev.* **2022**, *95*, 101659. [CrossRef]
20. Solà, J. Cosmological Constant and Vacuum Energy: Old and New Ideas. *J. Phys. Conf. Ser.* **2013**, *453*, 012015. [CrossRef]
21. Martin, J. Everything You Always Wanted to Know about the Cosmological Constant Problem (but Were Afraid to Ask). *Comptes Rendus Phys.* **2012**, *13*, 566–665. [CrossRef]
22. Padmanabhan, T. Why Does Gravity Ignore the Vacuum Energy? *Int. J. Mod. Phys. D* **2006**, *15*, 2029–2058. [CrossRef]
23. Weinberg, S. Theories of the Cosmological Constant. *arXiv* **1996**, arXiv:astro-ph/9610044. [CrossRef]
24. Weinberg, S. The Cosmological Constant Problem. *Rev. Mod. Phys.* **1989**, *61*, 1. [CrossRef]
25. Cree, S.S.; Davis, T.M.; Ralph, T.C.; Wang, Q.; Zhu, Z.; Unruh, W.G. Can the Fluctuations of the Quantum Vacuum Solve the Cosmological Constant Problem? *Phys. Rev. D* **2018**, *98*, 063506. [CrossRef]
26. Adler, R.J.; Casey, B.; Jacob, O.C. Vacuum Catastrophe: An Elementary Exposition of the Cosmological Constant Problem. *Am. J. Phys.* **1995**, *63*, 620–626. [CrossRef]
27. Nobbenhuis, S. The Cosmological Constant Problem, an Inspiration for New Physics. Ph.D. Thesis, Utrecht University, Utrecht, The Netherlands, 2006. [CrossRef]
28. Bernabei, R.; Belli, P.; Bussolotti, A.; Cappella, F.; Caracciolo, V.; Cerulli, R.; Dai, C.-J.; D'Angelo, A.; Di Marco, A.; He, H.-L.; et al. First Model Independent Results from DAMA/LIBRA–Phase2. *Universe* **2018**, *4*, 116. [CrossRef]
29. Bulbul, E.; Markevitch, M.; Foster, A.; Smith, R.K.; Loewenstein, M.; Randall, S.W. Detection of an Unidentified Emission Line in the Stacked X-ray Spectrum of Galaxy Clusters. *Astrohpys. J.* **2014**, *789*, 13. [CrossRef]
30. Hofmann, F.; Wegg, C. 7.1 keV Sterile Neutrino Dark Matter Constraints from a Deep Chandra X-ray Observation of the Galactic Bulge Limiting Window. *Astron. Astrophys.* **2019**, *625*, L7. [CrossRef]
31. Barkana, R. Possible Interaction between Baryons and Dark-Matter Particles Revealed by the First Stars. *Nature* **2018**, *555*, 71–74. [CrossRef]
32. Colladay, D.; Kostelecký, V.A. Lorentz-Violating Extension of the Standard Model. *Phys. Rev. D* **1998**, *58*, 116002. [CrossRef]
33. Moody, J.E.; Wilczek, F. New Macroscopic Forces? *Phys. Rev. D* **1984**, *30*, 130–138. [CrossRef]
34. Fadeev, P.; Stadnik, Y.V.; Ficek, F.; Kozlov, M.G.; Flambaum, V.V.; Budker, D. Revisiting Spin-Dependent Forces Mediated by New Bosons: Potentials in the Coordinate-Space Representation for Macroscopic- and Atomic-Scale Experiments. *Phys. Rev. A* **2019**, *99*, 022113. [CrossRef]
35. Sponar, S.; Sedmik, R.I.P.; Pitschmann, M.; Abele, H.; Hasegawa, Y. Tests of Fundamental Quantum Mechanics and Dark Interactions with Low-Energy Neutrons. *Nat. Rev. Phys.* **2021**, *3*, 309–327. [CrossRef]

36. Casimir, H.B.G. On the Attraction between Two Perfectly Conducting Plates. *Proc. Kon. Ned. Akad. Wet. B* **1948**, *51*, 793–795. Available online: https://dwc.knaw.nl/DL/publications/PU00018547.pdf (accessed on 7 February 2024).
37. Lamoreaux, S. Demonstration of the Casimir Force in the 0.6 to 6 μm Range. *Phys. Rev. Lett.* **1997**, *78*, 5. [CrossRef]
38. Mohideen, U.; Roy, A. Precision Measurement of the Casimir Force from 0.1 to 0.9 μm. *Phys. Rev. Lett.* **1998**, *81*, 4549–4552. [CrossRef]
39. Roy, A.; Mohideen, U. Demonstration of the Nontrivial Boundary Dependence of the Casimir Force. *Phys. Rev. Lett.* **1999**, *82*, 4380–4383. [CrossRef]
40. Tang, L.; Wang, M.; Ng, C.Y.; Nikolic, M.; Chan, C.T.; Rodriguez, A.W.; Chan, H.B. Measurement of Non-Monotonic Casimir Forces between Silicon Nanostructures. *Nat. Photon.* **2017**, *11*, 97. [CrossRef]
41. Garrett, J.L.; Somers, D.A.T.; Munday, J.N. Measurement of the Casimir Force between Two Spheres. *Phys. Rev. Lett.* **2018**, *120*, 040401. [CrossRef]
42. Chen, F.; Mohideen, U.; Klimchitskaya, G.L.; Mostepanenko, V.M. Demonstration of the Lateral Casimir Force. *Phys. Rev. Lett.* **2002**, *88*, 101801. [CrossRef]
43. Chiu, H.C.; Klimchitskaya, G.L.; Marachevsky, V.N.; Mostepanenko, V.M.; Mohideen, U. Demonstration of the Asymmetric Lateral Casimir Force between Corrugated Surfaces in the Nonadditive Regime. *Phys. Rev. B* **2009**, *80*, 121402. [CrossRef]
44. Lisanti, M.; Iannuzzi, D.; Capasso, F. Observation of the Skin-Depth Effect on the Casimir Force between Metallic Surfaces. *Proc. Natl. Acad. Sci. USA* **2005**, *102*, 11989. [CrossRef]
45. Chen, F.; Klimchitskaya, G.L.; Mostepanenko, V.M.; Mohideen, U. Demonstration of the Difference in the Casimir Force for Samples with Different Charge-Carrier Densities. *Phys. Rev. Lett.* **2006**, *97*, 170402. [CrossRef]
46. de Man, S.; Heeck, K.; Wijngaarden, R.J.; Iannuzzi, D. Halving the Casimir Force with Conductive Oxides. *Phys. Rev. Lett.* **2009**, *103*, 040402. [CrossRef]
47. Torricelli, G.; van Zwol, P.J.; Shpak, O.; Binns, C.; Palasantzas, G.; Kooi, B.J.; Svetovoy, V.B.; Wuttig, M. Switching Casimir Forces with Phase-Change Materials. *Phys. Rev. A* **2010**, *82*, 010101. [CrossRef]
48. Torricelli, G.; Pirozhenko, I.; Thornton, S.; Lambrecht, A.; Binns, C. Casimir Force between a Metal and a Semimetal. *Europhys. Lett.* **2011**, *93*, 51001. [CrossRef]
49. Banishev, A.A.; Klimchitskaya, G.L.; Mostepanenko, V.M.; Mohideen, U. Demonstration of the Casimir Force between Ferromagnetic Surfaces of a Ni-Coated Sphere and a Ni-Coated Plate. *Phys. Rev. Lett.* **2013**, *110*, 137401. [CrossRef]
50. Banishev, A.A.; Wen, H.; Xu, J.; Kawakami, R.K.; Klimchitskaya, G.L.; Mostepanenko, V.M.; Mohideen, U. Measuring the Casimir Force Gradient from Graphene on a SiO_2 Substrate. *Phys. Rev. B* **2013**, *87*, 205433. [CrossRef]
51. Liu, M.; Zhang, Y.; Klimchitskaya, G.L.; Mostepanenko, V.M.; Mohideen, U. Demonstration of an Unusual Thermal Effect in the Casimir Force from Graphene. *Phys. Rev. Lett.* **2021**, *126*, 206802. [CrossRef]
52. Ardito, R.; Frangi, A.; Corigliano, A.; Masi, B.D.; Cazzaniga, G. The Effect of Nano-Scale Interaction Forces on the Premature Pull-in of Real-Life Micro-Electro-Mechanical Systems. *Microel. Reliab.* **2012**, *52*, 271. [CrossRef]
53. Broer, W.; Palasantzas, G.; Knoester, J.; Svetovoy, V.B. Significance of the Casimir Force and Surface Roughness for Actuation Dynamics of MEMS. *Phys. Rev. B* **2013**, *87*, 125413. [CrossRef]
54. Somers, D.A.T.; Garrett, J.L.; Palm, K.J.; Munday, J.N. Measurement of the Casimir Torque. *Nature* **2018**, *564*, 386–389. [CrossRef]
55. Lee, S.w.; Sigmund, W.M. Repulsive van der Waals Forces for Silica and Alumina. *J. Coloid Interf. Sci.* **2001**, *243*, 365–369. [CrossRef]
56. Feiler, A.A.; Bergström, L.; Rutland, M.W. Superlubricity Using Repulsive van der Waals Forces. *Langmuir* **2008**, *24*, 2274–2276. [CrossRef]
57. Munday, J.N.; Capasso, F.; Parsegian, V.A. Measured Long-Range Repulsive Casimir–Lifshitz Forces. *Nature* **2009**, *457*, 170–173. [CrossRef]
58. Mostepanenko, V.M. Casimir Puzzle and Casimir Conundrum: Discovery and Search for Resolution. *Universe* **2021**, *7*, 84. [CrossRef]
59. Bimonte, G.; López, D.; Decca, R.S. Isoelectronic Determination of the Thermal Casimir Force. *Phys. Rev. B* **2016**, *93*, 184434. [CrossRef]
60. Chen, F.; Klimchitskaya, G.L.; Mostepanenko, V.M.; Mohideen, U. Control of the Casimir force by the modification of dielectric properties with light. *Phys. Rev. B* **2007**, *76*, 035338. [CrossRef]
61. van Zwol, P.; Svetovoy, V.; Palasantzas, G. Characterization of Optical Properties and Surface Roughness Profiles: The Casimir Force Between Real Materials. In *Casimir Physics*; Dalvit, D., Milonni, P., Roberts, D., da Rosa, F., Eds.; Springer: Berlin/Heidelberg, Germany, 2011; pp. 311–343. [CrossRef]
62. Behunin, R.O.; Intravaia, F.; Dalvit, D.A.R.; Neto, P.A.M.; Reynaud, S. Modeling Electrostatic Patch Effects in Casimir Force Measurements. *Phys. Rev. A* **2012**, *85*, 012504. [CrossRef]
63. Sushkov, A.O.; Kim, W.J.; Dalvit, D.A.R.; Lamoreaux, S.K. Observation of the Thermal Casimir Force. *Nat. Phys.* **2011**, *7*, 230–233. [CrossRef]
64. Klimchitskaya, G.L.; Mostepanenko, V.M. An Alternative Response to the Off-Shell Quantum Fluctuations: A Step Forward in Resolution of the Casimir Puzzle. *Eur. Phys. J. C* **2020**, *80*, 900. [CrossRef]
65. Bezerra, V.B.; Klimchitskaya, G.L.; Mostepanenko, V.M.; Romero, C. Violation of the Nernst Heat Theorem in the Theory of the Thermal Casimir Force between Drude Metals. *Phys. Rev. A* **2004**, *69*, 022119. [CrossRef]

66. Klimchitskaya, G.L.; Mostepanenko, V.M.; Sedmik, R.I.P. Casimir Pressure between Metallic Plates out of Thermal Equilibrium: Proposed Test for the Relaxation Properties of Free Electrons. *Phys. Rev. A* **2019**, *100*, 022511. [CrossRef]
67. Bordag, M.; Geyer, B.; Klimchitskaya, G.L.; Mostepanenko, V.M. Stronger Constraints for Nanometer Scale Yukawa-type Hypothetical Interactions from the New Measurement of the Casimir Force. *Phys. Rev. D* **1999**, *60*, 055004. [CrossRef]
68. Mostepanenko, V.M.; Novello, M. Constraints on Non-Newtonian Gravity from the Casimir Force Measurements between Two Crossed Cylinders. *Phys. Rev. D* **2001**, *63*, 115003. [CrossRef]
69. Decca, R.S.; Fischbach, E.; Klimchitskaya, G.L.; Krause, D.E.; López, D.; Mostepanenko, V.M. Improved Tests of Extra-Dimensional Physics and Thermal Quantum Field Theory from New Casimir Force Measurements. *Phys. Rev. D* **2003**, *68*, 116003. [CrossRef]
70. Decca, R.S.; López, D.; Chan, H.B.; Fischbach, E.; Krause, D.E.; Jamell, C.R. Constraining New Forces in the Casimir Regime Using the Isoelectronic Technique. *Phys. Rev. Lett.* **2005**, *94*, 240401. [CrossRef]
71. Decca, R.; López, D.; Fischbach, E.; Klimchitskaya, G.; Krause, D.; Mostepanenko, V. Novel Constraints on Light Elementary Particles and Extra-Dimensional Physics from the Casimir Effect. *Eur. Phys. J. C* **2007**, *51*, 963–975. [CrossRef]
72. Mostepanenko, V.M.; Decca, R.S.; Fischbach, E.; Klimchitskaya, G.L.; Krause, D.E.; López, D. Stronger Constraints on Non-Newtonian Gravity from the Casimir Effect. *J. Phys. A* **2008**, *41*, 164054. [CrossRef]
73. Masuda, M.; Sasaki, M. Limits on Nonstandard Forces in the Submicrometer Range. *Phys. Rev. Lett.* **2009**, *102*, 171101. [CrossRef]
74. Bezerra, V.B.; Klimchitskaya, G.L.; Mostepanenko, V.M.; Romero, C. Advance and Prospects in Constraining the Yukawa-type Corrections to Newtonian Gravity from the Casimir Effect. *Phys. Rev. D* **2010**, *81*, 055003. [CrossRef]
75. Sushkov, A.O.; Kim, W.J.; Dalvit, D.A.R.; Lamoreaux, S.K. New Experimental Limits on Non-Newtonian Forces in the Micrometer Range. *Phys. Rev. Lett.* **2011**, *107*, 171101. [CrossRef]
76. Klimchitskaya, G.L.; Mohideen, U.; Mostepanenko, V.M. Constraints on Corrections to Newtonian Gravity from Two Recent Measurements of the Casimir Interaction between Metallic Surfaces. *Phys. Rev. D* **2013**, *87*, 125031. [CrossRef]
77. Bezerra, V.B.; Klimchitskaya, G.L.; Mostepanenko, V.M.; Romero, C. Constraints on axion-nucleon coupling constants from measuring the Casimir force between corrugated surfaces. *Phys. Rev. D* **2014**, *90*, 055013. [CrossRef]
78. Chen, Y.J.; Tham, W.K.; Krause, D.E.; López, D.; Fischbach, E.; Decca, R.S. Stronger Limits on Hypothetical Yukawa Interactions in the 30–8000 Nm Range. *Phys. Rev. Lett.* **2016**, *116*, 221102. [CrossRef]
79. Klimchitskaya, G.L.; Mostepanenko, V.M. Constraints on Axionlike Particles and Non-Newtonian Gravity from Measuring the Difference of Casimir Forces. *Phys. Rev. D* **2017**, *95*, 123013. [CrossRef]
80. Kuz'min, V.A.; Tkachev, I.I.; Shaposhnikov, M.E. Restrictions Imposed on Light Scalar Particles by Measurements of van der Waals Forces. *JETP Lett.* **1982**, *36*, 59–62. Available online: http://jetpletters.ru/ps/1330/article_20101.shtml (accessed on 7 February 2024).
81. Behunin, R.O.; Dalvit, D.A.R.; Decca, R.S.; Speake, C.C. Limits on the Accuracy of Force Sensing at Short Separations Due to Patch Potentials. *Phys. Rev. D* **2014**, *89*, 051301. [CrossRef]
82. Wang, J.; Guan, S.; Chen, K.; Wu, W.; Tian, Z.; Luo, P.; Jin, A.; Yang, S.; Shao, C.; Luo, J. Test of Non-Newtonian Gravitational Forces at Micrometer Range with Two-Dimensional Force Mapping. *Phys. Rev. D* **2016**, *94*, 122005. [CrossRef]
83. Adelberger, E.G.; Stubbs, C.W.; Heckel, B.R.; Su, Y.; Swanson, H.E.; Smith, G.; Gundlach, J.H.; Rogers, W.F. Testing the Equivalence Principle in the Field of the Earth: Particle Physics at Masses below 1 μeV? *Phys. Rev. D* **1990**, *42*, 3267–3292. [CrossRef] [PubMed]
84. Hoyle, C.D.; Kapner, D.J.; Heckel, B.R.; Adelberger, E.G.; Gundlach, J.H.; Schmidt, U.; Swanson, H.E. Submillimeter Tests of the Gravitational Inverse-Square Law. *Phys. Rev. D* **2004**, *70*, 042004. [CrossRef]
85. Adelberger, E.G.; Heckel, B.R.; Hoedl, S.; Hoyle, C.D.; Kapner, D.J.; Upadhye, A. Particle-Physics Implications of a Recent Test of the Gravitational Inverse-Square Law. *Phys. Rev. Lett.* **2007**, *98*, 131104. [CrossRef]
86. Hammond, G.D.; Speake, C.C.; Trenkel, C.; Patón, A.P. New Constraints on Short-Range Forces Coupling Mass to Intrinsic Spin. *Phys. Rev. Lett.* **2007**, *98*, 081101. [CrossRef]
87. Schlamminger, S.; Choi, K.Y.; Wagner, T.A.; Gundlach, J.H.; Adelberger, E.G. Test of the Equivalence Principle Using a Rotating Torsion Balance. *Phys. Rev. Lett.* **2008**, *100*, 041101. [CrossRef]
88. Heckel, B.R.; Adelberger, E.G.; Cramer, C.E.; Cook, T.S.; Schlamminger, S.; Schmidt, U. Preferred-Frame and *CP*-Violation Tests with Polarized Electrons. *Phys. Rev. D* **2008**, *78*, 092006. [CrossRef]
89. Geraci, A.A.; Smullin, S.J.; Weld, D.M.; Chiaverini, J.; Kapitulnik, A. Improved Constraints on Non-Newtonian Forces at 10 Microns. *Phys. Rev. D* **2008**, *78*, 022002. [CrossRef]
90. Hoedl, S.A.; Fleischer, F.; Adelberger, E.G.; Heckel, B.R. Improved Constraints on an Axion-Mediated Force. *Phys. Rev. Lett.* **2011**, *106*, 041801. [CrossRef]
91. Heckel, B.R.; Terrano, W.A.; Adelberger, E.G. Limits on Exotic Long-Range Spin-Spin Interactions of Electrons. *Phys. Rev. Lett.* **2013**, *111*, 151802. [CrossRef]
92. Terrano, W.A.; Adelberger, E.G.; Lee, J.G.; Heckel, B.R. Short-Range, Spin-Dependent Interactions of Electrons: A Probe for Exotic Pseudo-Goldstone Bosons. *Phys. Rev. Lett.* **2015**, *115*, 201801. [CrossRef]
93. Tan, W.-H.; Yang, S.-Q.; Shao, C.-G.; Li, J.; Du, A.-B.; Zhan, B.-F.; Wang, Q.-L.; Luo, P.-S.; Tu, L.-C.; Luo, J. New Test of the Gravitational Inverse-Square Law at the Submillimeter Range with Dual Modulation and Compensation. *Phys. Rev. Lett.* **2016**, *116*, 131101. [CrossRef] [PubMed]

94. Tan, W.-H.; Du, A.-B.; Dong, W.-C.; Yang, S.-Q.; Shao, C.-G.; Guan, S.-G.; Wang, Q.-L.; Zhan, B.-F.; Luo, P.-S.; Tu, L.-C.; et al. Improvement for Testing the Gravitational Inverse-Square Law at the Submillimeter Range. *Phys. Rev. Lett.* **2020**, *124*, 051301. [CrossRef] [PubMed]
95. Lee, J.G.; Adelberger, E.G.; Cook, T.S.; Fleischer, S.M.; Heckel, B.R. New Test of the Gravitational $1/r^2$ Law at Separations down to 52 µm. *Phys. Rev. Lett.* **2020**, *124*, 101101. [CrossRef] [PubMed]
96. Zhao, Y.-L.; Tan, Y.-J.; Wu, W.-H.; Luo, J.; Shao, C.-G. Constraining the Chameleon Model with the HUST-2020 Torsion Pendulum Experiment. *Phys. Rev. D* **2021**, *103*, 104005. [CrossRef]
97. Sedmik, R.I.P.; Almasi, A.; Iannuzzi, D. Locality of Surface Interactions on Colloidal Probes. *Phys. Rev. B* **2013**, *88*, 165429. [CrossRef]
98. van Zwol, P.J.; Svetovoy, V.B.; Palasantzas, G. Distance upon Contact: Determination from Roughness Profile. *Phys. Rev. B* **2009**, *80*, 235401. [CrossRef]
99. Sedmik, R.I.P.; Pitschmann, M. Next Generation Design and Prospects for CANNEX. *Universe* **2021**, *7*, 234. [CrossRef]
100. Bressi, G.; Carugno, G.; Onofrio, R.; Ruoso, G. Measurement of the Casimir Force between Parallel Metallic Surfaces. *Phys. Rev. Lett.* **2002**, *88*, 041804. [CrossRef] [PubMed]
101. Antonini, P.; Bimonte, G.; Bressi, G.; Carugno, G.; Galeazzi, G.; Messineo, G.; Ruoso, G. An Experimental Apparatus for Measuring the Casimir Effect at Large Distances. *J. Phys. Conf. Ser.* **2009**, *161*, 012006. [CrossRef]
102. Almasi, A.; Brax, P.; Iannuzzi, D.; Sedmik, R.I.P. Force Sensor for Chameleon and Casimir Force Experiments with Parallel-Plate Configuration. *Phys. Rev. D* **2015**, *91*, 102002. [CrossRef]
103. Sedmik, R.; Brax, P. Status Report and First Light from Cannex: Casimir Force Measurements between Flat Parallel Plates. *J. Phys. Conf. Ser.* **2018**, *1138*, 012014. [CrossRef]
104. Sedmik, R.I.P. Casimir and Non-Newtonian Force Experiment (CANNEX): Review, Status, and Outlook. *Int. J. Mod. Phys. A* **2020**, *35*, 2040008. [CrossRef]
105. Fischer, H.; Käding, C.; Sedmik, R.I.P.; Abele, H.; Brax, P.; Pitschmann, M. Search for Environment-Dependent Dilatons. *Phys. Dark Univ.* **2024**, *43*, 101419. [CrossRef]
106. Brax, P.; van de Bruck, C.; Davis, A.C.; Shaw, D.J.; Iannuzzi, D. Tuning the Mass of Chameleon Fields in Casimir Force Experiments. *Phys. Rev. Lett.* **2010**, *104*, 241101. [CrossRef]
107. Stochino, A.; DeSalvo, R.; Huang, Y.; Sannibale, V. Improvement of the Seismic Noise Attenuation Performance of the Monolithic Geometric Anti-Spring Filters for Gravitational Wave Interferometric Detectors. *Nucl. Instrum. Meth. A* **2007**, *580*, 1559–1564. [CrossRef]
108. Stochino, A.; Abbot, B.; Aso, Y.; Barton, M.; Bertolini, A.; Boschi, V.; Coyne, D.; DeSalvo, R.; Galli, C.; Huang, Y.; et al. The Seismic Attenuation System (SAS) for the Advanced LIGO Gravitational Wave Interferometric Detectors. *Nucl. Inst. Methods A* **2009**, *598*, 737. [CrossRef]
109. Blom, M.R.; Beker, M.G.; Bertolini, A.; van den Brand, J.F.J.; Bulten, H.J.; Doets, M.; Hennes, E.; Mul, F.A.; Rabeling, D.S.; Schimmel, A. Vertical and Horizontal Seismic Isolation Performance of the Advanced Virgo External Injection Bench Seismic Attenuation System. *Phys. Procedia* **2015**, *61*, 641–647. [CrossRef]
110. van Heijningen, J.V.; Bertolini, A.; Hennes, E.; Beker, M.G.; Doets, M.; Bulten, H.J.; Agatsuma, K.; Sekiguchi, T.; van den Brand, J.F.J. A Multistage Vibration Isolation System for Advanced Virgo Suspended Optical Benches. *Class. Quant. Grav.* **2019**, *36*, 075007. [CrossRef]
111. Cella, G.; Sannibale, V.; DeSalvo, R.; Márka, S.; Takamori, A. Monolithic Geometric Anti-Spring Blades. *Nucl. Instr. Meth. A* **2005**, *540*, 502–519. [CrossRef]
112. Takamori, A.; Raffai, P.; Márka, S.; DeSalvo, R.; Sannibale, V.; Tariq, H.; Bertolini, A.; Cella, G.; Viboud, N.; Numata, K.; et al. Inverted Pendulum as Low-Frequency Pre-Isolation for Advanced Gravitational Wave Detectors. *Nucl. Instrum. Meth. A* **2007**, *582*, 683–692. [CrossRef]
113. Peterson, J.R. *Observations and Modeling of Seismic Background Noise*; USGS Numbered Series 93-322; U.S. Geological Survey: Reston, VA, USA, 1993. [CrossRef]
114. Beker, M.G.; Bertolini, A.; van den Brand, J.F.J.; Bulten, H.J.; Hennes, E.; Rabeling, D.S. State Observers and Kalman Filtering for High Performance Vibration Isolation Systems. *Rev. Sci. Instrum.* **2014**, *85*, 034501. [CrossRef]
115. Rossi, F.; Opat, G.I. Observations of the Effects of Adsorbates on Patch Potentials. *J. Phys. D Appl. Phys.* **1992**, *25*, 1349–1353. [CrossRef]
116. Garrett, J.L.; Kim, J.; Munday, J.N. Measuring the Effect of Electrostatic Patch Potentials in Casimir Force Experiments. *Phys. Rev. Res.* **2020**, *2*, 023355. [CrossRef]
117. Robertson, N.A.; Blackwood, J.R.; Buchman, S.; Byer, R.L.; Camp, J.; Gill, D.; Hanson, J.; Williams, S.; Zhou, P. Kelvin Probe Measurements: Investigations of the Patch Effect with Applications to ST-7 and LISA. *Class. Quant. Grav.* **2006**, *23*, 2665. [CrossRef]
118. Speake, C.C.; Trenkel, C. Forces between Conducting Surfaces due to Spatial Variations of Surface Potential. *Phys. Rev. Lett.* **2003**, *90*, 160403. [CrossRef]
119. Kim, W.J.; Sushkov, A.O.; Dalvit, D.A.R.; Lamoreaux, S.K. Surface Contact Potential Patches and Casimir Force Measurements. *Phys. Rev. A* **2010**, *81*, 022505. [CrossRef]

120. Fosco, C.D.; Lombardo, F.C.; Mazzitelli, F.D. Electrostatic Interaction due to Patch Potentials on Smooth Conducting Surfaces. *Phys. Rev. A* **2013**, *88*, 062501. [CrossRef]
121. Liu, M.; Schafer, R.; Xu, J.; Mohideen, U. Elimination of Electrostatic Forces in Precision Casimir Force Measurements Using UV and Argon Ion Radiation. *Mod. Phys. Lett. A* **2020**, *35*, 2040001. [CrossRef]
122. de Man, S.; Heeck, K.; Iannuzzi, D. No Anomalous Scaling in Electrostatic Calibrations for Casimir Force Measurements. *Phys. Rev. A* **2009**, *79*, 024102. [CrossRef]
123. Sedmik, R.I.P.; Borghesani, A.F.; Heeck, K.; Iannuzzi, D. Hydrodynamic Force Measurements under Precisely Controlled Conditions: Correlation of Slip Parameters with the Mean Free Path. *Phys. Fluids* **2013**, *25*, 042103. [CrossRef]
124. Sedmik, R.I.P.; Urech, A.; Zalevsky, Z.; Carmeli, I. Efficient Reduction of Casimir Forces by Self-assembled Bio-molecular Thin Films. *arXiv* **2023**, arXiv:2306.16209. [CrossRef]
125. Turetta, N.; Sedona, F.; Liscio, A.; Sambi, M.; Samorì, P. Au(111) Surface Contamination in Ambient Conditions: Unravelling the Dynamics of the Work Function in Air. *Adv. Mater. Interf.* **2021**, *8*, 2100068. [CrossRef]
126. Chavan, D.; Gruca, G.; de Man, S.; Slaman, M.; Rector, J.H.; Heeck, K.; Iannuzzi, D. Ferrule-Top Atomic Force Microscope. *Rev. Sci. Instrum.* **2010**, *81*, 123702. [CrossRef]
127. Behunin, R.O.; Dalvit, D.A.R.; Decca, R.S.; Genet, C.; Jung, I.W.; Lambrecht, A.; Liscio, A.; López, D.; Reynaud, S.; Schnoering, G.; et al. Kelvin Probe Force Microscopy of Metallic Surfaces Used in Casimir Force Measurements. *Phys. Rev. A* **2014**, *90*, 062115. [CrossRef]
128. Zerweck, U.; Loppacher, C.; Otto, T.; Grafström, S.; Eng, L.M. Accuracy and Resolution Limits of Kelvin Probe Force Microscopy. *Phys. Rev. B* **2005**, *71*, 125424. [CrossRef]
129. Axt, A.; Hermes, I.M.; Bergmann, V.W.; Tausendpfund, N.; Weber, S.A.L. Know Your Full Potential: Quantitative Kelvin Probe Force Microscopy on Nanoscale Electrical Devices. *Beilstein J. Nanotechnol.* **2018**, *9*, 1809–1819. [CrossRef]
130. Ma, Z.M.; Mu, J.L.; Tang, J.; Xue, H.; Zhang, H.; Xue, C.Y.; Liu, J.; Li, Y.J. Artifacts in KPFM in FM, AM and Heterodyne AM Modes. *Key Engin. Mater.* **2014**, *609–610*, 1362–1368. [CrossRef]
131. Burke, S.A.; LeDue, J.M.; Miyahara, Y.; Topple, J.M.; Fostner, S.; Grütter, P. Determination of the Local Contact Potential Difference of PTCDA on NaCl: A Comparison of Techniques. *Nanotechnol.* **2009**, *20*, 264012. [CrossRef]
132. Garrett, J.L.; Munday, J.N. Fast, High-Resolution Surface Potential Measurements in Air with Heterodyne Kelvin Probe Force Microscopy. *Nanotechnology* **2016**, *27*, 245705. [CrossRef]
133. Sugawara, Y.; Kou, L.; Ma, Z.; Kamijo, T.; Naitoh, Y.; Jun Li, Y. High Potential Sensitivity in Heterodyne Amplitude-Modulation Kelvin Probe Force Microscopy. *Appl. Phys. Lett.* **2012**, *100*, 223104. [CrossRef]
134. Sugawara, Y.; Miyazaki, M.; Li, Y.J. Surface Potential Measurement by Heterodyne Frequency Modulation Kelvin Probe Force Microscopy in MHz Range. *J. Phys. Commun.* **2020**, *4*, 075015. [CrossRef]
135. Ma, Z.M.; Kou, L.; Naitoh, Y.; Li, Y.J.; Sugawara, Y. The Stray Capacitance Effect in Kelvin Probe Force Microscopy Using FM, AM and Heterodyne AM Modes. *Nanotechnology* **2013**, *24*, 225701. [CrossRef]
136. Miyazaki, M.; Sugawara, Y.; Li, Y.J. Dual-Bias Modulation Heterodyne Kelvin Probe Force Microscopy in FM Mode. *Appl. Phys. Lett.* **2022**, *121*, 241602. [CrossRef]
137. Nonnenmacher, M.; O'Boyle, M.P.; Wickramasinghe, H.K. Kelvin Probe Force Microscopy. *Appl. Phys. Lett.* **1991**, *58*, 2921–2923. [CrossRef]
138. Dobosz, M.; Kożuchowski, M. Overview of the Laser-Wavelength Measurement Methods. *Opt. Lasers Engin.* **2017**, *98*, 107–117. [CrossRef]
139. Thorlabs GmbH (Newton, NJ, USA). Private communication, 2023.
140. Rabinovich, S.G. *Measurement Errors and Uncertainties: Theory and Practice*; AIP Press/Springer Science & Business Media: New York, NY, USA, 2005. [CrossRef]
141. Bordag, M.; Klimchitskaya, G.L.; Mohideen, U.; Mostepanenko, V.M. *Advances in the Casimir Effect*; Oxford University Press: New York, NY, 2014. [CrossRef]
142. Lifshitz, E.M. The Theory of Molecular Attractive Force between Solids. *Sov. Phys. JETP* **1956**, *2*, 73–83. Available online: http://jetp.ras.ru/cgi-bin/e/index/e/2/1/p73?a=list (accessed on 7 February 2024).
143. Iannuzzi, D.; Lisanti, M.; Capasso, F. Effect of Hydrogen-Switchable Mirrors on the Casimir force. *Proc. Natl. Acad. Sci. USA* **2004**, *101*, 4019–4023. [CrossRef]
144. Lamoreaux, S.K. Reanalysis of Casimir Force Measurements in the 0.6-to-6-μm Range. *Phys. Rev. A* **2010**, *82*, 024102. [CrossRef]
145. Banishev, A.A.; Chang, C.C.; Klimchitskaya, G.L.; Mostepanenko, V.M.; Mohideen, U. Measurement of the Gradient of the Casimir Force between a Nonmagnetic Gold Sphere and a Magnetic Nickel Plate. *Phys. Rev. B* **2012**, *85*, 195422. [CrossRef]
146. Zhao, R.; Li, L.; Yang, S.; Bao, W.; Xia, Y.; Ashby, P.; Wang, Y.; Zhang, X. Stable Casimir Equilibria and Quantum Trapping. *Science* **2019**, *364*, 984–987. [CrossRef]
147. Dzyaloshinskii, I.E.; Lifshitz, E.M.; Pitaevskii, L.P. General Theory of the van der Waals' Forces. *Sov. Phys. Usp.* **1961**, *4*, 153–176. [CrossRef]
148. Rodriguez, A.W.; Reid, M.T.H.; Intravaia, F.; Woolf, A.; Dalvit, D.A.R.; Capasso, F.; Johnson, S.G. Geometry-Induced Casimir Suspension of Oblate Bodies in Fluids. *Phys. Rev. Lett.* **2013**, *111*, 180402. [CrossRef]
149. Esteso, V.; Carretero-Palacios, S.; Míguez, H. Nanolevitation Phenomena in Real Plane-Parallel Systems Due to the Balance between Casimir and Gravity Forces. *J. Phys. Chem. C* **2015**, *119*, 5663–5670. [CrossRef]

150. Esteso, V.; Frustaglia, D.; Carretero-Palacios, S.; Míguez, H. Casimir-Lifshitz Optical Resonators: A New Platform for Exploring Physics at the Nanoscale. *Adv. Phys. Res.* **2023**, *3*, 2300065. [CrossRef]
151. Bostrom, M.; Sernelius, B.E. Thermal Effects on the Casimir Force in the 0.1-5 μm Range. *Phys. Rev. Lett.* **2000**, *84*, 4757. [CrossRef]
152. Brevik, I.; Shapiro, B.; Silveirinha, M.G. Fluctuational electrodynamics in and out of equilibrium. *Int. J. Mod. Phys. A* **2022**, *37*, 2241012. [CrossRef]
153. Klimchitskaya, G.L.; Mostepanenko, V.M. Current status of the problem of thermal Casimir force. *Int. J. Mod. Phys. A* **2022**, *37*, 2241002. [CrossRef]
154. Decca, R.S.; López, D.; Fischbach, E.; Klimchitskaya, G.L.; Krause, D.E.; Mostepanenko, V.M. Tests of new physics from precise measurements of the Casimir pressure between two gold-coated plates. *Phys. Rev. D* **2007**, *75*, 077101. [CrossRef]
155. Liu, M.; Xu, J.; Klimchitskaya, G.L.; Mostepanenko, V.M.; Mohideen, U. Precision measurements of the gradient of the Casimir force between ultraclean metallic surfaces at larger separations. *Phys. Rev. A* **2019**, *100*, 052511. [CrossRef]
156. Bimonte, G.; Spreng, B.; Maia Neto, P.A.; Ingold, G.L.; Klimchitskaya, G.L.; Mostepanenko, V.M.; Decca, R.S. Measurement of the Casimir Force between 0.2 and 8 μm: Experimental Procedures and Comparison with Theory. *Universe* **2021**, *7*, 93. [CrossRef]
157. Garcia-Sanchez, D.; Fong, K.Y.; Bhaskaran, H.; Lamoreaux, S.; Tang, H.X. Casimir Force and 'In Situ' Surface Potential Measurements on Nanomembranes. *Phys. Rev. Lett.* **2012**, *109*, 027202. [CrossRef]
158. Behunin, R.O.; Zeng, Y.; Dalvit, D.A.R.; Reynaud, S. Electrostatic Patch Effects in Casimir-force Experiments Performed in the Sphere-Plane Geometry. *Phys. Rev. A* **2012**, *86*, 052509. [CrossRef]
159. Garrett, J.L.; Somers, D.; Munday, J.N. The Effect of Patch Potentials in Casimir Force Measurements Determined by Heterodyne Kelvin Probe Force Microscopy. *J. Phys. Cond. Matter* **2015**, *27*, 214012. [CrossRef]
160. Torgerson, J.R.; Lamoreaux, S.K. Low-frequency Character of the Casimir Force between Metallic Films. *Phys. Rev. E* **2004**, *70*, 047102. [CrossRef]
161. Bimonte, G. Johnson Noise and the Thermal Casimir Effect. *New J. Phys.* **2007**, *9*, 281. [CrossRef]
162. Intravaia, F.; Henkel, C. Casimir Interaction from Magnetically Coupled Eddy Currents. *Phys. Rev. Lett.* **2009**, *103*, 130405. [CrossRef]
163. Klimchitskaya, G.L.; Mostepanenko, V.M. Casimir Effect Invalidates the Drude Model for Transverse Electric Evanescent Waves. *Physics* **2023**, *5*, 952–967. [CrossRef]
164. van Leeuwen, H.J. Problèmes de la théorie électronique du magnétisme. *J. Phys. Radium* **1921**, *2*, 361–377. [CrossRef]
165. Bimonte, G. Bohr–van Leeuwen theorem and the thermal Casimir effect for conductors. *Phys. Rev. A* **2009**, *79*, 042107. [CrossRef]
166. London, F.; London, H. The Electromagnetic Equations of the Supraconductor. *Proc. R. Soc. A Math. Phys. Engin. Sci.* **1935**, *149*, 71–88. [CrossRef]
167. Intravaia, F. How Modes Shape Casimir Physics. *Int. J. Mod. Phys. A* **2022**, *37*, 2241014. . [CrossRef]
168. Intravaia, F.; Ellingsen, S.; Henkel, C. Casimir–Foucault Interaction: Free Energy and Entropy at Low Temperature. *Phys. Rev. A* **2010**, *82*, 032504. [CrossRef]
169. Henkel, C.; Intravaia, F. On the Casimir Entropy between 'Perfect Crystals'. *Int. J. Mod. Phys. A* **2010**, *25*, 2328–2336. .. [CrossRef]
170. Reiche, D.; Busch, K.; Intravaia, F. Quantum Thermodynamics of Overdamped Modes in Local and Spatially Dispersive Materials. *Phys. Rev. A* **2020**, *101*, 012506. [CrossRef]
171. Bimonte, G.; Santamato, E. General Theory of Electromagnetic Fluctuations near a Homogeneous Surface in Terms of Its Reflection Amplitudes. *Phys. Rev. A* **2007**, *76*, 013810. [CrossRef]
172. Guérout, R.; Lambrecht, A.; Milton, K.A.; Reynaud, S. Derivation of the Lifshitz–Matsubara Sum Formula for the Casimir Pressure between Metallic Plane Mirrors. *Phys. Rev. E* **2014**, *90*, 042125. [CrossRef]
173. Svetovoy, V.B.; Esquivel, R. Nonlocal Impedances and the Casimir Entropy at Low Temperatures. *Phys. Rev. E* **2005**, *72*, 036113. [CrossRef]
174. Intravaia, F.; Henkel, C. Casimir Energy and Entropy between Dissipative Mirrors. *J. Phys. A Math. Gen.* **2008**, *41*, 164018. [CrossRef]
175. Klimchitskaya, G.L.; Blagov, E.V.; Mostepanenko, V.M. Problems in the Lifshitz Theory of Atom–Wall Interaction. *Int. J. Mod. Phys. A* **2009**, *24*, 1777–1788. [CrossRef]
176. Klimchitskaya, G.L.; Mohideen, U.; Mostepanenko, V.M. The Casimir Force between real Materials: Experiment and Theory. *Rev. Mod. Phys.* **2009**, *81*, 1827–1885. [CrossRef]
177. Milton, K. The Casimir Force: Feeling the Heat. *Nat. Phys.* **2011**, *7*, 190–191. [CrossRef]
178. Shelden, C.; Spreng, B.; Munday, J.N. Enhanced Repulsive Casimir Forces between Gold and Thin Magnetodielectric Plates. *Phys. Rev. A* **2023**, *108*, 032817. [CrossRef]
179. Banishev, A.A.; Klimchitskaya, G.L.; Mostepanenko, V.M.; Mohideen, U. Casimir Interaction between Two Magnetic Metals in Comparison with Nonmagnetic Test Bodies. *Phys. Rev. B* **2013**, *88*, 155410. [CrossRef]
180. Bordag, M.; Fialkovsky, I.V.; Gitman, D.M.; Vassilevich, D.V. Casimir Interaction between a Perfect Conductor and Graphene Described by the Dirac Model. *Phys. Rev. B* **2009**, *80*, 245406. [CrossRef]
181. Fialkovsky, I.V.; Marachevsky, V.N.; Vassilevich, D.V. Finite-Temperature Casimir Effect for Graphene. *Phys. Rev. B* **2011**, *84*, 035446. [CrossRef]
182. Egerland, C.H.; Busch, K.; Intravaia, F. Polaritonic Contribution to the Casimir Energy between Two Graphene Layers. *Phys. Rev. B* **2019**, *100*, 235418. [CrossRef]

183. Woods, L.M.; Dalvit, D.A.R.; Tkatchenko, A.; Rodriguez-Lopez, P.; Rodriguez, A.W.; Podgornik, R. Materials Perspective on Casimir and van der Waals Interactions. *Rev. Mod. Phys.* **2016**, *88*, 045003. [CrossRef]
184. Fialkovsky, I.; Khusnutdinov, N.; Vassilevich, D. Quest for Casimir Repulsion between Chern-Simons Surfaces. *Phys. Rev. B* **2018**, *97*, 165432. [CrossRef]
185. Chen, L.; Chang, K. Chiral-Anomaly-Driven Casimir-Lifshitz Torque between Weyl Semimetals. *Phys. Rev. Lett.* **2020**, *125*, 047402. [CrossRef]
186. Farias, M.B.; Zyuzin, A.A.; Schmidt, T.L. Casimir Force between Weyl Semimetals in a Chiral Medium. *Phys. Rev. B* **2020**, *101*, 235446. [CrossRef]
187. Intravaia, F.; Lambrecht, A. Surface Plasmon Modes and the Casimir Energy. *Phys. Rev. Lett.* **2005**, *94*, 110404. [CrossRef]
188. Intravaia, F.; Henkel, C.; Lambrecht, A. Role of Surface Plasmons in the Casimir Effect. *Phys. Rev. A* **2007**, *76*, 033820. [CrossRef]
189. Boyer, T.H. Quantum Electromagnetic Zero-Point Energy of a Conducting Spherical Shell and the Casimir Model for a Charged Particle. *Phys. Rev.* **1968**, *174*, 1764–1766. [CrossRef]
190. Graham, N.; Quandt, M.; Weigel, H. Attractive Electromagnetic Casimir Stress on a Spherical Dielectric Shell. *Phys. Lett. B* **2013**, *4–5*, 846–849. [CrossRef]
191. Büscher, R.; Emig, T. Nonperturbative Approach to Casimir Interactions in Periodic Geometries. *Phys. Rev. A* **2004**, *69*, 062101. [CrossRef]
192. Davids, P.S.; Intravaia, F.; Rosa, F.S.S.; Dalvit, D.A.R. Modal Approach to Casimir Forces in Periodic Structures. *Phys. Rev. A* **2010**, *82*, 062111. [CrossRef]
193. Lambrecht, A.; Marachevsky, V.N. Casimir Interaction of Dielectric Gratings. *Phys. Rev. Lett.* **2008**, *101*, 160403. [CrossRef]
194. Intravaia, F.; Davids, P.S.; Decca, R.S.; Aksyuk, V.A.; López, D.; Dalvit, D.A.R. Quasianalytical Modal Approach for Computing Casimir Interactions in Periodic Nanostructures. *Phys. Rev. A* **2012**, *86*, 042101. [CrossRef]
195. Messina, R.; Maia Neto, P.A.; Guizal, B.; Antezza, M. Casimir Interaction between a Sphere and a Grating. *Phys. Rev. A* **2015**, *92*, 062504. [CrossRef]
196. Hartmann, M.; Ingold, G.L.; Neto, P.A.M. Plasma versus Drude Modeling of the Casimir Force: Beyond the Proximity Force Approximation. *Phys. Rev. Lett.* **2017**, *119*, 043901. [CrossRef]
197. Antezza, M.; Chan, H.B.; Guizal, B.; Marachevsky, V.N.; Messina, R.; Wang, M. Giant Casimir Torque between Rotated Gratings and the $\theta = 0$ Anomaly. *Phys. Rev. Lett.* **2020**, *124*, 013903. [CrossRef]
198. Schoger, T.; Spreng, B.; Ingold, G.L.; Lambrecht, A.; Maia Neto, P.A.; Reynaud, S. Universal Casimir Interactions in the Sphere–Sphere Geometry. *Int. J. Mod. Phys. A* **2022**, *37*, 2241005. [CrossRef]
199. Emig, T.; Bimonte, G. Multiple Scattering Expansion for Dielectric Media: Casimir Effect. *Phys. Rev. Lett.* **2023**, *130*, 200401. [CrossRef]
200. Reid, M.T.H.; White, J.; Johnson, S.G. Computation of Casimir Interactions between Arbitrary three-dimensional objects with arbitrary material properties. *Phys. Rev. A* **2011**, *84*, 010503. [CrossRef]
201. Johnson, S. Numerical Methods for Computing Casimir Interactions. In *Casimir Physics*; Dalvit, D., Milonni, P., Roberts, D., da Rosa, F., Eds.; Springer: Berlin/Heidelberg, Germany, 2011; pp. 175–218. [CrossRef]
202. Rodriguez, A.W.; Capasso, F.; Johnson, S.G. The Casimir Effect in Microstructured Geometries. *Nat. Photon.* **2011**, *5*, 211–221. [CrossRef]
203. Reid, M.T.H.; White, J.; Johnson, S.G. Fluctuating Surface Currents: An Algorithm for Efficient Prediction of Casimir Interactions among Arbitrary Materials in Arbitrary Geometries. *Phys. Rev. A* **2013**, *88*, 022514. [CrossRef]
204. Kristensen, P.T.; Beverungen, B.; Intravaia, F.; Busch, K. High-Accuracy Casimir–Polder Force Calculations using the Discontinuous Galerkin Time-Domain method. *Phys. Rev. B* **2023**, *108*, 205424. [CrossRef]
205. Chan, H.B.; Aksyuk, V.A.; Kleiman, R.N.; Bishop, D.J.; Capasso, F. Quantum Mechanical Actuation of Microelectromechanical Systems by the Casimir Force. *Science* **2001**, *291*, 1941–1944. [CrossRef]
206. Chan, H.B.; Aksyuk, V.A.; Kleiman, R.N.; Bishop, D.J.; Capasso, F. Nonlinear Micromechanical Casimir Oscillator. *Phys. Rev. Lett.* **2001**, *87*, 211801. [CrossRef]
207. Derjaguin, B.V.; Abrikosova, I.I.; Lifshitz, E.M. Direct Measurement of Molecular Attraction between Solids Separated by a Narrow Gap. *Quart. Rev. Chem. Soc.* **1956**, *10*, 295–329. [CrossRef]
208. Decca, R.S.; López, D.; Fischbach, E.; Klimchitskaya, G.L.; Krause, D.E.; Mostepanenko, V.M. Precise Comparison of Theory and New Experiment for the Casimir Force Leads to Stronger Constraints on Thermal Quantum Effects and Long-Range Interactions. *Ann. Phys.* **2005**, *318*, 37–80. [CrossRef]
209. Sparnaay, M.J. Attractive Forces between Flat Plates. *Nature* **1957**, *180*, 334–335. [CrossRef]
210. Chan, H.B.; Bao, Y.; Zou, J.; Cirelli, R.A.; Klemens, F.; Mansfield, W.M.; Pai, C.S. Measurement of the Casimir Force between a Gold Sphere and a Silicon Surface with Nanoscale Trench Arrays. *Phys. Rev. Lett.* **2008**, *101*, 030401. [CrossRef]
211. Bao, Y.; Guèrout, R.; Lussange, J.; Lambrecht, A.; Cirelli, R.A.; Klemens, F.; Mansfield, W.M.; Pai, C.S.; Chan, H.B. Casimir Force on a Surface with Shallow Nanoscale Corrugations: Geometry and Finite Conductivity Effects. *Phys. Rev. Lett.* **2010**, *105*, 250402. [CrossRef]
212. Lussange, J.; Guérout, R.; Lambrecht, A. Casimir Energy between Nanostructured Gratings of Arbitrary Periodic Profile. *Phys. Rev. A* **2012**, *86*, 062502. [CrossRef]

213. Intravaia, F.; Koev, S.; Jung, I.W.; Talin, A.A.; Davids, P.S.; Decca, R.S.; Aksyuk, V.A.; Dalvit, D.A.R.; López, D. Strong Casimir Force Reduction through Metallic Surface Nanostructuring. *Nat. Commun.* **2013**, *4*, 2515. [CrossRef] [PubMed]
214. Wang, M.; Tang, L.; Ng, C.Y.; Messina, R.; Guizal, B.; Crosse, J.A.; Antezza, M.; Chan, C.T.; Chan, H.B. Strong Geometry Dependence of the Casimir Force between Interpenetrated Rectangular Gratings. *Nat. Commun.* **2021**, *12*, 600. [CrossRef] [PubMed]
215. Chen, H.T.; Taylor, A.J.; Yu, N. A Review of Metasurfaces: Physics and Applications. *Rep. Prog. Phys.* **2016**, *79*, 076401. [CrossRef] [PubMed]
216. Kort-Kamp, W.J.M.; Azad, A.K.; Dalvit, D.A.R. Space-Time Quantum Metasurfaces. *Phys. Rev. Lett.* **2021**, *127*, 043603. [CrossRef]
217. Qiu, C.W.; Zhang, T.; Hu, G.; Kivshar, Y. Quo Vadis, Metasurfaces? *Nano Lett.* **2021**, *21*, 5461–5474. [CrossRef]
218. Rahi, S.J.; Emig, T.; Graham, N.; Jaffe, R.L.; Kardar, M. Scattering Theory Approach to Electrodynamic Casimir Forces. *Phys. Rev. D* **2009**, *80*, 085021. [CrossRef]
219. Rahi, S.J.; Emig, T.; Jaffe, R.L. Geometry and Material Effects in Casimir Physics-Scattering Theory. In *Casimir Physics*; Dalvit, D., Milonni, P., Roberts, D., da Rosa, F., Eds.; Springer: Berlin/Heidelberg, Germany, 2011; pp. 129–174. [CrossRef]
220. Lambrecht, A.; Canaguier-Durand, A.; Guérout, R.; Reynaud, S. Casimir Effect in the Scattering Approach: Correlations between Material Properties, Temperature and Geometry. In *Casimir Physics*; Dalvit, D., Milonni, P., Roberts, D., da Rosa, F., Eds.; Springer: Berlin/Heidelberg, Germany, 2011; pp. 97–127. [CrossRef]
221. Ingold, G.L.; Lambrecht, A. Casimir Effect from a Scattering Approach. *Am. J. Phys.* **2015**, *83*, 156–162. [CrossRef]
222. Busch, K.; von Freymann, G.; Linden, S.; Mingaleev, S.; Tkeshelashvili, L.; Wegener, M. Periodic Nanostructures for Photonics. *Phys. Rep.* **2007**, *444*, 101–202. [CrossRef]
223. Matsubara, T. A New Approach to Quantum Statistical Mechanics. *Prog. Theor. Phys.* **1955**, *14*, 351–378. [CrossRef]
224. Chiu, H.C.; Klimchitskaya, G.L.; Marachevsky, V.N.; Mostepanenko, V.M.; Mohideen, U. Lateral Casimir Force between Sinusoidally Corrugated Surfaces: Asymmetric Profiles, Deviations from the Proximity Force Approximation, and Comparison with Exact Theory. *Phys. Rev. B* **2010**, *81*, 115417. [CrossRef]
225. Antezza, M.; Pitaevskii, L.P.; Stringari, S.; Svetovoy, V.B. Casimir-Lifshitz Force Out of Thermal Equilibrium and Asymptotic Nonadditivity. *Phys. Rev. Lett.* **2006**, *97*, 223203. [CrossRef]
226. Volokitin, A.I.; Persson, B.N.J. Near-Field Radiative Heat Transfer and Noncontact Friction. *Rev. Mod. Phys.* **2007**, *79*, 1291–1329. [CrossRef]
227. Reiche, D.; Intravaia, F.; Busch, K. Wading through the Void: Exploring Quantum Friction and Nonequilibrium fluctuations. *APL Photon.* **2022**, *7*, 030902. [CrossRef]
228. Antezza, M.; Pitaevskii, L.P.; Stringari, S.; Svetovoy, V.B. Casimir–Lifshitz Force out of Thermal Equilibrium. *Phys. Rev. A* **2008**, *77*, 022901. [CrossRef]
229. Obrecht, J.M.; Wild, R.J.; Antezza, M.; Pitaevskii, L.P.; Stringari, S.; Cornell, E.A. Measurement of the Temperature Dependence of the Casimir-Polder Force. *Phys. Rev. Lett.* **2007**, *98*, 063201. [CrossRef]
230. Messina, R.; Antezza, M. Scattering-Matrix Approach to Casimir–Lifshitz Force and Heat Transfer out of Thermal Equilibrium between Arbitrary Bodies. *Phys. Rev. A* **2011**, *84*, 042102. [CrossRef]
231. Bartolo, N.; Messina, R.; Dalvit, D.A.R.; Intravaia, F. Nonequilibrium Casimir–Polder Plasmonic Interactions. *Phys. Rev. A* **2016**, *93*, 042111. [CrossRef]
232. Fuchs, S.; Bennett, R.; Krems, R.V.; Buhmann, S.Y. Nonadditivity of Optical and Casimir-Polder Potentials. *Phys. Rev. Lett.* **2018**, *121*, 083603. [CrossRef] [PubMed]
233. Bimonte, G.; Emig, T.; Krüger, M.; Kardar, M. Dilution and Resonance-enhanced Repulsion in Nonequilibrium Fluctuation Forces. *Phys. Rev. A* **2011**, *84*, 042503. [CrossRef]
234. Zhang, B.; Henkel, C.; Haller, E.; Wildermuth, S.; Hofferberth, S.; Krüger, P.; Schmiedmayer, J. Relevance of Sub-Surface Chip Layers for the Lifetime of Magnetically Trapped Atoms. *Eur. Phys. J. D* **2005**, *35*, 97–104. [CrossRef]
235. Yariv, A.; Yeh, P. *Optical Waves in Crystals. Propagation and Control of Laser Radiation*; John Wiley & Sons: New York, NY, USA, 1983.
236. Mendoza Herrera, L.J.; Arboleda, D.M.; Santillán, J.M.J.; Fernández van Raap, M.B.; Scaffardi, L.B.; Schinca, D.C. Nanoscale Dielectric Function of Fe, Pt, Ti, Ta, Al, and V: Application to Characterization of Al Nanoparticles Synthesized by Fs Laser Ablation. *Plasmonics* **2017**, *12*, 1813–1824. [CrossRef]
237. Ordal, M.A.; Bell, R.J.; Alexander, R.W.; Long, L.L.; Querry, M.R. Optical Properties of Fourteen Metals in the Infrared and Far Infrared: Al, Co, Cu, Au, Fe, Pb, Mo, Ni, Pd, Pt, Ag, Ti, V, and W. *Appl. Opt.* **1985**, *24*, 4493–4499. [CrossRef] [PubMed]
238. Pirozhenko, I.; Lambrecht, A. Influence of Slab Thickness on the Casimir Force. *Phys. Rev. A* **2008**, *77*, 013811. [CrossRef]
239. Khoury, J.; Weltman, A. Chameleon Cosmology. *Phys. Rev. D* **2004**, *69*, 044026. [CrossRef]
240. Khoury, J. Les Houches Lectures on Physics beyond the Standard Model of Cosmology. *arXiv* **2013**, arXiv:1312.2006. [CrossRef]
241. Brax, P.; Burrage, C.; Davis, A.C. Screening Fifth Forces in K-Essence and DBI Models. *J. Cosmol. Astropart. Phys.* **2013**, *1*, 020. [CrossRef]
242. Brax, P.; Valageas, P. K-Mouflage Cosmology: The Background Evolution. *Phys. Rev. D* **2014**, *90*, 023507. [CrossRef]
243. Vainshtein, A.I. To the Problem of Nonvanishing Gravitation Mass. *Phys. Lett. B* **1972**, *39*, 393–394. [CrossRef]
244. Damour, T.; Polyakov, A.M. The String Dilaton and a Least Coupling Principle. *Nucl. Phys.* **1994**, *B423*, 532–558. [CrossRef]
245. Brax, P.; van de Bruck, C.; Davis, A.C.; Shaw, D. Dilaton and Modified Gravity. *Phys. Rev. D* **2010**, *82*, 063519. [CrossRef]

246. Sakstein, J.A. Astrophysical Tests of Modified Gravity. Ph.D. Thesis, Downing College, University of Cambridge, Cambridge, UK, 2014. [CrossRef]
247. Cronenberg, G.; Brax, P.; Filter, H.; Geltenbort, P.; Jenke, T.; Pignol, G.; Pitschmann, M.; Thalhammer, M.; Abele, H. Acoustic Rabi Oscillations between Gravitational Quantum States and Impact on Symmetron Dark Energy. *Nat. Phys.* **2018**, *14*, 1022–1026. [CrossRef]
248. Brax, P.; Pitschmann, M. Exact Solutions to Nonlinear Symmetron Theory: One- and Two-Mirror Systems. *Phys. Rev. D* **2018**, *97*, 064015. [CrossRef]
249. Pitschmann, M. Exact Solutions to Nonlinear Symmetron Theory: One- and Two-Mirror Systems. II. *Phys. Rev. D* **2021**, *103*, 084013. [CrossRef]
250. Burrage, C.; Sakstein, J. Tests of Chameleon Gravity. *Living Rev. Relativ.* **2018**, *21*, 1. [CrossRef]
251. Gasperini, M.; Piazza, F.; Veneziano, G. Quintessence as a Runaway Dilaton. *Phys. Rev. D* **2001**, *65*, 023508. [CrossRef]
252. Damour, T.; Piazza, F.; Veneziano, G. Violations of the Equivalence Principle in a Dilaton Runaway Scenario. *Phys. Rev. D* **2002**, *66*, 046007, [CrossRef]
253. Damour, T.; Piazza, F.; Veneziano, G. Runaway Dilaton and Equivalence Principle Violations. *Phys. Rev. Lett.* **2002**, *89*, 081601, [CrossRef] [PubMed]
254. Brax, P.; Burrage, C.; Davis, A.C. Laboratory Constraints. *Int. J. Mod. Phys. D* **2018**, *27*, 1848009. [CrossRef]
255. Burrage, C.; Copeland, E.J.; Hinds, E.A. Probing Dark Energy with Atom Interferometry. *J. Cosmol. Astropart. Phys.* **2015**, *2015*, 042. [CrossRef]
256. Burrage, C.; Copeland, E.J. Using Atom Interferometry to Detect Dark Energy. *Contemp. Phys.* **2016**, *57*, 164–176. [CrossRef]
257. Upadhye, A. Symmetron Dark Energy in Laboratory Experiments. *Phys. Rev. Lett.* **2013**, *110*, 031301. [CrossRef] [PubMed]
258. Jenke, T.; Bosina, J.; Micko, J.; Pitschmann, M.; Sedmik, R.; Abele, H. Gravity Resonance Spectroscopy and Dark Energy Symmetron Fields. *Eur. Phys. J. Spec. Top.* **2021**, *230*, 1131–1136. [CrossRef]
259. Brax, P.; Davis, A.C.; Elder, B. Screened Scalar Fields in Hydrogen and Muonium. *Phys. Rev. D* **2023**, *107*, 044008. [CrossRef]
260. Fischer, H.; Käding, C.; Lemmel, H.; Sponar, S.; Pitschmann, M. Search for Dark Energy with Neutron Interferometry. *Prog. Theor. Exp. Phys.* **2024**, *2*, 023E02. [CrossRef]
261. Brax, P.; Fischer, H.; Käding, C.; Pitschmann, M. The Environment Dependent Dilaton in the Laboratory and the Solar System. *Eur. Phys. J. C* **2022**, *82*, 934. [CrossRef]
262. Ivanov, A.N.; Cronenberg, G.; Höllwieser, R.; Jenke, T.; Pitschmann, M.; Wellenzohn, M.; Abele, H. Exact Solution for Chameleon Field, Self-Coupled through the Ratra–Peebles Potential with $n = 1$ and Confined between Two Parallel Plates. *Phys. Rev. D* **2016**, *94*, 085005. [CrossRef]
263. Keysight Technologies (Santa Rosa, CA, USA). Private communication, 2023.